Building Centimeter Sized Heterostacks of 2D Materials: Growth, Transfer and Characterisation

---

Dissertation

zur

Erlangung der naturwissenschaftlichen Doktorwürde
(Dr. sc. nat.)

vorgelegt der

Mathematisch-naturwissenschaftlichen Fakultät
der
Universität Zürich

von

Carlo Maria Bernard
aus Zuzwil (SG)

Promotionskommission
Prof. Dr. Thomas Greber (Vorsitz)
Prof. Dr. Jürg Osterwalder
Prof. Dr. Peter Sutter

Zürich, 2019

M'illumino
d'immenso

Giuseppe Ungaretti

Abstract

Since the discovery of the exfoliation technique to transfer single graphene sheets on supports of choice, which granted the 2010 Nobel prize for physics, the scientific community started to explore the high mobility electronics of this two-dimensional material for more than a decade by now.

The electronic and optical properties of graphene allow it to be a promising candidate material for the new area of nano-electronics, especially when combined with other known two dimensional materials as it is hexagonal boron nitride. The combinations of these materials are called heterostructures, where the insulating and chemically inert properties of hexagonal boron nitride are combined with the high mobility electronics of graphene. The advantages of these heterostructures were shown in previous works where they were prepared through mechanical exfoliation.

Albeit, mechanical exfoliation is a labour intensive process, which limits its use for industrial applications at the present day. An alternative route is a direct growth by chemical vapour deposition on suitable metallic substrates and subsequent electrochemical delamination to transfer the two-dimensional materials to the desired substrate. These processes are industrially implementable, as the process is scalable form microscopically sized samples to large wafer sized material.

In this work, we use 4-inch wafer substrates with single crystalline rhodium and iridium coatings for the growth of high quality graphene and hexagonal boron nitride, in a cost- and labour-efficient way. The transfer of the two-dimensional materials is achieved through electrochemical delamination in an ionic solution. The produced layers can be arranged on SiO_2 wafers, and a vertical heterostructure of graphene and hexagonal boron nitride are built.

In an alternative an more time efficient attempt to produce the heterostructure devices, a direct growth-approach of the full heterostructure is presented. The grown heterostructures were studied by photoelectron spectroscopy and tunnelling microscopy methods before being transferred on SiO_2 and then studied by optical microscopy and Raman spectroscopy. The combination of the two complementary measurement methods gives new insights into the in-situ growth mechanics of graphene on boron nitride heterostructures.

The growth on 4-inch wafers, and the electrochemical delamination process is not only limited to graphene and hexagonal boron nitride. The developed procedures were equally applied to transition metal dichalcogenides, which are materials of high interest for their optical-electronic properties. The growth of a molybdenum-diselenide heterostructure on hexagonal boron nitride is presented and the transfer of the complete heterostructures is demonstrated. The result is a few-layer molybdenum-diselenide on hexagonal boron nitride heterostate on SiO_2 which may be used for optoelectronic device applications.

Contents

1 Introduction **1**

1.1 sp^2 layers: graphene and hexagonal boron nitride 1

1.2 Scope of this thesis 3

2 Experimental Methods **5**

2.1 Chemical Vapor Deposition (CVD) 5

2.1.1 Synthesis of graphene and *h*-BN by CVD on 4-inch wafers 6

2.2 Photoemission 8

2.2.1 X-ray Photoelectron Spectroscopy (XPS) 12

2.2.2 X-ray Photoelectron Diffraction XPD 13

2.2.3 Angle Resolved Photoelectron Spectroscopy (ARPES) 14

2.3 Low Energy Electron Diffraction (LEED) 17

2.4 Scanning Tunneling Microscopy (STM) 18

2.5 Raman Spectroscopy 20

3 Electronic transport measurement of graphene on SiO$_2$ and g/h-BN/SiO$_2$ heterostructures **25**

3.1 Introduction 25

3.2 Properties of graphene and hexagonal boron nitride 26

3.3 Electronic transport measurements 30
  3.3.1 The Electrical Resistivity 30
  3.3.2 Simplest case model 31
  3.3.3 Van der Pauw theorem: isotropic samples of arbitrary shape . . . 35
  3.3.4 The Hall voltage 38
  3.3.5 The charge carrier mobility 41
3.4 Delamination of graphene and hexagonal boron nitride 42
3.5 The 4-point probe setup 43
3.6 Transport measurements of g/SiO_2 46
3.7 Ex-situ prepared hexagonal boron nitride heterostructures 48
  3.7.1 Sample preparation 48
  3.7.2 Characterisation 50
3.8 Conclusions 54

4 In situ prepared graphene - hexagonal boron nitride heterostructures 59
4.1 Introduction 59
4.2 Paper Draft: Growth and characterisation of carbon - *h*-BN millimeter sized heterostructures on Rh(111) wafers and SiO_2 chips 61
  4.2.1 Abstract 61
  4.2.2 Experimental 62
    4.2.2.1 Growth Conditions 62
    4.2.2.2 Sample Characterisation 63
  4.2.3 Results 63
    4.2.3.1 Optical Microscopy 64
    4.2.3.2 Raman Spectroscopy 67
    4.2.3.3 Scanning Tunnelling Microscopy 70
    4.2.3.4 Photoemission of the pristine sample 73

4.2.3.5 Photoemission of the transferred sample 78
4.2.4 Conclusions 79
4.3 Supplementary Information 83
4.3.1 Optical image contrast analysis 83
4.3.2 Angular Resolved Photoelectron Spectroscopy 84
4.3.3 Transfer ratio 86
4.3.4 Possible origin of the C_2 peak 88

5 Molybdenum Diselenide on hexagonal Boron Nitride: A new heterostructure 93
5.1 Introduction 94
5.2 Stoichiometry 96
5.2.1 Graphical Solution 102
5.2.2 Analytic Solution 106
5.3 Material Structure: LEED and XPD 108
5.4 Exfoliation 115
5.5 Discussion 117

6 Conclusions and Outlook 121
6.1 Conclusions 121
6.2 Outlook 124

1 Introduction

1.1 sp^2 layers: graphene and hexagonal boron nitride

The discovery of *graphene* dates back to H.P. Boehm in 1962 which observed the one atom thick structure by TEM analysis and published these findings with the title “Das Adsorpitonsverhalten sehr dünner Kohlenstoff-Folien “[1]. Later he named the discovered structure with the name graphene [2], as the Nobel prize recognised researcher André Geim writes in his publication about the history of graphene [3].

Graphene consists of a one atom thick layer of carbon, arranged in a honeycomb structure bond together in sp^2 hybridized atomic orbitals. The essential breakthrough to investigate the electronic properties of graphene happened decades later, when a single sheet was made visible on a SiO_2 substrate [4]. With a visible graphene layer, it was possible to electrically contact the thin film and measure its properties including graphene’s particular property, namely the variation of the charge carrier concentration under the influence on an applied electric field. Furthermore, graphene possesses surprisingly high charge carrier mobilities compared to conventional field effect transistors based on silicon [5], [6]. Several research results demonstrating the field effect transistor application of the devices were later published concentrating on mechanically exfoliated material [7], [8].

Further research revealed improvements in the charge carrier mobility and application possibilities for graphene in association with hexagonal boron nitride [9], which is, as graphene, a one-atom thick layer of nitrogen and boron atoms arranged in a honeycomb structure. While structural properties of hexagonal boron nitride are similar to graphene, the electronic properties are radically different: hexagonal boron nitride is a large band gap insulator. The similarity of the two structures thus renders the *h*-BN an ideal companion material for graphene, allowing encapsulation and other device applications. This has drawn the attention of scientific and industrial communities.

The use of graphene in industrial applications is hindered by the tedious process of mechanical exfoliation of the graphene sheets. The mechanical exfoliation is labour intensive and cannot be upscaled to mass production [10]. An alternative method to the mechanical exfoliation consists in the synthesis by chemical vapour deposition, which can be performed for graphene [11], [12], [13] and hexagonal boron nitride [14], [15], [16]. This chemical growth processes are performed on single crystals which are both cost intensive to produce and usually do not allow chemical treatments to delaminate the grown graphene or *h*-BN. Thin film foils were used as a remedy to this complication and several research articles have been published presenting graphene and *h*-BN growth on thin copper or platinum [17], [18], [19], [20].

In the same way also the growth of graphene - *h*-BN heterostructures on thin film foils was investigated. The attempts include layer by layer delamination of the graphene and the hexagonal boron nitride [21], [22], and direct CVD approaches to grow the graphene directly on *h*-BN [23], [24] in a vertical arrangement or next to *h*-BN in a lateral arrangement [25], [26]. These heterostructures were used for applications of simple *h*-BN graphene devices [27], [28], [29].

Considering these potential applications, the development of large area high quality single crystalline transferred graphene and *h*-BN material is a central demand in the technological development in the field of electronics. The exploration of different sources of two dimensional material for cost, labour and complexity reduction remains a challenge for the scientific community.

1.2 Scope of this thesis

In this thesis, we use single-crystalline thin film samples on a silicon (111) wafer with a $100 - 200$ nm rhodium or iridium cover layer in a (111) orientation [30], [31], called *sinergia films*. The sinergia wafers are produced in a specialised laboratory set up within the sinergia grant. These crystalline wafers have a 4-inch size and can be prepared by CVD in full size, producing approximately 64 10×10 mm^2 samples of graphene or h-BN in one preparation cycle. The structure of sinergia films, the growth of graphene and h-BN is shown in chapter 2 and embedded in the experimental methods.

In chapter 3 these samples are used to produce transferred layers of graphene and h-BN. The transfer is done by an electrochemical delamination process which allows the delamination of the layers and transport to SiO_2 substrates, following the method of Koefoed et al. [32], [18]. The transfer of single layers, grown on the single crystalline sinergia films, realises a scalable process to produce heterostructure samples with manifold arrangement options, as the relative rotation of the graphene layer relative to the h-BN orientation. The transport properties of such a device in terms of charge carrier mobility is studied using a home built 4-point probe setup. The devices have a size in the order of few square millimeters up to a square centimeter, which demonstrates the scalability of the process.

In an alternative approach to grow graphene - h-BN heterostructures a direct in-situ growth approach is presented in chapter 4. After the growth of a h-BN layer on rhodium sinergia films the wafer is exposed to a millibar pressure CVD cycle as described by Roth et al. [24], [33] to enable the growth of a heterostructure. The samples were characterised by photoelectron spectroscopy, photoelectron diffraction and scanning tunnelling microscopy were the growth of a lateral heterostructure is evidenced. The heterostructure is subsequently transferred on a SiO_2 chip with 90 nm oxide thickness for further characterisations using optical microscopy and Raman spectroscopy. The comparison between the results form photoemission, and optical measurements allow conclusions on the grown heterostructure and assert the advantages and disadvantages of the graphene and *h*-BN growth on thin film sinergia samples, and the used transfer and growth methods.

In chapter 5 the growth of heterostructures on the *h*-BN sinergia samples was extended to transition metal dichalcogenides. Molybdenum diselenide can be grown on the *h*-BN substrates by molecular beam epitaxy. The grown samples were analysed to measure the layer thickness and the structure of the molybdenum diselenide structure. The samples were subsequently delaminated to probe to enable Raman and luminescence measurements, which were summarised in a publication [34].

2 Experimental Methods

In this chapter, the experimental methods used for this thesis are presented. The thesis was completed using mainly the sinergia laboratory [30] for the growth processes of the samples and the ESCA laboratory of the University of Zurich [35] for the photoelectron spectroscopy and diffraction studies. Additionally, in the sinergia laboratory, the optical microscopy and the electron transport measurements were carried out. Some samples subsequently were also characterised at the PEARL endstation of the Swiss Light Source (SLS) at the Paul Scherrer Institute, where a higher resolution for the electron spectroscopy was available, and the possibility of energy-resolved photoelectron diffraction was used. At the Department for Mechanical and Process Engineering (D-MAVT) mainly Raman investigations were performed. In the following subchapters, the methods will be presented independently from the used laboratory. The method of electronic transport characterisation will be discussed in chapter 3, in order to give a deeper insight and detail.

2.1 Chemical Vapor Deposition (CVD)

Chemical Vapor Deposition is a growth process used in the semiconductor industry, to produce thin films of diverse materials. The process is usually performed in an ultra-high vacuum to reduce contaminations and oxidations from the air. The technique requires precursor molecules which are admitted to the vacuum chamber. The substrate, on which the thin film has to be grown, is heated to a temperature which allows the precursor molecule to react with the substrate and assemble in the desired way. The process involves the adsorption of the precursor molecule on the surface, the cracking of the molecule, the migration of the cracking products on the surface, and the self-assembly of a new structure. The process is illustrated in figure 2.1. CVD methods represent the most promising way for the production of scalable industrially practicable growth of 2-dimensional materials as graphene and hexagonal boron nitride [36], [37], [38].

2.1.1 Synthesis of graphene and h-BN by CVD on 4-inch wafers

The synthesis of graphene and h-BN in this thesis uniquely relays on the CVD method, using borazine [39] $(HBNH)_3$ as a precursor for the h-BN production and ethylene [40] C_2H_4 or 3-pentanone [41] $C_5H_{10}O$ for the synthesis of graphene. The used substrates are 4-inch wafers, consisting of a basis Si(111) p-doped wafer with a 20 nm buffer layer of yttria-stabilised-zirconia (YSZ) [42]. On top of the YSZ, a 100-200 nm thick layer of rhodium or iridium was deposited. The metallic layer was grown epitaxially with an fcc(111) top face and low defects [43], [44]. In the following these wafers are called “sinergia wafers“.

Sinergia wafers were used to grow graphene and h-BN by CVD, where graphene was grown on the iridium- while the h-BN on the rhodium coated wafers. The metals act as a catalysts for the cracking process of the precursor molecules. The CVD growth process terminates automatically when the metal is fully covered by a h-BN or graphene layer, as the metal catalyst is no longer available for the cracking process [45], [46].

All CVD preparations were performed using a standard cleaning procedure before CVD evaporation which includes:

1. Ar^+ sputtering with $E = 1\ keV$ discharge energy for 10 minutes.
2. Annealing to a temperature of $T = 1075\ K$ for 60 minutes.
3. Oxygen dosing with a pressure of $p = 1 \cdot 10^{-7}\ mbar$ for 30 minutes.
4. Flashing to a temperature of $T = 1175\ K$ for 20 minutes.

The cycle was repeated at least three times, and until the pressure in the vacuum chamber drops below $1 \cdot 10^{-9}\ mbar$ during flashing. The precursor molecules were introduced at a sample temperature of $T = 1125\ K$ into the chamber, in a stepwise fashion, allowing for slow a growth on few nucleation seeds, of the graphene or *h*-BN layers respectively. The allowed pressure was $p = 1{\cdot}10^{-9}\ mbar$ initially and was increased by half order of magnitude every 10 minutes to reach an end pressure of $p = 1{\cdot}10^{-7}\ mbar$. To avoid cracks caused by thermal contraction stress the wafers were cooled down over a period of at least 60 minutes. The process for the two used structures is visible in figure 2.1.

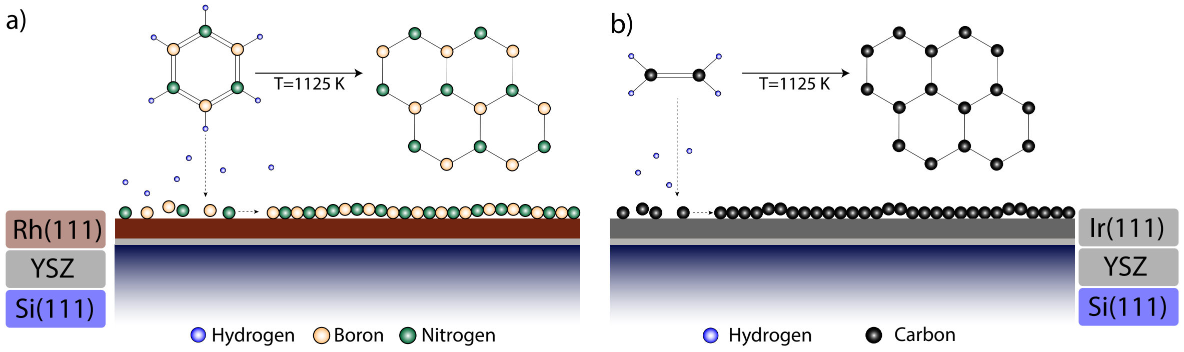

Figure 2.1 Illustration of the CVD process for a) *h*-BN growth on rhodium b) graphene growth on iridium. The image is for illustrative purpose and is not to scale with reality. The CVD process involves the adsorption of a precursor molecule on the surface, the cracking of the molecule through high temperature, the migration of the cracking products on the surface and self-assembly to the 2-dimensional structure.

In the further sections, the examples of h-BN and graphene will be used to illustrate the presented methods.

2.2 Photoemission

One of the most significant results of modern science at the beginning of the 20th century was the explanation of the photoelectric effect, which revealed the quantum nature of light in its fundamental mechanics and the particle-wave dualism of electrons [47]. The discovery of the photoelectric effect can be attributed mainly to Heinrich Hertz [48] for the observation of the photoelectric effect, Albert Einstein [49] for its explanation. These findings are the main contributions which allow scientists these days to use photoemission as an investigative tool to analyse chemical compositions of material and their structure by the use of light and electrons. The mechanism of interaction between light and matter can be explained by the electromagnetic interaction of the light wave with the electrons. Light quanta of a specific frequency can be absorbed by an electron, which will remain in an excited state. This effect is observable on the matter with the photoemission experiment, where light illuminating a metal will emit electrons from its surface only if the light has a sufficiently small wavelength, or in other words, carries enough energy per photon to allow the electron to be emitted from the solid. The equation which can be postulated form this observation is:

$$E_K = \hbar\omega - E_B - \Phi, \tag{2.1}$$

Where E_K ist the kinetic energy which the electron possesses after the emission process, $h\nu$ the energy of the illuminating light quanta, E_B the energy which binds the electron to the atomic nucleus and Φ the work function which corresponds to the minimum energy the electron has to harvest in order to be emitted into the vacuum. This last term becomes necessary as the binding energy E_B is usually referenced to the Fermi energy. The Fermi energy of a material is the highest occupied state energy and is usually the edge of the valence band in metals.

The Fermi energy level and the vacuum energy level have a difference which is the work function Φ. To be emitted from a solid an electron needs to have an equal or higher final state energy as the vacuum level. Equation 2.1 thus satisfies the emission of an electron from an energetic point of view. This simple view of photoemission although does not include any other consideration like the emission angle, momentum conservation or interaction with the material.

The detailed emission process of the electron can be described in various ways. Here we present a semi-classical way called the three-step model, which includes considerations on the electron momentum and simple interaction with the material. The following description and the more extensive quantum mechanical model can be found in the well-known monograph “Photoelectron Spectroscopy “[50].

The three-step model: The emission process of the electron may be described with three different steps which the electron has to fulfill in order to be emitted:

1. Absorption of a photon with the energy $h\nu$ by the electron. This leads to an electronic transition from a bound state $|\Psi_i\rangle$ with an energy E_B to a final state $|\Psi_f\rangle$ with kinetic energy E_K.

2. Transport through the solid as a wave vector with magnitude $|\vec{k}| = \sqrt{2m(E_k + V_0)/\hbar^2}$, where V_0 is the energy difference between the energy level of the bound state and the vacuum energy (E_O) level $V_0 = \Phi + E_F - E_O$. The electron can scatter elastically and can be dampened with exponential progression in respect to the emission

path length. The exponential constant in this process is called the inelastic mean free path Λ.

3. Emission from the material surface into the vacuum where the electron has to overcome the surface potential step. This energy barrier reduces the perpendicular component of the electron wave vector $k_\perp$ while the parallel component $k_{||}$ remains unchanged. The effect is a refraction of the wave, in analogy to geometrical optics.

The parallel momentum can thus be calculated and has the form:

$$k_{||} = \frac{\sqrt{2mE_K} \cdot \sin(\theta)}{\hbar} \cdot \vec{e_s} \tag{2.2}$$

with the polar emission angle θ in the vacuum with respect to the sample normal. From the final state energy E_f the perpendicular momentum inside the solid $k^s_\perp$ can be obtained, with the condition that the inner potential V_0 is known, which is a priori not the case:

$$\vec{k}^s_\perp = \frac{\sqrt{2m(E_K + V_0)}\cos(\theta_i)}{\hbar} \cdot \vec{e_z}. \tag{2.3}$$

Where $\vec{e_z}$ is a vector in normal direction respect to the sample surface.

To emphasise the analogy to geometrical optics, the two equations can be summarised in Snell's law for electron refraction on a solid vacuum interface:

$$\frac{\sin\theta^s}{\sin\theta} = \sqrt{\frac{E_k}{E_k + V_0}}. \tag{2.4}$$

The energy and momentum conservation relation are visualised in figure 2.2.

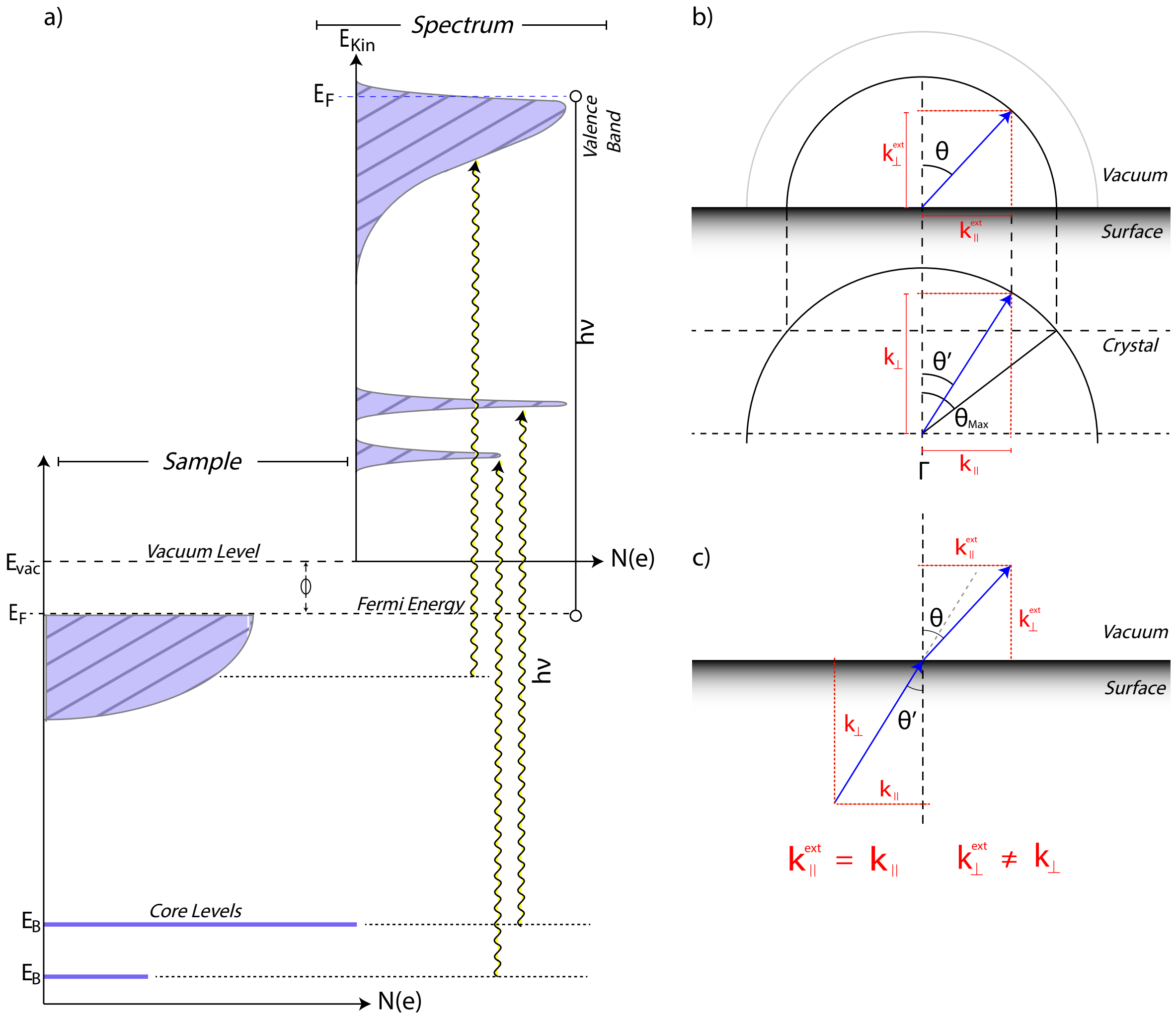

Figure 2.2 Schematic view of the photoemission process. a) shows the relation between the measured photoemission of a sample and the electron energy levels in the sample. The sample occupies electronic levels up to the Fermi energy in the valence bands. More bound states are called core levels. The energy gap between the Fermi energy E_F and the vacuum energy E_{vac} is the work function Φ. Electrons may absorb a photon of the energy $h\nu$ and be emitted if the energy conservation expressed in equation 2.1 is fulfilled. b) Schematic view of the exit condition for a photoelectron concerning of momentum conservation. The total momentum of the electron is shown in blue, the parallel and perpendicular components of the momentum are shown in red. The two semi-circles represent the internal and external escape cones. c) Schematic view of the momentum change at the solid-vacuum interface where the parallel component is conserved while the perpendicular changes through the interface. Figures adapted form [50], [51].

2.2.1 X-ray Photoelectron Spectroscopy (XPS)

Photoemission is a photon in electron out process. The emitted electron thus carries the information of the absorbed photon and the information of the initial state $|\Psi_i\rangle$. The technique of measuring the final state of the emitted electron $|\Psi_f\rangle$ in the photoemission process can reveal pieces of information about the initial state of the electron and thus about the material from which the electron is emitted. This technique is commonly called Electron Spectroscopy for Chemical Analysis (ESCA) or XPS method and involves the use of an x-ray light source and an electron energy analyser under ultra-high vacuum conditions [52], [53]. Based on the choice of the energy the method can be very surface sensitive as the energy of the photoelectron final-state depends on the exciting photon energy and this determines the photoelectron mean free path Λ.

Under adequate measurement circumstances and correct equipment, the information carried by the final state electron allows to determine the initial state binding energy E_B. When scanned over a wide energy range the resulting photoelectron spectrum is a fingerprint of the chemical composition of the analysed material. Equally the intensity of the measured signal, with the consideration of the source intensity and the photoemission cross-section, is bound to the density and quantity of the illuminated material on a sample, thus allowing for quantitative analysis of the measured material [54]. The knowledge of the inelastic mean free path Γ also allows to estimate the thickness of the examined material [55].

Two examples are shown in figure 2.3, where, in a) the XPS spectrum of a *h*-BN CVD preparation on a rhodium sinergia 4-inch wafer is shown. Instead, the illustration b) the XPS spectrum of a graphene CVD preparation on an iridium sinergia 4-inch wafer.

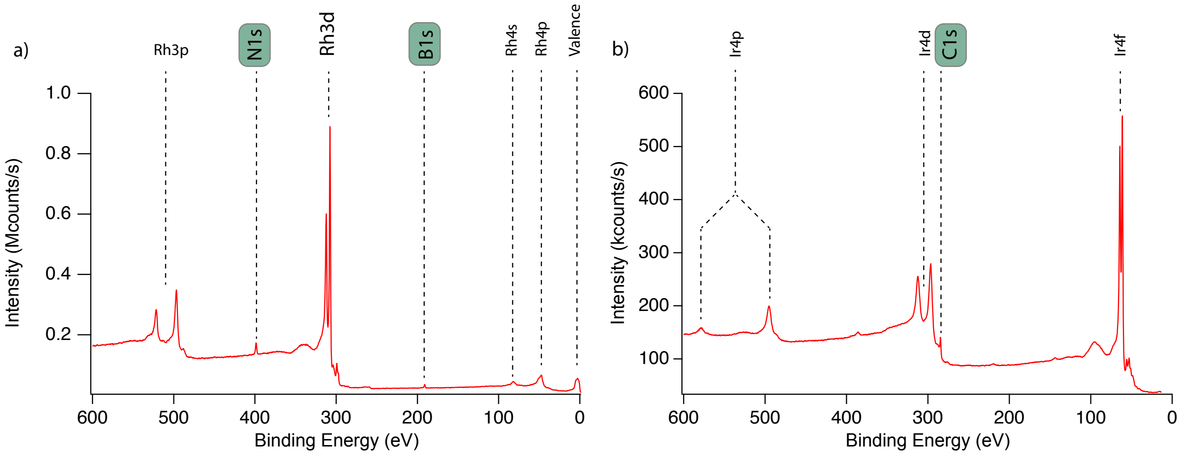

Figure 2.3 XPS survey spectra of CVD prepared taken using a MgK_α source with 1253.6 eV photon energy. a) h-BN/Rh(111)/YSZ/Si(111) sinergia 4-inch wafer b) g/Ir(111)/YSZ/Si(111) sinergia 4-inch wafer.

2.2.2 X-ray Photoelectron Diffraction XPD

A more involved technique to gather information about the sample with a photon in electron out method is represented by x-ray photoelectron diffraction XPD. As described in the three-step model and illustrated in figure 2.2 the photoelectron will travel through the solid as a wave before emission at the surface. During the propagation through the solid, the electron has a probability of scattering elastically at atomic sites of the solid lattice, resulting in a self-interference. The intensity distribution measured over the sample hemisphere varies as a result of the interference patterns of elastically scattered electrons. The pattern is found to carry the information about the lattice structure of the analysed material, an intensity map over the sample hemisphere allows thus to reconstruct the lattice of the material [56], [57]. Especially for energies above $E_K > 200$ eV the forward scattering processes dominate allowing for efficient recognition of the lattice configuration. For this purpose, a pattern can also be calculated starting from a theoretical lattice arrangement using single or multiple scattering theory which is implemented in simulation software as Electron Diffraction in Atomic Clusters (EDAC) [58]. The scattering process is shown in the sketch in figure 2.4 a).

As the patterns are recorded over a hemisphere, a suitable map projection has to be chosen for the visualisation on the bidimensional media such as paper. The commonly used projection for XPD is the stereographic projection, where the center of the map corresponds to the normal emission angle in respect to the sample ($\theta = 0°$). The polar coordinate is transformed into a radial coordinate of the circular plot ($\rho \propto \tan\left(\frac{\theta}{2}\right)$). The outermost ring of the circular plot is thus the maximum polar angle measured. The azimuthal coordinate, on the other hand, is left unchanged. The stereographic mapping has the advantage, over other projection methods, to be conformal and preserve the angles in the transformation, allowing for the direct interpretation of scattering angles in the XPD pattern. The transformation is sketched for two dimensions in figure 2.4 b).

2.2.3 Angle Resolved Photoelectron Spectroscopy (ARPES)

In section 2.2.1 the emission mechanism of a photoelectron from the solid has been presented through the three-step approximation. The final formula for the parallel and perpendicular momentum of the emitted photoelectrons have thus been derived, where the parallel component of the momentum $\vec{k}$ is conserved during the emission process, while the perpendicular component of the momentum will not be conserved.

The conservation of the parallel momentum is beneficial for the analysis of 2-dimensional materials, as their electronic states will disperse only along the parallel momentum component $\vec{k}_{\parallel}$. In this case the complete electronic band structure $A(E, \vec{k_x}, \vec{k_y})$ can be obtained in an ARPES experiment by measuring the photoemission intensity as a function of E_{kin} and the polar angle θ, where $\vec{k_x}$ is the momentum orthogonal to $\vec{k_y}$ which are respectively parallel to the sample plane.

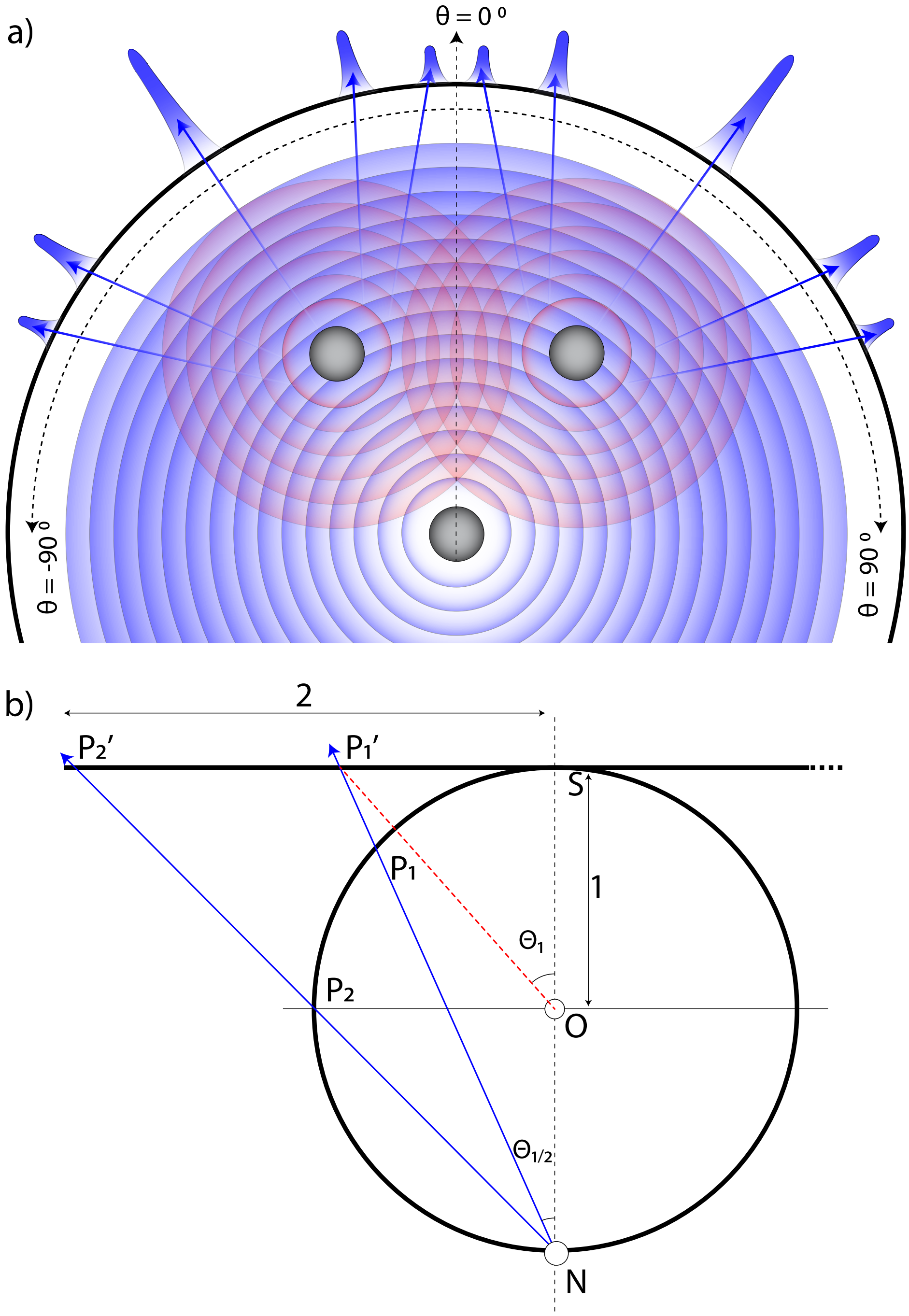

Figure 2.4 In a) sketch of the XPD diffraction process. The central atom (called emitter) emits an electron wave which propagates through the solid (blue waves). Next neighbouring atoms will scatter the wave (red waves). The coherent sum of the scattered and emitted waves generate interference fringes which can be recorded over the sample hemisphere and is visualised by blue Gaussian peaks. In b) sketch of the stereographic projection. The circle represents the hemisphere of data. The data is projected starting from the point (N) on the screen (S). The two points (P_1) and (P_2) are projected to (P_1') and (P_2') through a line starting from (N).

The expressions for $\vec{k_x}$ and $\vec{k_y}$ can thus be expressed as:

$$k_x\ [\text{Å}^{-1}] = 0.5123 \cdot \sqrt{E_{kin}[eV]}\sin(\theta)\cos(\phi) \tag{2.5}$$

$$k_y[\text{Å}^{-1}] = 0.5123 \cdot \sqrt{E_{kin}[eV]}\sin(\theta)\sin(\phi) \tag{2.6}$$

Where θ represents the polar and ϕ the azimuthal angle respect to the sample as shown in figure 2.2.

In figure 2.5 an example of ARPES measurement on graphene on an iridium substrate, measured by M.Kralj et al. [59] is shown. Visible is the intensive Dirac cone dispersing linearly towards the Fermi energy at the K point of the Brillouin zone, which is a fingerprint of the graphene dispersion relation.

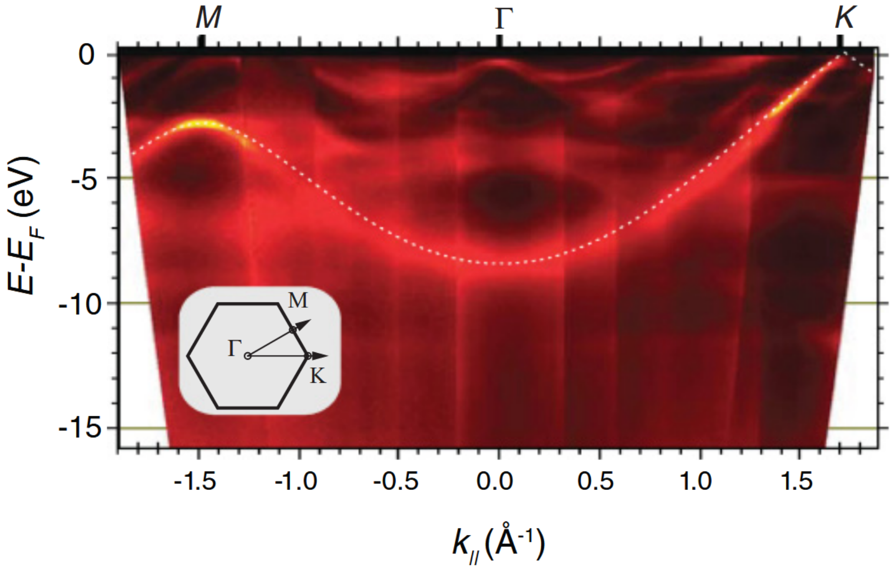

Figure 2.5 ARPES measurement of graphene on iridium g/Ir(111) taken form [59].

2.3 Low Energy Electron Diffraction (LEED)

Davisson and Germer in 1927 discovered low-energy electrons backscattered by an oxidised nickel surface [60]. The intensity distribution of the backscattered electrons was not uniform. The explanation for the effect was the interference of the scattered electrons on the periodic crystalline structure of the nickel surface. A diffraction effect arises as the de Broglie wavelength of the scattered electrons is in the order of magnitude of the periodic lattice of the surface.

The setup of a LEED consists in an electron gun with sufficient energy resolution and a collimated beam, a fluorescent screen to detect the electrons and a retarding grid to select the elastically scattered electrons. A sketch of the setup can be seen in figure 2.6.

The kinematic scattering theory can explain the physical mechanism behind LEED. An incident electron will have a wave vector of $\vec{k_{in}} = (2\pi/\lambda_{in})\ e_{\vec{k_{in}}}$ while the scattered electron will have a different wave vector $\vec{k_{scatt}} = (2\pi/\lambda_{scatt})\ e_{\vec{k_{scatt}}}$. Scattered electrons which fulfill the Laue rule will satisfy the condition for constructive interference. The Laue condition states [61]:

$$\vec{k_{scatt}} - \vec{k_{in}} = \vec{G_{hkl}} \tag{2.7}$$

Where $\vec{G_{hkl}}$ is a vector of the reciprocal lattice and $\vec{e}$ the directional unity vectors. Since only elastic scattering is contemplated, the magnitude of the scattered and the incident wave vectors must be equal. The Laue condition can thus be visualised with the construction of the Ewald sphere shown in 2.6 b), which is the sphere that the wave vector k_{in} describes. Each intersection of the Ewald sphere and the reciprocal lattice rods represents a diffracted beam and generates so-called Bragg reflections on the measurement screen.

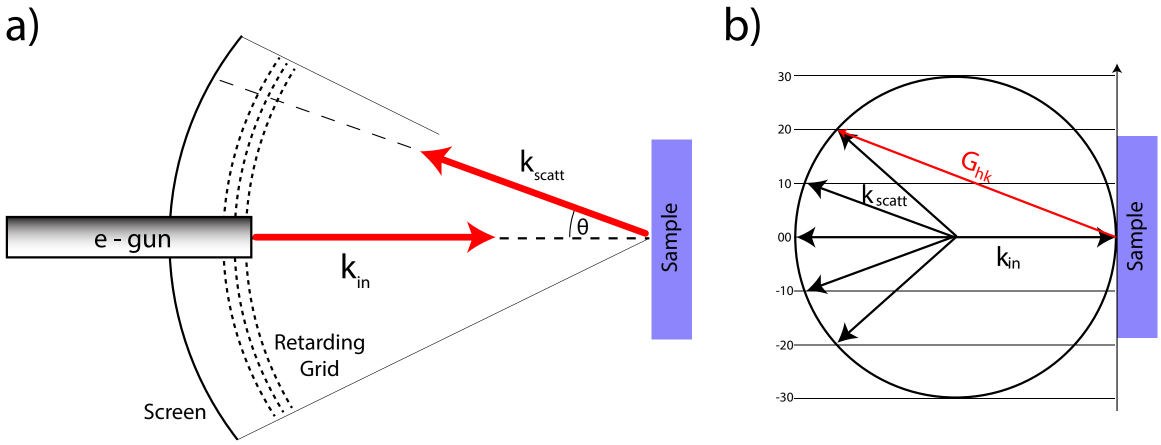

Figure 2.6 In a) setup of a LEED technique which is placed in vacuum. b) Scattering mechanism of the electrons fulfilling the Laue condition.

The examples for the h-BN/Rh(111)/YSZ/Si(111) and the g/Ir(111)/YSZ/Si(111) are shown in figure 2.7 where the LEED patterns, measured at 70 eV electron energy, of the h-BN is shown in a) and the graphene in b). The diffraction patterns were taken with a CCD camera and inverted in the image processing. The figures show the principal Bragg spots of the rhodium and iridium surfaces respectively, which are marked with the markers (Rh) and (Ir). The finer structure marked with (S) corresponds to the superstructure periodicity of the h-BN (13 boron and nitrogen atoms on 12 rhodium atoms) and graphene (10 carbon atoms on 9 iridium atoms). Further insights into the LEED techniques can be found in the monograph “Physics at Surfaces“[62].

2.4 Scanning Tunneling Microscopy (STM)

Scanning Tunnelling Microscopy (STM) is a surface sensitive method to investigate the structural arrangement of atoms or molecules on surfaces developed by G.Binning and H.Rohrer in 1981 [63]. The technique involves an atomically sharp metallic tip (usually tungsten or platinum-iridium) which is brought to the immediate vicinity of a surface. The distance d is usually less than a nanometer, on which a bias voltage V_B is applied.

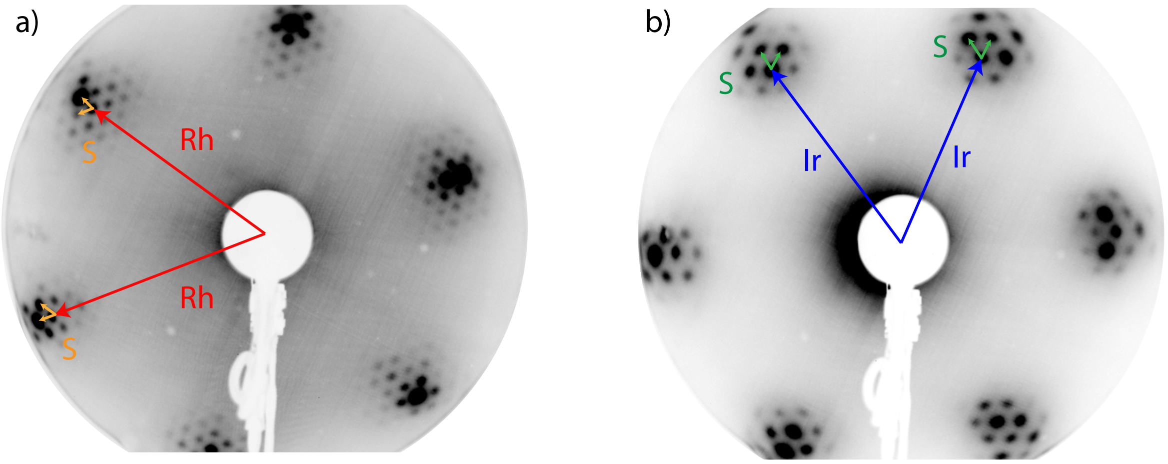

Figure 2.7 In a) LEED image of *h*-BN/Rh(111) and in b) of g/Ir(111). In both images the markers (Rh) and (Ir) show the reciprocal lattice vectors of the substrate, while the markers (S) show the reciprocal lattice vectors of the superstructure, which arises form the incommensurate growth of the 2d-materials on these substrates.

With this small gap d, the electron wave functions of the tip states and the sample states overlap. This overlap and the applied voltage results in a current I_t flowing between the tip and the sample. The process can be explained assuming the gap d as a rectangular energy barrier formed by the vacuum between tip and sample and the solution of the one dimensional Schrödinger equation [64], which yields a tunnelling current of:

$$I_t \propto \exp\{-2\kappa d\}, \quad \text{where} \quad \kappa = \sqrt{2m(\Phi - E)/\hbar^2} \tag{2.8}$$

Where m is the mass of the tunnelling electron, Φ is the tunnelling barrier height, E is the energy of the tunnelling electron respect to the Fermi energy E_F and κ is the so-called Gamov factor. Further theoretical calculations about the tunnelling mechanism of STM might be found in the publication “theory of the scanning tunnelling microscope “ [65].

Recording the tunnelling current while moving the tip in a raster over the sample allows to produce a current image of the sample which is a mapping of the density of states (DOS). This STM mode is called constant height mode and is not practical except in particular applications. The commonly used mode is the constant current mode where a feedback loop between tunnelling current and the motors driving the z-axis of the tip controls the distance d of the tip respect to the surface. The STM electronics can so adequately react to topographic changes and features on the sample to reduce the risk of tip crashes. The sharpness of the images will depend upon the sharpness of the tip, vibration isolation of the STM apparatus and measurement temperature. A simplified working mechanism for the STM is shown in figure 2.8 while a measurement example for graphene on rhodium is shown in figure 2.9.

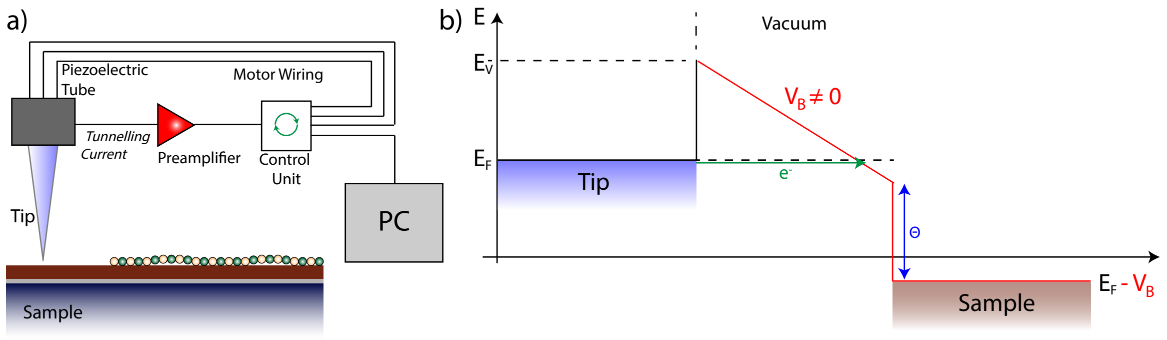

Figure 2.8 Setup of an STM. In a) control mechanism is shown. The tunnelling current of the tip is pre-amplified and, with the input of the user by a computer, transduced to a movement for the piezoelectric tube. The measured image is the z-height of the tip. b) A simplified model of the tunnelling in an STM junction, showing the electron sea of the tip at the Fermi energy, the tunnelling junction in the vacuum which will be at vacuum energy level and the electron sea of the sample at Fermi energy. If a bias voltage is applied the Fermi levels of the sample (or tip) can be modified, resulting in a narrower tunnelling barrier. The electrons will have higher tunnelling probability.

2.5 Raman Spectroscopy

Raman spectroscopy is a photon in photon out measurement technique which uses an inelastic scattering process of light with matter. A light quantum $h\nu$ hitting a molecule, may scatter elastically through Rayleigh scattering or inelastically through Raman scattering. The latter process has a much lower probability. The Raman scattering of light quanta can excite or relax vibrational states in a molecule [66]. The scattered light

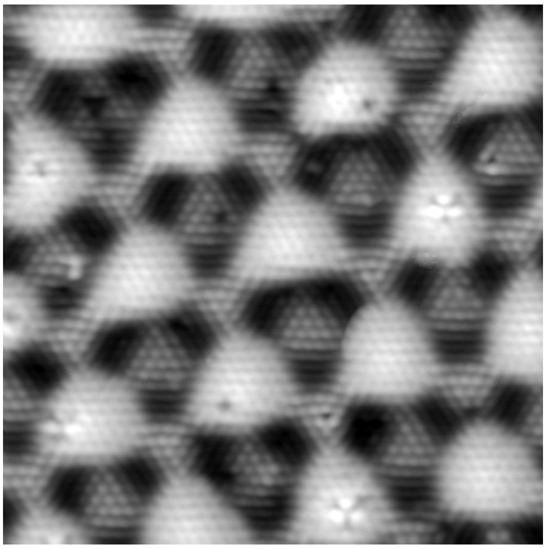

Figure 2.9 Example of a graphene on rhodium STM measurement. The triangular bright shapes are height modulations induced from the incommensurate growth on rhodium. The small periodic structure within the bright and dark regions represent single atoms.

quanta's have thus an energy of $h\nu \pm h\nu_S$. The excitation mechanism, where the scattered photon carries less energy $h\nu - h\nu_S$, is the predominant at room temperature ($k_B T = 25\ meV$ or 201.6 cm^{-1}), as most vibrational modes are in their ground states under these conditions [67].

Sir George Stokes and Sir Chandrasekhara Venkata Raman observed deviations in the wavelength of light when it interacts with matter [68]. These wavelength changes are referred to as Stokes lines, for lines which are lower in frequency as the exciting light (while anti-Stokes lines are higher in frequency). Only stokes lines are measured in Raman scattering since their intensity is much higher. The mechanism of Raman scattering is sketched in figure 2.10 a), where the stokes and anti-Stokes excitation mechanisms are illustrated.

In graphene, the Raman scattering modes are called G, D and 2D modes. These modes arise from different excitation mechanisms. Using a photon wavelength of $\lambda = 532\ nm$, the G mode appears at $E_G = 1582\ cm^{-1}$, and is the most characteristic feature of graphene and various after carbon compounds. Analogously, for *h*-BN, the same mode is located at $E_{2G} = 1366\ cm^{-1}$ but it is much less intensive. [69], [70], [71]. The G band rises from photons exciting electrons at the Brillouin zone center generating an electron-hole pair. The electron (or hole) may scatter through an iTO or iLO phonon and recombine with the emission of a photon with lower wavelength [72]. The iTO and iLO phonons are associated with the bond stretching of the carbon bonds at the Γ point as visible in figure 2.10 c).

The D modes ($E_D = 1620\ cm^{-1}$), instead, originate from the scattering of photons at a defect site and relax through an iLO phonon or an iTO phonon. The D mode can give an insight on the azimuthal disorder or defect density of the analysed graphene sheet, in perfect crystalline graphene the D mode should be absent [73], [74].

The 2D mode ($E_{2D} = 2700\ cm^{-1}$) is the most active feature in Raman spectroscopy on graphene and originates from an in-plane breathing motion of the honeycomb carbon network as shown in figure 2.10 c) and is located at the K point of the Brillouin zone. The process involves the scattering of an electron or a hole from a K to an energy degenerate K' point of the Brillouin zone, shown in 2.10 b). The backscattering for the recombination of the electron-hole pair equally happens through phonon scattering, in order to fulfill energy and momentum conservation. In the presence of multilayer graphene, the 2D mode splits in multiple peak structures, as the excitation and scattering processes also involve the additional π-bands originating from the additional layers. Examples of measurements for graphene are shown in figure 2.10 b) bottom right which has been taken from the publication of Wu et al. [75]. Two references for a deeper insight into Raman processes in graphene can be found by Beams et al. [76] and Malarad et al. [77].

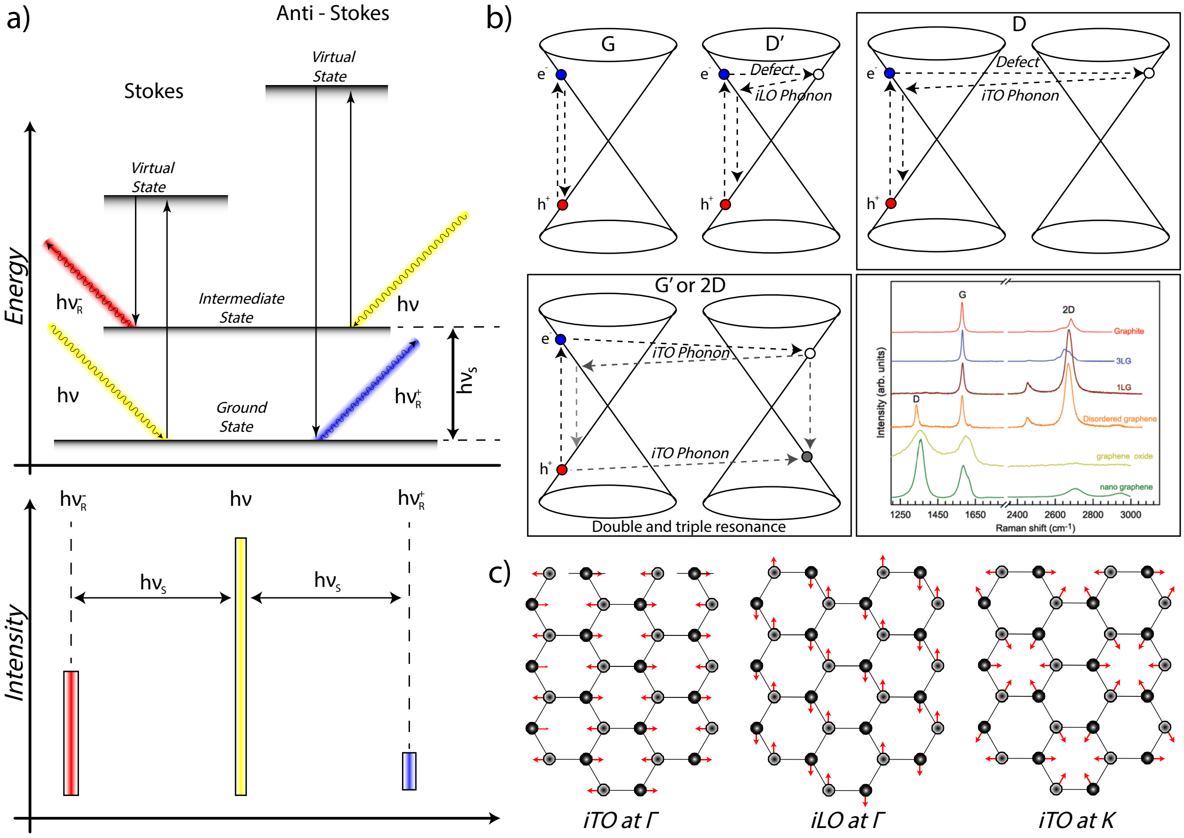

Figure 2.10 In a) mechanism of Raman spectroscopy: in yellow a scattered photon with energy $h\nu$ which is absorbed by the electronic ground state of a system. On the left: the transition of an electron from the ground state to a virtual state through the excitation of the photon and relaxation in an intermediate state and emission of a photon with $h\nu - h\nu_S$. The energy difference between incoming and scattered light is the Stokes energy. On the right, the same mechanism is sketched for the anti-Stokes lines. In the bottom subfigure, the intensity ratios are sketched for the Stokes and anti-Stokes lines. In b) possible excitation mechanisms of an electron in graphene, involving defect states of the lattice and phonon excitation to fulfill the momentum conservation. In the subfigure on the right bottom, examples of Raman spectra for different graphene allotropes, taken from [75] are shown. In c) the phonon vibration mechanics of the involved Raman modes in graphene.

3 Electronic transport measurement of graphene on SiO_2 and g/h-BN/SiO_2 heterostructures

3.1 Introduction

In this chapter, the investigation of electronic properties of graphene and h-BN is discussed. For this purpose, a description of the electronic structure of h-BN and graphene is included, and the details of resistivity and mobility measurements reported. In a second part, a technique to delaminate h-BN and graphene from their metallic substrates is introduced. This technique allows the transfer of the sp^2 materials to insulating substrates which are suitable for electronic measurements. The transport measurements were carried out in a home-built 4-point probe experiment setup. The transfer mechanism has been applied to graphene and h-BN, allowing the construction of vertical heterostructures which can be arranged as desired. These heterostructures have been characterised by spectroscopic techniques and electronic transport measurements.

3.2 Properties of graphene and hexagonal boron nitride

The crystal structure of h-BN and graphene is very similar. Both materials consist of a honeycomb lattice, where each atom is connected to three neighbours through σ bonds in the hybridised sp^2 orbitals. These orbitals reside below the Fermi level. The additional valence electron per atom populates the π band, which disperses towards the Fermi energy. The anti-bonding π^* band is empty when the system is at $T = 0$ K. At room temperature electrons in graphene can populate the π^* band and enable conduction of charges through the material.

h-BN instead equally bonds in a honeycomb lattice through σ bonds in sp^2 orbitals. Albeit, the different electron affinity of boron and nitrogen leads to a different band structure than graphene, in particular, a large band gap of $E_G \simeq 5.8$ eV makes h-BN to be an insulator [78], [79].

The band structure of graphene can be calculated using the tight binding model. The explanation of the peculiar band structure of graphene can be assigned to Wallace et al. [80], in the process of explaining the band structure of graphite. Graphite consists of multiple stacked layers of graphene in a so-called Bernal stacking sequence [81]. The approach by Wallace was to assume that the interlayer distance of graphite to be big ($l = 3.37$ Å) compared to the hexagonal spacing in the single layer $d = 1.42$ Å[82]. The structure for graphene and h-BN are shown in figure 3.1.

The Bravais lattice contains two atoms per unit cell, which are called A and B atoms. This signifies two hexagonal sub-lattices to reside in the graphene honeycomb. The lattice vectors can be written as:

$$\vec{a_1} = \frac{a}{2}(3, \sqrt{3}) \quad \text{and} \quad \vec{a_2} = \frac{a}{2}(3, -\sqrt{3}) \tag{3.1}$$

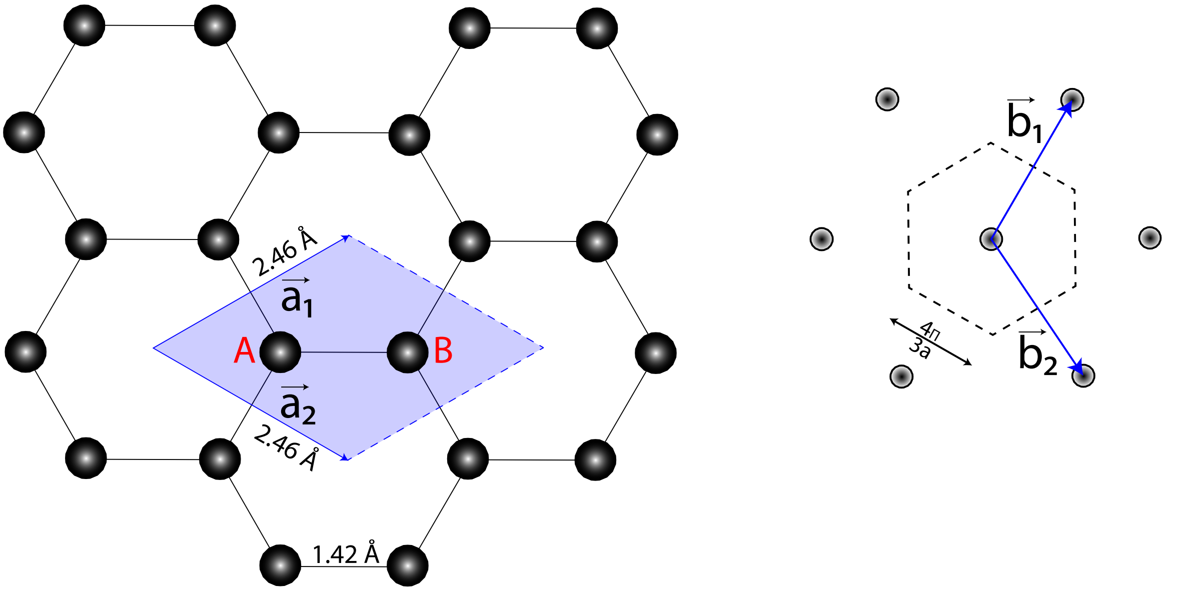

Figure 3.1 Sketch of the hexagonal honeycomb structure of graphene in real space (left) and reciprocal space (right) showing the first Brillouin zone. The color shaded area is the primitive cell of the structure.

From which the reciprocal lattice vectors can be calculated:

$$\vec{b_1} = \frac{2\pi}{3a}(1, -\sqrt{3}) \text{ and } \vec{b_2} = \frac{2\pi}{3a}(1, \sqrt{3}) \tag{3.2}$$

Where a is the distance between the carbon atoms. The tight binding Hamiltonian for the two sublattices has to be considered, where the therms H_{AA} and H_{BB} describe the energy of the two separate lattices while the therms H_{AB} describe the hopping of an electron from one sublattice to the other. The eigenvalue problem will thus be:

$$\begin{pmatrix} H_{AA} & H_{AB} \\ H_{AB} & H_{BB} \end{pmatrix} \Psi = E \ \Psi \tag{3.3}$$

Using the Bloch theorem and therefore assuming the wavefunction of the electrons to be:

$$\Psi(r) = e^{i\vec{k}\cdot\vec{r}} u(\vec{r}) \tag{3.4}$$

the eigenvalues of the Schrödinger equation can be computed and yield:

$$E(k) = \pm\sqrt{\gamma_0^2(1 + 4\cos^2\frac{k_y a}{2} + 4\cos\frac{k_y a}{2} + 4\cos\frac{k_x\sqrt{3}a}{2})} \tag{3.5}$$

where the positive solution describes the antibonding π^* orbital and the negative solution the bonding π orbital. As graphene possesses two delocalised electrons, these fill the π band while the π^* remains empty. A plot of the band structure of graphene is shown in figure 3.2, which is taken from [6] where a detailed calculation of the band structure is offered.

The intersection point of the two bands is called Dirac point and is located at the border of the Brillouin zone in the K and K' points. The shape of the band structure around the Dirac point can be described as two cones pointing to each other, where the apices meet in the Dirac point. These cones are called Dirac cones.

The dispersion relation $E(k)$ around the Dirac cones is linear. This deviates from the typical parabolic dispersion relation $E(k) = \hbar^2k^2/(2m^*)$ found for free electrons in metals and semiconductors. Instead, the dispersion relation in the vicinity of the Dirac points is linear. The dispersion relation can be written in a simplified form which is only valid in the vicinity of the Dirac point and states:

$$E(k) = \pm h|k|v_F \tag{3.6}$$

where is the Fermi velocity $v_F \simeq 10^6\ m/s$ and k is measured from the Dirac point. The effective mass m^* with a linear dispersion is undetermined.

$$\frac{1}{m^*} = \frac{1}{\hbar^2}\frac{\partial^2 E(k)}{\partial k^2} = 0\ . \tag{3.7}$$

A similar conclusion can be reached in considering electrons in graphene to be relativistic. We substitute $p = hk$ in the relativistic expression for the energy and assume $v_F = c$:

$$E^2 = (pc)^2 + (m_0 c^2)^2 = (hkc)^2 + (m_0 c^2)^2 \quad \rightarrow \quad m_0 = 0 \tag{3.8}$$

This is the sense electrons and holes in graphene are called “massless“.

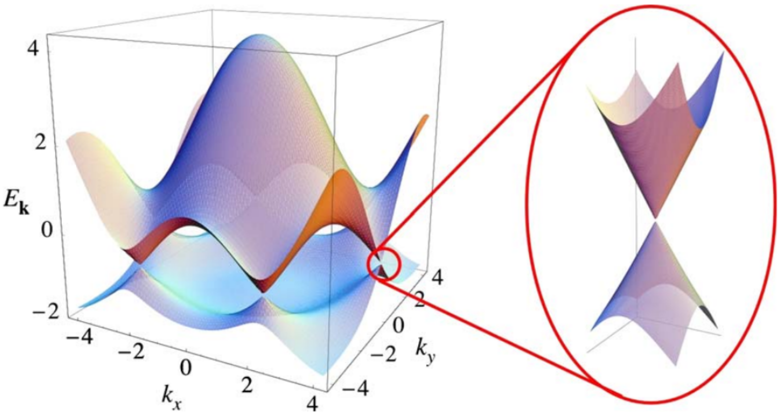

Figure 3.2 Dispersion relation of graphene. Figure taken form [6].

These findings suggest that graphene has high electron mobility which in case can reach 10000 cm^2/Vs [5] and higher [83]. Although the high mobility values are only valid for freestanding graphene with no interaction from the substrate, where the two graphene sublattices are symmetric. This symmetry leads to a zero energy difference between the highest occupied energy level and the lowest unoccupied energy level, where this difference is commonly called *band-gap*. Substrate interactions may lift the degeneracy of the K and K' energy levels, which in freestanding graphene are equal [84]. In the case of graphene on Ni(111) this degeneracy is lifted, as the matching of the lattice constants allows the p_z orbitals of graphene to hybridise with the Ni3d orbitals [85], opening a band gap of 3 eV [86]. The delamination of the graphene, form the metal substrate, becomes thus a crucial step for the characterisation of electronic properties.

3.3 Electronic transport measurements

To understand the properties and behavior of materials, it is essential to conduct investigations on a macroscopic scale, which is not reduced to the analysis of a single unit cell. A way to achieve this is the measurement of the electronic transport properties, like the resistivity (namely the behavior of an electric charge under the influence of an electric field in the material); the Hall coefficient (information about the electron dynamics) giving access to the charge carrier mobility and the charge carrier density, which is the number of available mobile charge carriers per unit volume. Those methods are important Keys for the jump from the nano-scale to macroscopic behaviour. In our case the materials of interest are mainly graphene g and *h*-BN.

3.3.1 The Electrical Resistivity

To measure the resistivity of a sample we need to quantify the physical proportionality factor which relates the electrical current I to the applied electrostatic field E. We shall represent the resistivity with the symbol ρ. The relation between the electrostatic field and the electrical current is given by:

$$E\ [Vcm^{-1}] = \rho\ [\Omega cm]\ J\ [Acm^{-2}] \tag{3.9}$$

Where J is the current density per unit area and E is the electrostatic field. Analyzing the units of the equation one gets for the resistivity $\Omega = V/A$ which is the unit for the resistivity and is called *Ohm* per unit length. This equation is analogue to *Ohms law*:

$$U\ [V] = R\ [\Omega] I[A] \tag{3.10}$$

Where R is the measured resistance of the sample in units of *Ohm*.

The difference between *resistance* and *resistivity* can be explained as follows. The resistance R, in contrary to the resistivity, does still include geometrical factors of the contact arrangement or the resistance induced by the contacts itself. In a simple example, if two contacts are used to measure resistance with a commercially available multimeter, the multimeter induces a test current to the sample, and the corresponding voltage drop is measured. The quotient between these two values is the sum of resistances of the sample, the resistance of the contacts and the resistance of the cabling. The measured resistance is:

$$R_{tot} = R_s + R_c + R_i \tag{3.11}$$

Where R_s is the resistance of the sample, R_c the resistance of the contacts and R_i the resistance of the cabling. Hence the measured resistance R_{tot} is only an upper limit approximation of the true resistivity of the sample. Further, the arrangement of the probing contacts can change the measured value substantially. An improvement to this approximative technique is the *four point probe (4PP)* technique, where the test current and the probing contacts are separated. Over the probing contacts ideally no current flows (ideal infinite impedance), such that there is no potential drop between device and the probing contacts. So the contribution of the contact and cabling resistances do not influence the measured values [87].

3.3.2 Simplest case model

While the 4PP technique solves the problem of contact and cabling resistances, the issue of the sample- and contact geometry is still open. We will now in the first place consider the simplest geometrical configuration and present a solution to the calculation of the resistivity in this case. Successively a general method called van der Pauw method, valid for any geometry of the sample with anisotropic resistivity is introduced.

The simplest non-trivial case of a 4PP setup for two dimensional materials is to consider a sample with infinite extension (length and width are much larger than the contact spacing), negligible thickness (thickness is much smaller than contact spacings) as sketched in Figure 3.3.

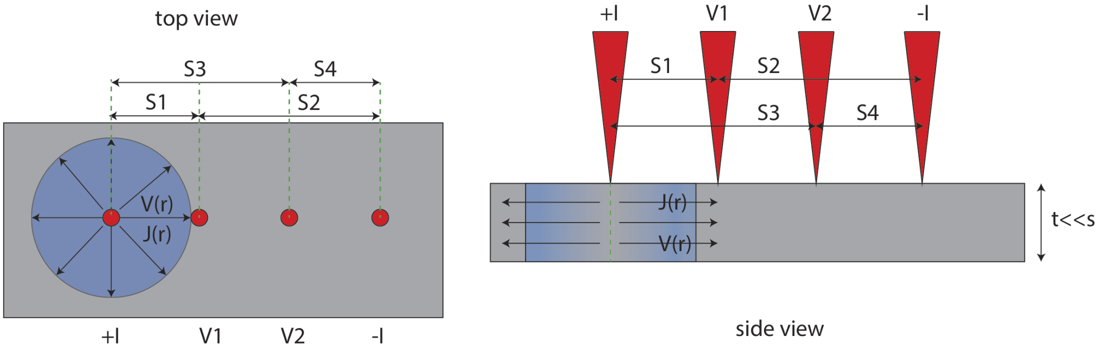

Figure 3.3 Scheme of the setup. Left: top view of the sample, right a side view. In red the contacts in a in-line geometry. The two outer contacts inject the test current while the internal contacts measure a voltage drop. In blue the propagation of the current is modeled as a cylinder. The contact spacing are called S_1, S_2, S_3, S_4

We consider four in line, point-shaped contacts (which have negligible extension compared to the contact spacing). Let the spacing between the contacts be S_i with $i \in \{1, 2, 3, 4\}$. In this configuration, all the current which is introduced in the sample through contact I_+ leaves the sample through contact I_-, and the boundary of the sample do not influence the electrostatic field in the probed sample area, and thus the Gauss law can be applied. A suitable geometry to calculate the potential difference between the contacts V_1 and V_2 can simplify the problem. Convenient geometries are: For 3D samples spherical, while for 2D samples the sphere reduces to cylindrical geometry. The general expression for the resistivity can be written as:

$$\rho = 2\pi S \frac{V}{I} \tag{3.12}$$

Where S is the spacing of the contacts, V the potential drop and I the test current. Assuming the sample to be very thin a cylindrical geometry[1] can be used and the expression which relates the current density and the total current flowing through the cylinder surface can be written as:

$$J(r) = \frac{I}{2\pi r d} \tag{3.13}$$

Where d represents the thickness of the sample. Substituting Equation 3.13 and 3.9 in 3.12 we obtain:

$$E(r) = \rho J = \frac{\rho I}{2\pi r d} = -\frac{dV}{dr} \tag{3.14}$$

Integrating on both sides leads to the general expression for the potential in a distance r:

$$\int_0^V dV = -\frac{\rho I}{2\pi d}\int_0^r \frac{dr}{r} \quad \Rightarrow \quad V(r) = \frac{I\rho}{2\pi d}\ln(r) \tag{3.15}$$

The potential drop between the contacts V_1 and V_2 is given by the potential difference at distance $\Delta S_{12} = S_1 - S_2$ and $\Delta S_{34} = S_3 - S_4$. The equation can thus be rewritten as:

$$\Delta V = V_2 - V_1 = \frac{I\rho}{2\pi d}\ln\left(\frac{S_2 S_3}{S_1 S_4}\right) \tag{3.16}$$

---

[1] Assuming the sample not to be flat we would consider a spherical geometry and expression 3.13 would modify containing the surface of a semi-sphere in the denominator.

Assuming equidistant contacts ($S_i = S$) results in:

$$\rho = \frac{\pi d}{\ln 2} \frac{\Delta V}{I} \tag{3.17}$$

Note: the resistivity is independent from the contact spacing, this is true for two-dimensional materials and a consequence of the dimensionality of the probes. The 2D resistivity is called *sheet resistance* R_s and has the dimension $\Omega_\square$:

$$R_s[\Omega_\square] = \frac{\pi}{\ln 2} \frac{\Delta V}{I} \tag{3.18}$$

If the contacts are arranged in a square geometry as shown in Figure 3.4 with $S_1 = S_4 = S$ and $S_3 = S_4$ the pythagoras theorem leads to $S_{3,4} = \sqrt{S}$. Simplifying Equation 3.16 to:

$$R_s[\Omega_\square] = \frac{2\pi}{\ln 2} \frac{\Delta V}{I} \tag{3.19}$$

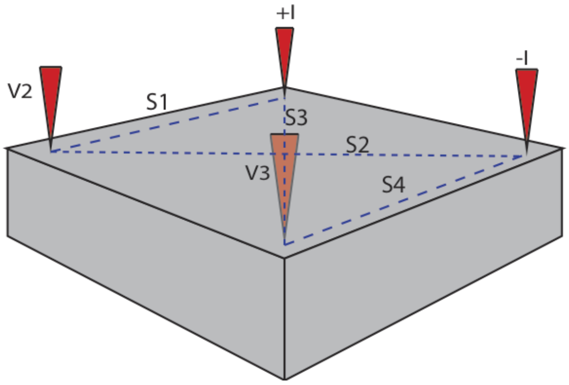

Figure 3.4 Contact arrangement for a square sheet resistance transport measurement setup.

The measurement of the sheet resistance using the equation 3.19 is a significant improvement over the simple measurement of the resistance with a 2-point probe method. Albeit, the equation does not consider geometrical correction factors, as the shape of the sample boundaries, the placement of the contacts and the thickness of the sample (other than the two ideal cases). To solve these limitations, various correction factors were calculated, which became obsolete with the formulation of the *Van der Pauw* theorem, which extends the use of equation 3.19 to samples of arbitrary shape. In the next section the *Van der Pauw* theorem is shown directly while the extensive calculation of the correction factors can be found the extensive publication of Miccoli et. al. [87].

3.3.3 Van der Pauw theorem: isotropic samples of arbitrary shape

The *Van der Pauw* theorem is a substantial improvement because it extends the problem of the sample shape to samples of arbitrary shape.

This improvement is significative if the sample to be measured consists of exfoliated or delaminated 2D materials like graphene or hexagonal boron nitride, where the shape of the flakes is hard to control, or in best case introduces an additional process step of removing excess material by oxygen plasma treatment.

The requirements for the Van der Pauw theorem are the following:

- The sample has to be homogeneous and isotropic.
- No isolated holes or defects in the layer, the layer has to be simply connected[2].
- The sample has to be thin compared to the probe spacing ($t/s < 1/4$).

---

[2] A simply connected sample is not allowed to have holes or discontinuities. The necessary and sufficient requirement for a simply connected space is that given two points in the space and two paths to connect them it must be possible to transform one path into the other continuously preserving the endpoints.

To measure the resistivity of a sample which fulfills these requirements the setup is analogous to the previous cases, with the addition that the contacts are placed on the boundary of the sample. If a probing current is applied between the contacts $I_+ = A$ and $I_- = B$ and the voltage drop is measured on the remaining probes $V_1 = C$ and $V_2 = D$ we can define the following *resistance* measurement:

$$R_{AB}^{CD} = \frac{V^D - V^C}{I_{AB}} = \frac{V^{CD}}{I_{AB}} \tag{3.20}$$

The same measurement can be performed applying the current on the contacts BC and measuring the voltage drop between AD. We obtain two measurement of resistance, namely R_{AB}^{CD} and R_{BC}^{AD}. The Van de Pauw theorem states, that the two resistances have to satisfy following condition:

$$\exp^{-\pi \frac{t}{\rho} R_{AB}^{CD}} + \exp^{-\pi \frac{t}{\rho} R_{BC}^{AD}} = 1 \tag{3.21}$$

If the contacts are placed on lines of symmetry on the sample the reciprocity theorem ensures that $R_{AB}^{CD} = R_{BC}^{AD} = R$ and equation 3.21 is simplified to:

$$\rho = \frac{\pi d}{\ln(2)} \frac{\Delta V}{I} \tag{3.22}$$

In the case of missing symmetry axes on the sample the resistivity can be expressed as:

$$\rho = \frac{\pi d}{\ln(2)} \frac{R_{AB}^{CD} + R_{BC}^{AD}}{2} f \tag{3.23}$$

Where f is a function of the ratio between the two resistances:

$$\cosh\left(\frac{\ln(2)}{f}\frac{R_{AB}^{CD}/R_{BC}^{AD}-1}{R_{AB}^{CD}/R_{BC}^{AD}+1}\right)=\frac{1}{2}\exp\left\{\frac{\ln(2)}{f}\right\} \tag{3.24}$$

The proof of this theorem can be found in the two papers of Van de Pauw [88], [89] and, because of the importance of the theorem, its concept is summarized here.

Let there be an semi-infinite sample with a boundary. The contacts on the boundary will be S, P, Q, R and the distances between the contacts a, b, c, d. The probes are allowed to have arbitrary spacing. Using equation 3.12 we can write for the voltage difference between Q, R:

$$V_R - V_S = \frac{I\rho}{\pi d}\ln\left(\frac{(a+b)(b+c)}{b(a+b+c)}\right) = IR_{SP}^{QR} \tag{3.25}$$

$$V_R - V_S = \frac{I\rho}{\pi d}\ln\left(\frac{(a+b)(b+c)}{ca}\right) = IR_{PQ}^{RS} \tag{3.26}$$

The two resistances on the right hand side have to be equal so we set the middle section into equation and get:

$$(a+b)(b+c) = b(a+b+c) + ca \tag{3.27}$$

The same calculation can be done in a cycle for the other contacts which prove the validity of the equation 3.21. If we apply the theory of conformal mapping, it is possible to show that the theorem is not only valid for a semi-infinite sample, but also for a sample of finite extension and arbitrary shape, as it is always possible to map a closed curve on a straight line. From the theory of conformal mapping [90] the necessary condition of simply connected sample in the Van der Pauw theorem arises, as for a not singly connected sample the conformal mapping theory is not applicable.

The Van de Pauw theorem shows that a measurement at the boundaries of a sample is advantageous as it eliminates the need of correction factors for the geometrical form of the sample.

3.3.4 The Hall voltage

To compute the charge carrier mobility of a sample an additional property has to be investigated, namely the *Hall coefficient.* The Hall coefficient yields information about the behaviour of the charge carriers as a function of a magnetic field. Charged particles which are in motion experience a deflection from their trajectory when a magnetic field is present. This effect is called the *Lorentz* force and can be described by the following Equation [61]:

$$\vec{F} = q(\vec{E} + \vec{v} \times \vec{B}) \tag{3.28}$$

This effect can be observed when a magnetic field is applied perpendicular to a sample with an electrical current. The current paths are deflected in the sample, generating a charge imbalance on one side of the sample. A charge imbalance generates an electric field which counterbalances the effect and generates a potential gradient over the sample. If the voltage is probed, a potential drop can be measured. The parameter called *Hall coefficient* is defined as:

$$R_H = \frac{E_y}{J_x B} \tag{3.29}$$

Where J_x is the current density in the x-direction and E_y the electric field in the y-direction. Considering the Lorentz equation the force can be written in terms of momentum per electron:

$$\frac{d\vec{p}}{dt} = -e(\vec{E} + \frac{\vec{p}}{2m} \times \vec{B}) - \vec{p}/\tau \tag{3.30}$$

Where τ is the mean free path from a Drude type of transport given by $\tau = m/(\rho n e)$, e is the electron charge, ρ is the resistivity and n is the electron density. The current is stationary so the derivative of the momentum is 0 so:

$$0 = -eE_x - \omega_c p_y - p_x/\tau \tag{3.31}$$

$$0 = -eE_y + \omega_c p_x - p_y/\tau \tag{3.32}$$

$\omega_c = eB/m$ is the cyclotron frequency. We multiply the two equations by the current density which is $j = ne\tau/m$:

$$E_x/\rho = \omega_c \tau j_y + j_x \tag{3.33}$$

$$E_y/\rho = -\omega_c \tau j_x + j_y \tag{3.34}$$

The first term yields the microscopic Ohmic law:

$$E_x = \rho J_x \tag{3.35}$$

The second therm describes the electrical field in the y direction of the sample and is the Hall field. In a stationary condition the field balances the Lorentz force of the magnetic field so the current $j_y = 0$. We can rewrite the term for E_y and obtain the Hall coefficient in function of the electron density:

$$E_y = -\omega_c \tau \rho j_x = -\frac{B_z j_x}{ne} \;\Rightarrow\; R_H = -\frac{1}{ne} \tag{3.36}$$

This relation means that the Hall coefficient R_H is only dependent on the three dimensional electron density n and the sign of the charge carrier. Therefore the measurement of the Hall coefficient is the measurement of the charge carrier concentration. The sign of R_H gives information about which type of charge carriers are involved in the electronic transport: When the value is negative the charge is carried by electrons when the value is positive the charge is carried by electron-holes.

To measure the Hall coefficient, the sample is contacted in a square arrangement with two opposing contacts as current inducing contacts and the remaining two perpendicularly arranged contacts as voltage probes. A magnetic field is induced perpendicular to the sample surface and the Hall voltage measured with the voltage probes. The measurement scheme is shown in Figure 3.5.

To measure the electron density of a two-dimensional sample the equation 3.36 has to be corrected in terms of the sample thickness d:

$$R_H = -\frac{d}{n_{2D} e} = \frac{U_H d}{IB} \quad \rightarrow \quad \frac{R_H}{d} = -\frac{1}{n_{2D} e} \tag{3.37}$$

The measured quantity is called the Hall resistance, which is the measured voltage drop in the y-direction normalised by the applied probing current at a fixed magnetic field:

$$\rho_H = \frac{R_H B_z}{d} = \frac{U_H}{I} \tag{3.38}$$

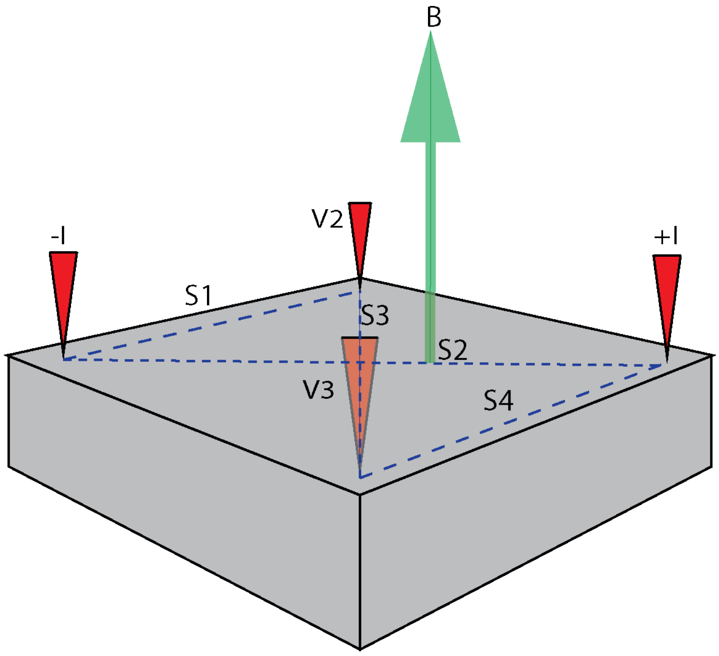

Figure 3.5 Scheme of a Hall measurement. In green the magnetic field and in red the four contacts.

3.3.5 The charge carrier mobility

Once the Hall coefficient and the resistivity of a sample are determined, the charge carrier mobility μ can be computed. The mobility is a quantity which describes the drift velocity of the charge carriers under the influence of an electric field. In general, mobility is defined as:

$$v_d = \mu E \tag{3.39}$$

Where v_d is the drift velocity of the electrons in a material. The mobility can be calculated from the ratio of the Hall coefficient and the sample resistivity:

$$\mu \left[\frac{m^2}{Vs}\right] = \frac{1}{enR_s} = \frac{V_H}{IBR_s} \tag{3.40}$$

3.4 Delamination of graphene and hexagonal boron nitride

As seen in section 3.2, the graphene layers must be separated from metallic growth substrates and moved to a insulating substrate, to obtain transport data of the two-dimensional material.

The delamination process depends on the used substrate where the graphene or h-BN is grown. The delamination consists in a first step, where the strong van der Waals bonding of the graphene or h-BN to the substrate, is lifted. In a second step, the delamination process occurs in a salt solution [18]. Graphene grown on copper substrates may be delaminated directly skipping the first step, as the weak interaction with the copper substrate allows direct delamination.

A sketch of the delamination process is shown in figure 3.6 a). The first step is an electrochemical treatment with a tetraoctylammonium-bromide (TOA-Br) $0.1M$ solution in acetonitrile. The setup of the electrochemical cell is shown in figure 3.6. The migration of the TOA^{+}-ions to the sample interface is facilitated by the application of a bias voltage of $V = -1.9$ V between the working electrode and a silver reference electrode for $t = 10$ min. A subsequent voltage of $V = -0.2$ V is applied to prevent further reactions between the negatively charged graphene and the polymethylacrylate (PMMA) layer which is subsequently applied. The samples were then rinsed with acetonitrile and dried in an inert atmosphere. This treatment has been proven to increase the transfer yield, as the TOA^{+}-ions weaken the van der Waals interaction between graphene (or h-BN) and the substrate [32], [91], [92].

The samples were subsequently coated with 4wt.% PMMA 495 K solution and dried for 12 hours. The PMMA is necessary as a support for the exfoliated layers. The delamination is performed with the bubbling method [18], [17], [93] using two electrodes, where one electrode is a graphite rod and the counter-electrode the sample. A 1 M KCl aqueous solution was used. The sample was polarized to a voltage of -5 V to attract positive H^+ ions and to form H_2 between the layer and the metal. The separation of the PMMA and graphene (or *h*-BN) foil is achieved through water reduction at the metallic sample surface, where:

$$2H_2O(l) + 2e^- \quad \rightarrow \quad H_2(g) + 2OH^-(aq) \tag{3.41}$$

such that H_2 bubbles lift the PMMA-graphene (-*h*-BN) layer.

This layer is subsequently rinsed for 30 minutes in ultra-pure millipore water and deposited on a 10×10 mm^2 SiO_2/Si chip. The removal of the PMMA can be achieved through heating for 12 hours to 400 K, subsequent hot acetone and ethanol baths and a final heating cycle of 30 minutes to 400 K.

The moment of detachment of the PMMA-graphene (*h*-BN) layer is visible in figure 3.6 b), where at marker (A) the delaminated film is visible and at marker (B) the submerged substrate. In figure 3.6 c) a successfully transferred graphene on a $\mathrm{SiO_2}$ substrate with gold markers is shown. At marker (C) a not covered area is shown while at (D) the covered area is visible. The characterisation of the obtained graphene samples can be found in the publication by Miniussi et al. [94].

3.5 The 4-point probe setup

The setup to measure electric resistivity and mobility is shown in figure 3.7. It consists of an ECOPIA sample holder with 4 gold coated sprung contacts [95]. The contacts are called ABCD and are assembled in a quatrefoil geometry. A back-gate contact plate is

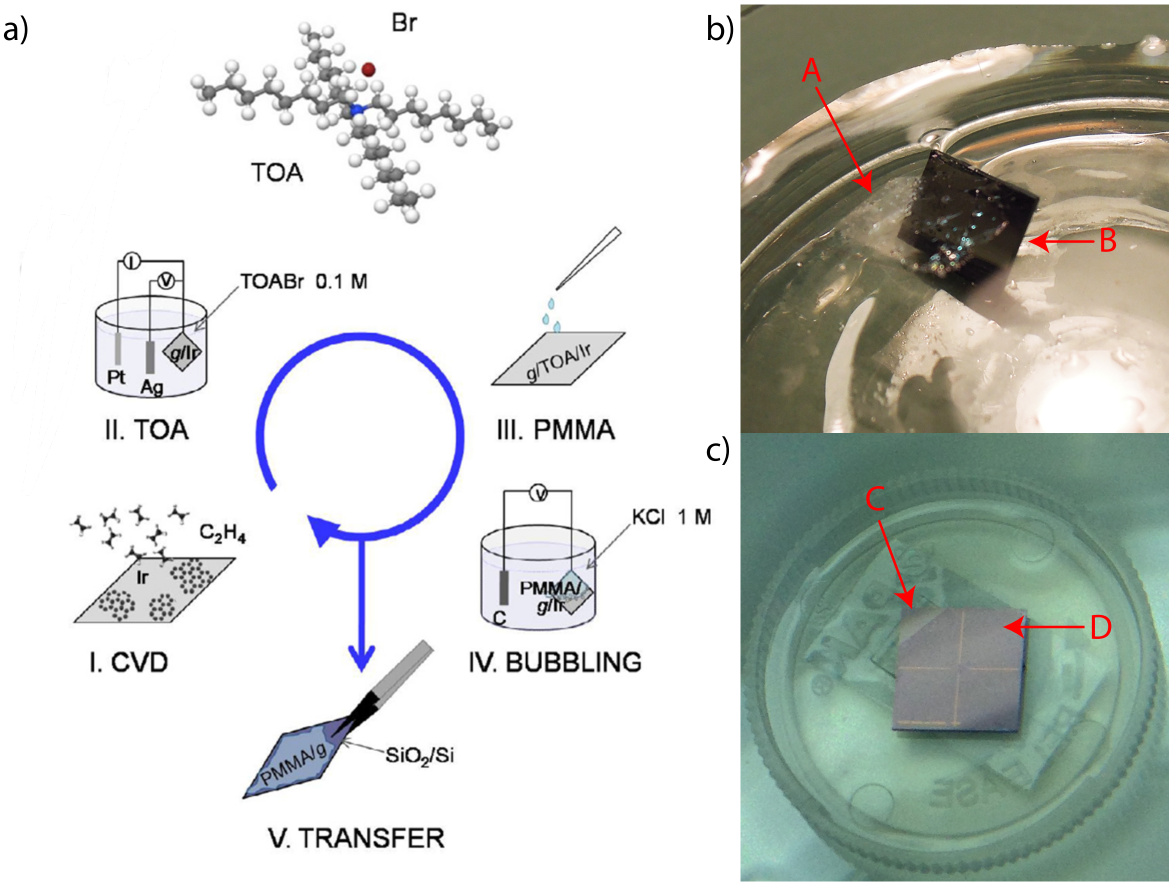

Figure 3.6 a) Sketch of the TOA-pretreatment and the bubbling procedure. Figure taken from [94]. b) Detachment of the PMMA foil with the graphene (A) from the substrate (B). c) Successfully transferred graphene layer, where in (C) the missing edge where the sample was clamped during the bubbling procedure is visible. This missing edge can be used as a marker for the graphene orientation if the growth substrate orientation is known. In (D) the graphene layer after acetone cleaning procedure is visible, the bright cross shaped features are gold markers.

placed on the back of the sample. The sample contacting construct can be closed in a brass mount which can be rotated on the horizontal axis. The mount is placed between the yokes of a GMW electromagnet [96], which can deliver ±1 T magnetic flux density, which is constant in the area where the sample is placed. The electrical scheme is shown on the bottom of figure 3.7. A PC controls a Keithley source-meter through a software measurement script, which generates the probe current and senses the voltage drop. These signals are fed to a switching board, which is controlled by an NI-DAQ digital to analog converter, to permute the four contacting arrangements for the resistivity measurements, and the two for the mobility measurements. The NI-DAQ controls the switching of the measurement arrangement operating on relays in the switching board. Furthermore, the magnetic flux is measured through a Hall probe and the back-gate contact can be addressed. The GMW magnet is controlled by a GPIB connection in the measurement script, or can alternatively be changed manually on the power supply front panel.

A resistivity measurement consists of the permutation of the possible contact arrangements, where two adjacent pins are used as probing current source and drain while the remaining two contacts are used as sensing contacts. For each measurement, the probing current is swept from a minimum to a maximum current. The slope of the obtained voltage drop versus the probing current is thus the measured sheet resistivity for one arrangement. Using equation 3.19 and averaging the obtained sheet resistances, the total sheet resistance of the sample is obtained.

A similar consideration can be done to measure the electron mobility, which is given by equation 3.40. The electron mobility is given by the ratio of the Hall coefficient and the sheet resistance. The sheet resistance has already been measured and calculated. The Hall coefficient, on the other hand, can be measured changing the measurement arrangement, applying a current between two opposing contacts and measuring the voltage drop over contacts placed perpendicular to the probing current. On the out-of-plane axis of the sample, a magnetic field is applied and switched between $B = 1$ T and $B = -1$ T after each resistivity measurement.

Two contact arrangements are possible, the first applying a current across the contacts A and C measuring the voltage drop over contacts B and D for the two opposing magnetic fields, while in the other arrangement the contact pairs are changed. Analogously to the sheet resistance the slope of the voltage drop versus current is calculated and the slopes measured at different magnetic fields compared. The slope difference normalized by the change in magnetic field is the Hall coefficient. The Hall coefficient's that are measured in the two distinct arrangements are averaged and divided by the sheet resistance to obtain the electron (or hole) mobility.

Using equation 3.36 the charge carrier concentration can be calculated, where a net positive carrier concentration indicates a hole carrier type while a negative carrier concentration indicates the charge carrier consists of electrons.

3.6 Transport measurements of g/SiO$_2$

The 4-point probe setup was tested with samples transferred from a commercially available supplier (Graphenea) of graphene on copper [97]. The transfer method for these samples does not include the TOA-Br pretreatment, as from polycrystalline copper samples this procedure is not necessary. A measurement of sheet resistance and charge carrier mobility is shown in figure 3.8. In subfigure a) the resistance measurement of a g/SiO$_2$ sample where the sheet resistance was found to be $R_s = 576.27 \pm 0.31\ \Omega_\square$. The Hall resistance measurement is shown in 3.8 b) and found to be $R_H = 33.5\ \pm\ 1.7\ m^3/C$ which leads to a charge carrier mobility of $\mu = 581\ \ \pm 30\ cm^2/Vs$. From the Hall resistance, the charge carrier density can be computed which in this case is $n_{2D} = 1.86 \cdot 10^{13}\ cm^{-2}$,

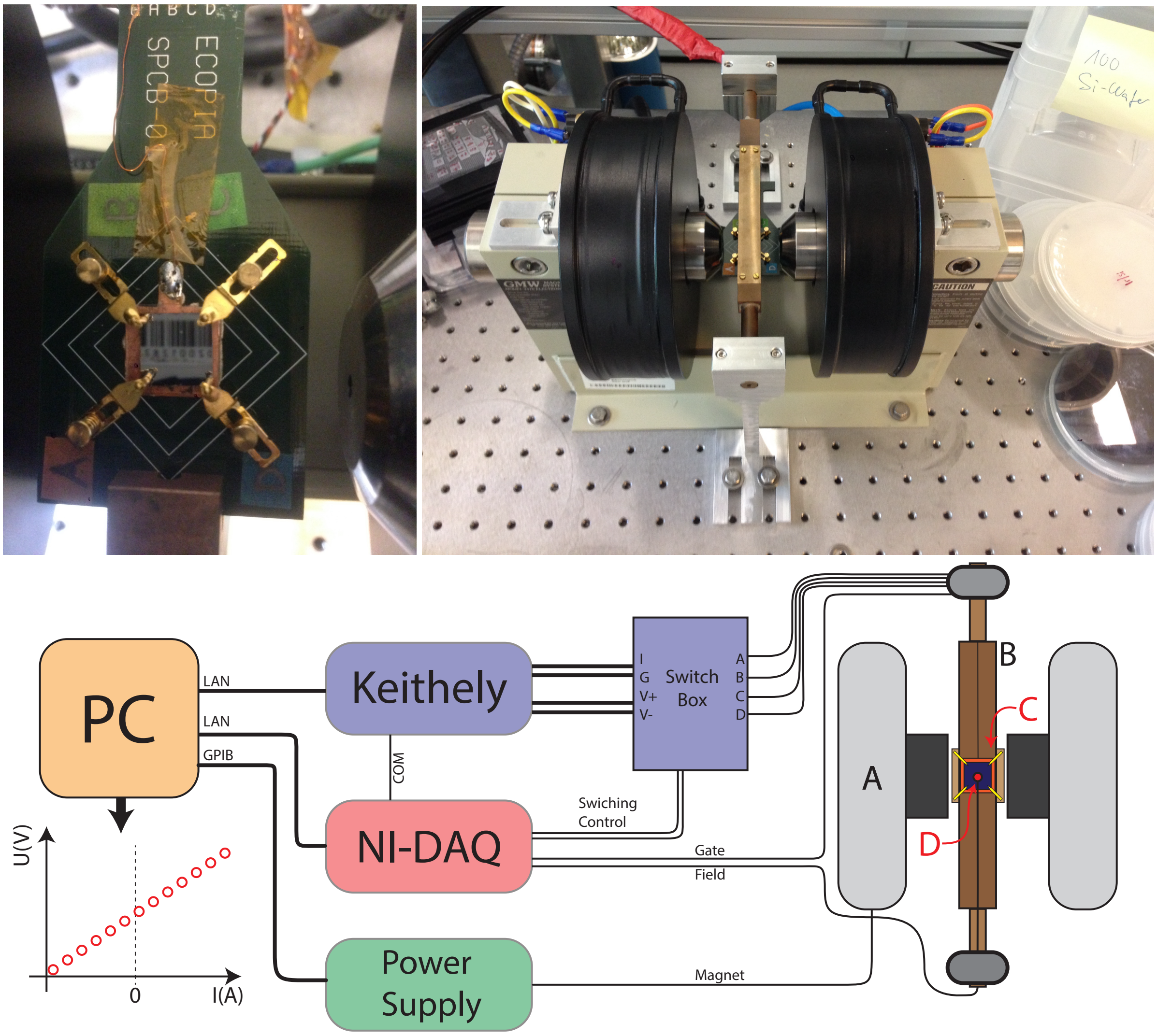

Figure 3.7 Picture of the 4-point probe setup. Top row: contact arrangements with gold coated pins in quatrefoil geometry which is placed between the poles of an electromagnet. The sample holder is made of brass to minimize magnetic interferences. Bottom: sketch of the data acquisition line. The GMW electromagnet is sketched in (A), in (D) the sample is placed while on the backside of the sample a Hall probe is placed to measure the magnetic field. (C) shows the gold sprung contacts of the ECOPIA sample holder visible in the top picture.

measured in charge carriers per centimeter square, as we assume graphene to be a two-dimensional sheet.

3.7 Ex-situ prepared hexagonal boron nitride heterostructures

The delamination of the layers grown on sinergia wafers introduced in chapter 2 can be performed for graphene and h-BN. This allows to manually arrange heterostructures, where the graphene and h-BN order can be chosen. Moreover, the relative orientation of the layers can be chosen in the transfer process. In this subchapter, the construction of two such samples is described. The samples were arranged by transferring a h-BN layer on SiO_2 and subsequently adding a crystalline graphene layer, transferred from an iridium sinergia wafer piece. The orientation between the h-BN and the graphene can be chosen as the wafer orientations are known. The arranged samples have two different relative orientations of graphene respect to the h-BN substrate, namely $\varphi = 40^\circ$ and $\varphi = 0^\circ$.

3.7.1 Sample preparation

The sample growth was performed as described in chapter 2 and it was delaminated with the TOA-Br assisted bubbling method described in section 3.4. As a first step, the h-BN layer was deposited on a SiO_2 chip with an oxide thickness of 90 nm and the cleaning procedure performed. In a second step, the graphene layer was transferred on the h-BN/SiO_2 samples. As the transfer process is performed in a liquid, the chip and the transferred sheet can be aligned in the desired relative angle. Two angles were chosen: a zero-degree and 40-degree relative rotation of the graphene with respect to

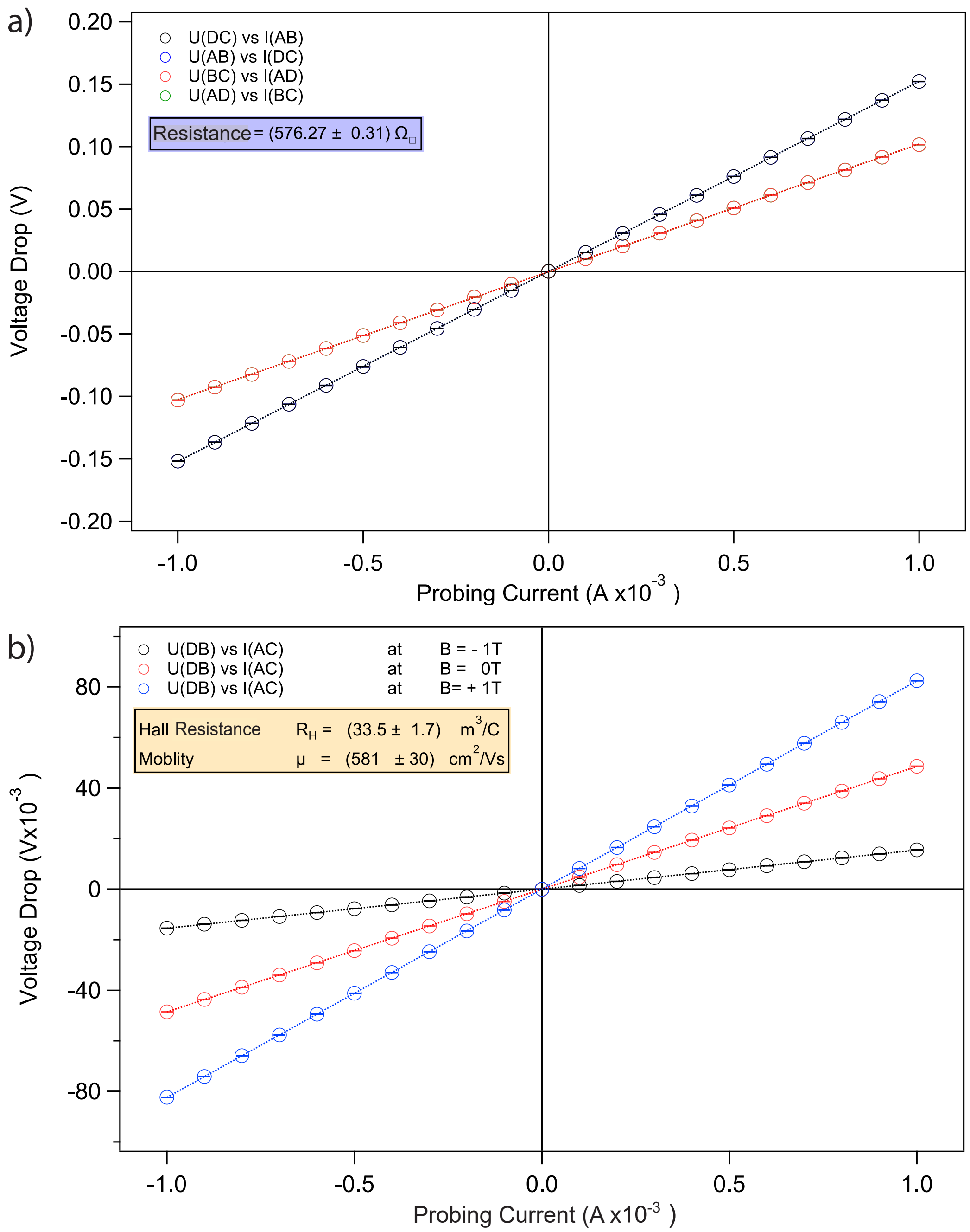

Figure 3.8 Top figure: resistivity measurement on a g/SiO$_2$ sample transferred from polycrystalline copper. The voltage drop respect to the probing current plot is shown for all four measurement configurations. The dashed lines are the linear fits used for the computation of the resistivity. Bottom figure: Hall coefficient measurement of the same sample, the three datasets in black red and blue represent the different magnetic field settings. Only one measurement configuration is shown. The circles are the data points while the dashed line the linear fits used to compute the Hall coefficient the mobility.

the *h*-BN. In the transfer process, a triangular corner of the sample square is cut as a reference for alignment. The alignment process is shown in figure 3.9, where a simple set square was used as a reference. For this reason, the error of the relative angle has to be estimated accordingly high.

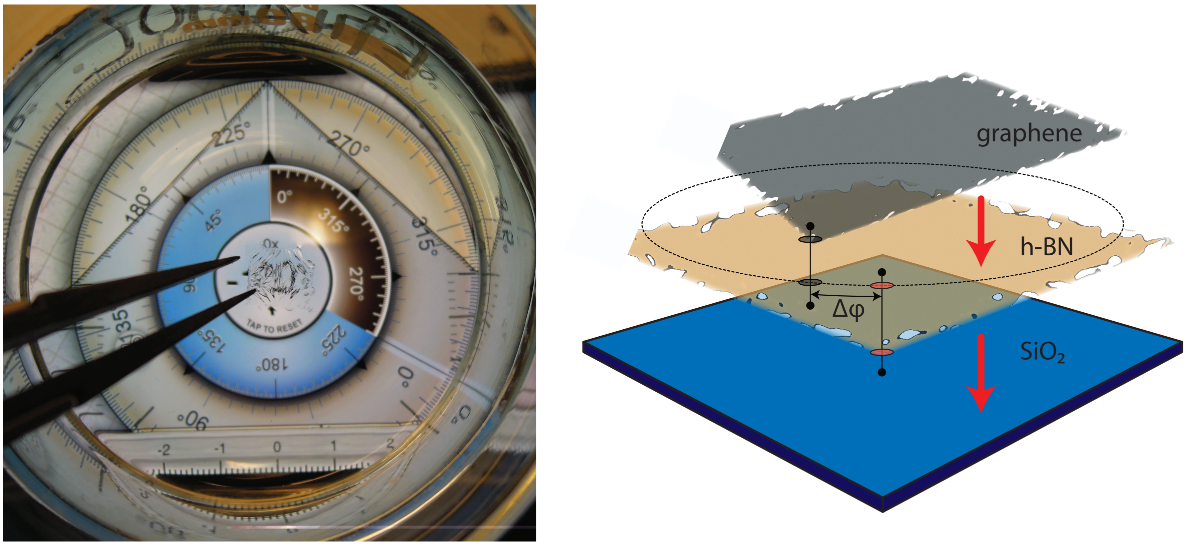

Figure 3.9 On the left side: floating graphene/PMMA suspended layer in ultra-pure water. The layer can be oriented azimuthally taking a set square as a reference, which is visible through the transparent beaker. The graphene is placed on the already prepared *h*-BN/SiO_2 sample (not shown) by picking up the graphene/PMMA layer in the liquid. On the right: staking sequence of the *h*-BN and graphene with an azimuthal relative angle. The missing left corner can be used as a guide for the orientation.

3.7.2 Characterisation

As a first step, the samples were analysed by optical microscopy. The results are shown in figure 3.10, where the optical microscopy images for the sample with a $\varphi = 40°$ relative rotation is shown in a) and the sample with $\varphi = 0°$ relative rotation is shown in b). The borders of the respective layers are highlighted by a yellow dashed line in the case of the *h*-BN-SiO_2 interface and in a red dashed line in case of the graphene-*h*-BN interface. The different contrasts of the *h*-BN layer to the graphene allows for the identification of the two different layer types. The relative rotation of the graphene layers with respect to the h-BN is easily visible in the figures and highlighted by the black arrows. The vertical stacking sequence is set by the mechanical arrangement during the transfer steps and is thus fixed. Other arrangement geometries or capping of the graphene layer are equally possible.

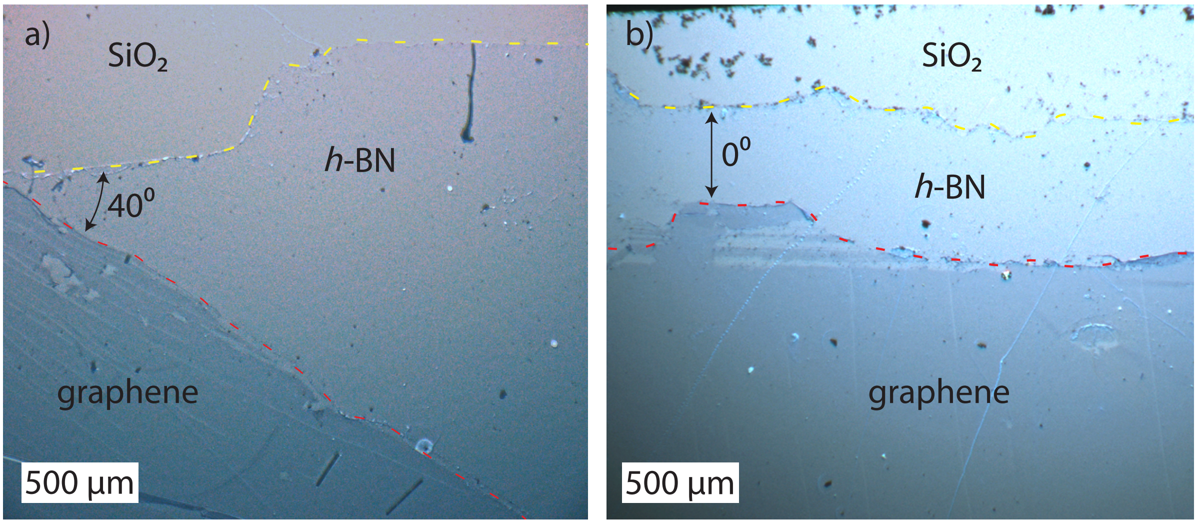

Figure 3.10 Optical microscopy of g/h-BN/SiO$_2$. In a) sample with $\varphi = 40°$ relative rotation and in b) the sample with $\varphi = 0°$ relative rotation.

The presence of graphene and boron nitride is proven by the XPS spectrum shown in figure 3.11, wherein red the spectra for the sample with $\varphi = 0°$ relative rotation and in black the sample with $\varphi = 40°$ relative rotation is shown. The presence of the three species indicates the transfer of h-BN and graphene on the SiO$_2$. The ratio of the carbon intensity in relation to nitrogen intensity is $I_C/I_N = 5.85$ which suggests an excess of carbon on the sample, which may be due to transfer residues. The ratio of nitrogen to boron is $I_N/I_B = 1.04$ which is the stoichiometric value for h-BN, indicating no change in the h-BN composition.

To further prove the presence of graphene on the sample surface, an ARPES measurement of the g/h-BN/SiO$_2$ samples was performed. The figure 3.12 shows the intensity plots in the $\overline{\Gamma K}$ direction in a) for the $\varphi = 40°$ and in d) for the $\varphi = 0°$ relative rotated sample. In the figure a) and d) the linear dispersion of the π towards the Fermi energy,

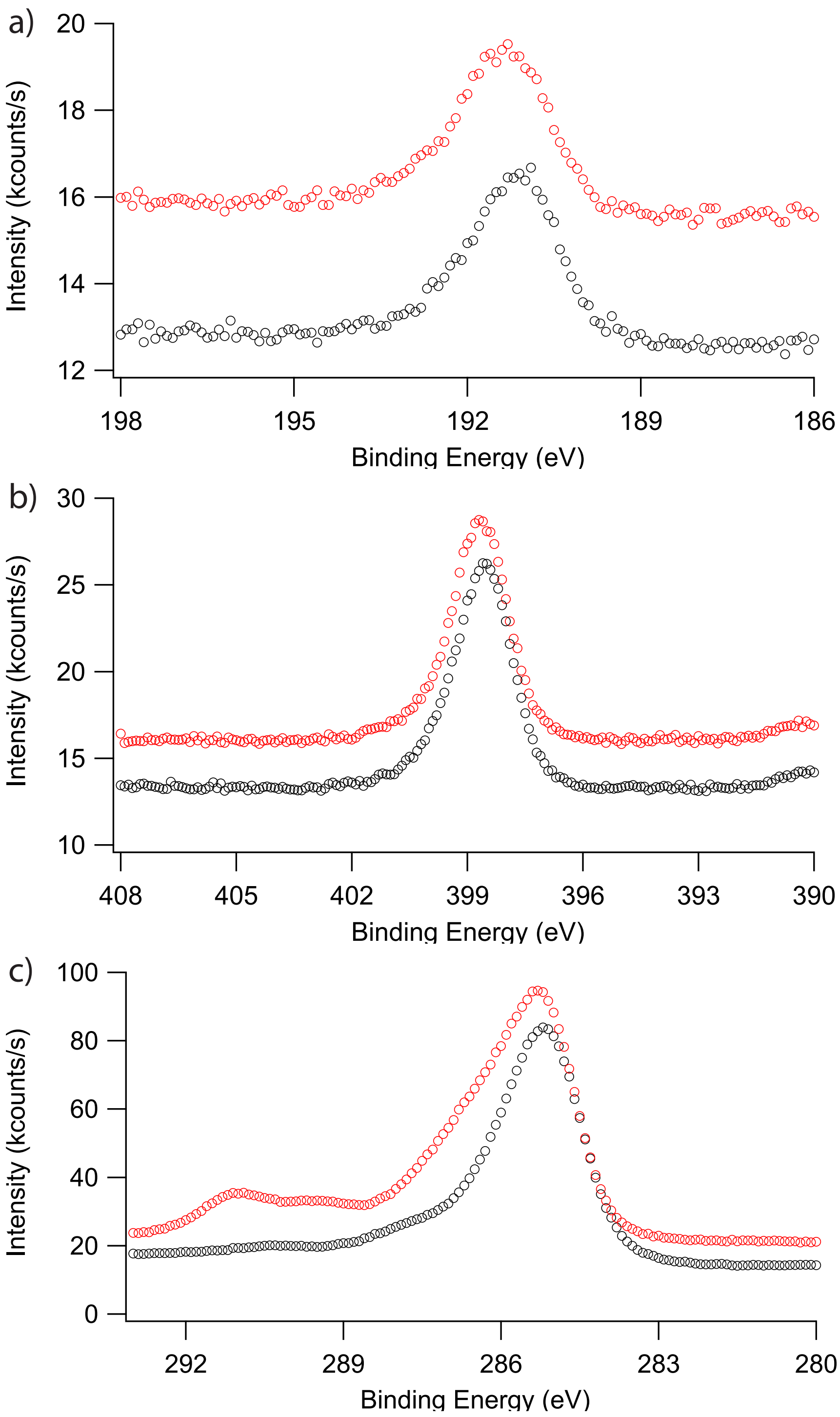

Figure 3.11 XPS spectra of g/h-BN/SiO$_2$ in with $\varphi = 0°$ relative rotation in red and $\varphi = 40°$ relative rotation shown in black. In a) spectrum for B1s, in b) spectrum for N1s and in c) spectrum for C1s.

called Dirac cone, is visible, which is a fingerprint for graphene. The Dirac cones are also visible in the momentum distribution maps in b) and c), where the six-fold symmetric intensity hills refer to the $\overline{\Gamma K}$ and $\overline{\Gamma K'}$ directions. When comparing the momentum distribution plots, the different relative graphene rotations of the samples become visible, as the Dirac cones are rotated by $\varphi = 40°$ in respect to each other. The relative rotation is highlighted by the orange arrows.

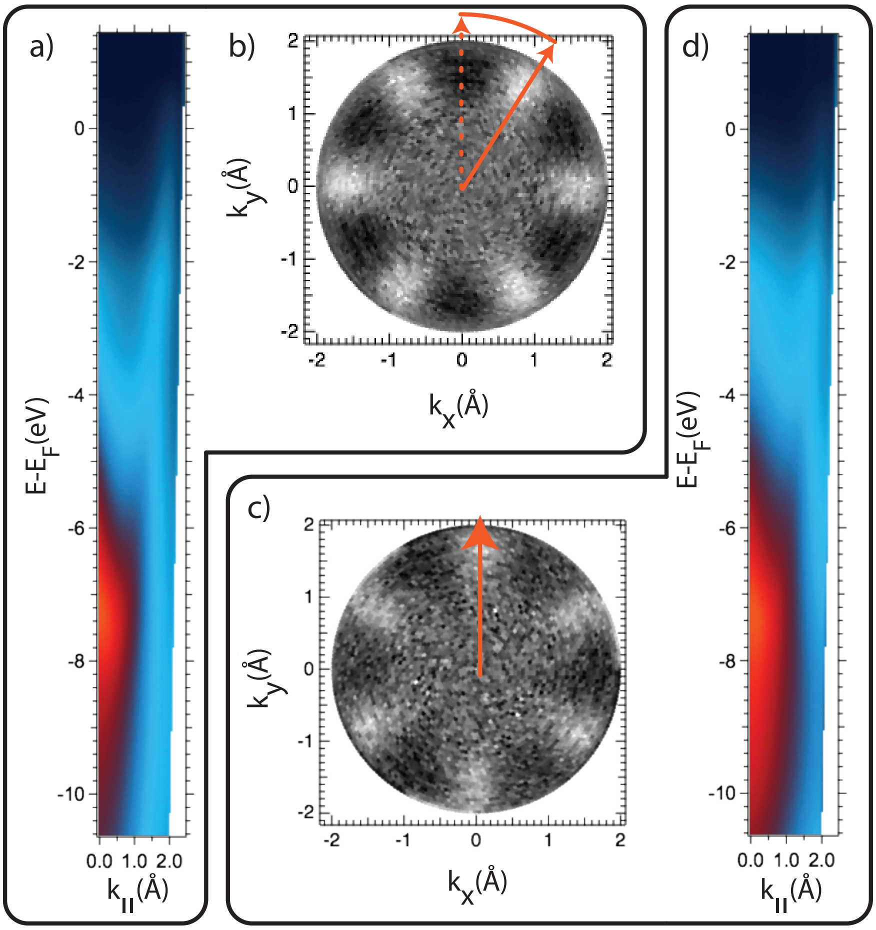

Figure 3.12 In a) and d) intensity plots in the $\overline{\Gamma K}$ direction of the $\varphi = 40°$ and $\varphi = 0°$ relative rotated sample respectively. In b) and c) the momentum distribution maps of the $\varphi = 40°$ and $\varphi = 0°$ relative rotated sample respectively.

The samples were measured by resistivity and Hall measurements. From these data the mobility was determined and compared in figure 3.13 to regularly transferred graphene originating form polycrystalline copper foils and to transferred graphene originating form iridium sinergia films grown as described in chapter 2. The figure shows the charge carrier mobility in respect to the resistivity of the samples in a logarithmic plot. The data clearly show the decrease in mobility and an increase in resistivity between different groups of samples. The transport properties of graphene originating from polycrystalline copper (black triangles) display the best electronic transport properties (highest mobility and low resistivity). These samples were not treated with the TOA-Br pretreatment for the graphene transfer. The single layer graphene originating from single crystalline iridium, on the other hand, show a degradation of the electronic transport properties by a factor of 10, while the heterostructured samples display a degradation by a factor of 100. This trend suggests a negative impact of the transfer method on the measured samples also observed by Salmi et al. [98]. On the other hand, using equation 3.40, the charge carrier densities can be seen as lines on the mobility-resistance plot. These dashed lines are called isodensity lines and show that the heterostructured samples possess the lowest charge carrier density. The low charge carrier densities may arise from the h-BN substrate for graphene in the heterostructure, which quenches the influence of the SiO_2 substrate.

3.8 Conclusions

In this chapter, the electronic properties of graphene were resumed, and a known method to measure electronic transport in thin materials through resistivity and Hall coefficient measurements was presented. These properties are well known for mechanically exfoliated graphene sheets of microscopic size. The possibility to grow and transfer graphene sheets from inexpensive, single crystalline substrates can be used to probe large centimeter sized graphene sheets on SiO_2 [94]. To probe the electronic properties of the graphene grown on the Sinergia Ir(111)/YSZ/Si(111) in combination with the h-BN

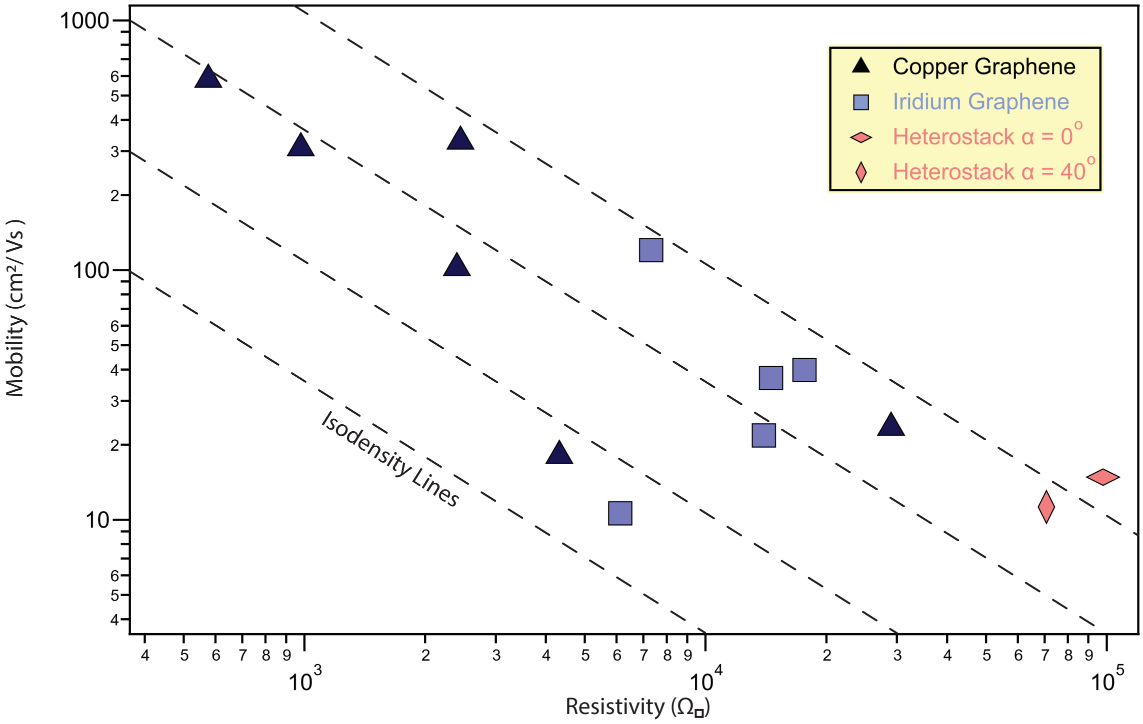

Figure 3.13 Electronic transport properties of transferred g/SiO_2 and g/h-BN/SiO_2 samples. Plot of the charge carrier mobility in respect to the sheet resistivity on a log-log scale. The black triangles represent graphene transferred from polycrystalline copper, which were not treated with TOA-Br in the delamination step. The blue squares represent graphene transferred from iridium samples and the red rhombi represent the g/h-BN/SiO_2 samples. The dashed lines represent the lines with equal charge carrier density, which are called isodensity lines.

grown on Rh(111)/YSZ/Si(111) a home-built 4-point probe measurement setup was constructed. This setup is capable of probing the voltage drop generated by an applied current over four pins. An external homogeneous magnetic field allows to probe the Hall coefficient and thus compute the charge carrier density and mobility. The grown graphene sheets were transferred onto insulating materials using the TOA-assisted electrochemical delamination method, which allows the transfer on SiO_2 substrates. The transfer process must be performed individually for each sheet of material, but can be performed in sequence to construct heterostacks of arbitrary h-BN - graphene combinations. The combination of two g/h-BN/SiO_2 samples was shown in section 3.7.2, where the graphene sheet was rotated by a chosen angle of $\varphi = 40°$ between the graphene and h-BN orientation. This rotation was visible with optical microscopy (figure 3.10) and in the momentum distribution map (figure 3.12), where a rotation of the Dirac cones between the samples can be observed. The transport results can be compared to single standing graphene transferred from iridium on SiO_2 and to single standing graphene transferred from polycrystalline copper on SiO_2 (figure 3.13). A tendency towards lower performing transfer properties can be observed for samples which received the TOA-Br pretreatment for electrochemical delamination. The figure 3.13 shows a decrease in transport properties of roughly a factor 10 for each TOA-assisted layer transfer on the sample, which suggests a strong interaction of the transfer method with the electronic properties of the samples. Nevertheless, the heterostructured samples show the lowest charge carrier density respect to the samples transferred directly on graphene, which may be due to the decoupling from the SiO_2 substrate by the h-BN. The negative effect of the TOA transfer may be avoided partially by a direct growth approach of g/h-BN/Rh(111) structures in situ, where one of the two transfer steps can be avoided. The results of this approach are shown in chapter 4. On the other hand, the separate exfoliation method remains an appealing target for the construction of arbitrary graphene

- *h*-BN heterostructures. An extensive study and optimisation of the electrochemical transfer method would be needed, to reach literature comparable mobility values for the transferred layers.

4 In situ prepared graphene - hexagonal boron nitride heterostructures

4.1 Introduction

In this chapter, the direct in situ growth of graphene on hexagonal boron nitride - g/h-BN/Rh(111) heterostructures will be discussed. While the attempt to mechanically assemble heterostructures was presented in chapter 3, the quality of the structure was not satisfying for device application as seen in section 3.7. In order to improve the quality of the produced structures, the approach of the direct growth in situ was investigated. This direct method eliminates the two separate intermediate electrochemical delamination steps, so reducing potential defects and the negative effect which tetraoctylammonium-Bromide (TOA-Br) treatment has on the sp_2 layers [98]. Nevertheless, one single step of delamination will still be necessary to obtain the heterostructure on an insulating chip instead of two separate steps. Additionally, the transfer on a silicon oxide substrate opens the possibility for optical measurement methods, which can help to understanding the growth mechanism of heterostructures.

The growth of g/h-BN/Rh(111) structures was already attempted by Roth et. al. on rhodium Rh(111) [33] and on copper Cu(111) [24] single crystals. The growth of these heterostructures on single crystals suggested the feasibility of this project on rhodium sinergia films Rh(111)/YSZ/Si(111) [30], which are considered of equal quality and crystallinity, but lower in price by an order of magnitude and in high availability.

The preparation was performed by a first step of CVD using borazine $(HBNH)_3$ on the rhodium sinergia films to grow the h-BN layer, as discussed in chapter 2. A subsequent millibar pressure exposure to carbon rich precursor molecules (3-pentanone $C_5H_{10}O$ and ethylene C_2H_4) was carried out to grow the graphene layer on the passivated h-BN/Rh(111) surface.

The grown samples were preliminary quality checked in the ESCA laboratory using XPS, XPD, UPS and ARPES. To obtain steadfast experimental data the samples were also measured in the PEARL laboratory at the Paul Scherrer Institute, where a higher energy resolution for the XPS data can be achieved and the possibility to record energy resolved XPD patterns is present. After the transfer of the heterostructures to an insulating SiO_2 substrate the heterostructure can be directly observed with optical microscopy and Raman spectroscopy, opening a new way of interpretation of the h-BN graphene heterostructure aggregation.

The obtained results will be presented in form of a paper draft to be submitted for peer review.

4.2 Paper Draft: Growth and characterisation of carbon - h-BN millimeter sized heterostructures on Rh(111) wafers and SiO_2 chips

Authors:

C.Bernard, R.Stania, E.Miniussi, W.Zabka, M.Haluska, M.Muntwiler, J.Osterwalder and T.Greber

4.2.1 Abstract

The High charge carrier mobility in graphene is a highly researched topic since exfoliation and characterisation of single graphene layers [5], [6]. The lack of integration of graphene in electronics is mainly due to the difficult task of the decoupling from the substrate, especially for the industrially practicable growth method, as chemical vapour deposition (CVD) is [99]. On the other hand, *h*-BN was found to be the ideal substrate companion for graphene, for its similar structure and high band gap insulating character [9]. The integration of both materials in a vertical or horizontal stack is called a heterostructure.

Here we show the attempt to grow a heterostructure in a single step by CVD on low cost large scale Rh(111)/YSZ/Si(111) wafer, which enables an important step towards application oriented material engineering.

The grown structure was analysed by scanning tunnelling microscopy (STM) and x-ray photoelectron spectroscopy and diffraction (XPS, XPD). Moreover, the inexpensive availability of wafer samples, respect to the single crystal counterpart, opens the possibility for liquid phase electrochemical delamination of the 2D materials [32], [94]. This

allows for integration on well known insulating substrates, such as silicon oxide, and additional characterisation methods as optical microscopy and Raman spectroscopy.

4.2.2 Experimental

4.2.2.1 Growth Conditions

The heterostructure was grown using a 4-inch wafer consisting of a $Si(111)$ base wafer with a 10 nm thick yttria stabilized zirconium (YSZ) buffer layer on which a 200 nm thick film of rhodium with a Rh(111) crystalline structure was deposited [31], [30]. The 200 nm thick rhodium film can be thus considered as bulk material. The wafer was subsequently treated by three cycles of argon ion sputtering (E_{kin} = 1 keV), annealing and hot oxygen dosing (P= $1 \cdot 10^{-7}$ mbar at T= 1075 K) and high temperature flashing (T= 1175 K). The *h*-BN layer was grown by chemical vapor deposition (CVD) at a temperature of T= 1125 K using borazine $(HBNH)_3$ [39] as a precursor molecule with a dose of D= 170 L [16].

The carbon was deposited by a millibar pressure CVD growth step at $T = 1125\ K$ sample temperature on the *h*-BN/Rh(111)/YSZ/Si(111) wafer, as shown by Roth et. al [24] [33]. The pressure was increased by a leak valve admitting ethene (C_2H_6) to the chamber up to a growth pressure of p=$1 - 1.5$ mbar for 5 minutes at a sample temperature of T=1175 K. This cycle was repeated after an intermediate cooling step. The total dose admitted for the carbon species growth was D=0.5 GL of ethene. The same procedure was also repeated with 3-pentanone $C_5H_{10}O$ [41] finding no differences in the result of the two precursor molecules [13].

The samples were measured as grown by STM, XPS and XPD. Subsequently the samples were transferred on SiO_2 chips (oxide thickness of 90 nm), with gold quatrefoil cloverleaf shaped contacts, by tetraoctylammonium bromide assisted electrochemical delamination [32], [94]. The transferred layers were analysed by optical microscopy and Raman spectroscopy and the XPS, XPD measurements were repeated to ensure the transfer quality.

4.2.2.2 Sample Characterisation

Optical images were obtained using a Leica DMV2500 stereo-microscope with a 1-inch CCD camera [100]. Raman measurements were acquired with a Witec confocal Raman microscope with a 532 nm laser wavelength and a diffraction-limited lateral resolution of 340 nm. X-ray photoelectron spectroscopy (XPS) and x-ray photoelectron diffraction (XPD) were acquired at the PEARL laboratory stationed at the Swiss Light Source (SLS) of the Paul Scherrer Institute (PSI) using a bending magnet source with a 1200 lines per mm planar grating for the energy range of $60 - 2000$ eV [101]. The data was taken with a photon energy of $E_{kin} = 800$ eV. The electron spectrometer was a Scienta EW4000 hemispherical electron analyser with two dimensional detection. Preliminary data was taken at the ESCA laboratory of the University of Zurich, using a MgK_α x-ray source and a modified VG-Scienta electron spectrometer [35]. STM data was taken with an Omicron LT-STM at a temperature of T=4 K in constant current mode with a direct transfer system to the PEARL laboratory vacuum system.

We investigated the transferred and untransferred samples by STM, XPD and XPS while Raman and optical microscopy were only performed on the transferred samples.

4.2.3 Results

The results will be presented in a non chronological fashion, beginning with the optical and Raman results, to allow for a more straightforward explanation of the proposed arrangement of the heterostructure. Subsequently the photoelectron spectroscopic and scanning tunnelling results are presented. We will refer to the untransferred samples as to the *pristine* samples and to the delaminated samples as to *transferred* for clarity.

4.2.3.1 Optical Microscopy

The transferred g/h-BN/Rh(111) was analysed by optical microscopy, as the optical contrast between the SiO_2 substrate and the h-BN and graphene depends on the oxide thickness and wavelength of the light [102], [103], [69]. The chosen oxide thickness of 90 nm for the substrates allows identifying layers of graphene and h-BN species. The optical images are shown in figure 4.1, illustrating a transferred g/h-BN/Rh(111) sample with increasing magnifications.

In subfigure a) the entire sample is shown, the dark cloverleaf structures (A) are gold contacts, with a $\simeq 3nm$ chromium layer underneath, on the substrate, used for electronic transport measurements. The size of the transferred layer is in the order of 6×8 mm^2. At (B) the bare substrate, with the onset of the transferred layer (C) is visible. The image shows numerous concentric darker regions (D) with a similar size of L$\simeq$ 200 μm. The darker contrast with respect to the remaining structure can be associated with increased carbon deposition, starting from growth centers on the sample. The reflective grain (E) in subfigure 4.1 b) may be associated with a metallic residue transferred from the delamination process.

The dark concentric regions (D) are visible in the magnification shown in subfigure 4.1 c) and d) where an additional inner structure becomes visible (H), in the form of darker grains with a size up to $L_{grain} = 4.2$ μm. The grains increase in size towards the border of the concentric structures. In (F) the merging of two concentric growth sites is visible, suggesting a radial growth of the structures during the millibar exposure.

Figure 4.1 d) allows additionally to differentiate between the dark grain structure (I) and darker flat regions (J). The composition of the three structures, the dark concentric regions, the flat dark regions, and the grain structure can not be deduced from optical imaging alone. As the g/h-BN/Rh(111) structure is on a silicon oxide substrate further Raman spectroscopy measurements were performed on these regions of interest.

Having gold sputtered cloverleaf contacts the option to measure the electronic transport was attempted in a self built 4-point probe. The optical images show how the graphene layer is not shaped in a closed patch over the four contacts and the obtained resistivity was therefore measured as higher than $R > 20$ GΩ, compared to the $R_s \simeq 3$ kΩ measured in [94]. This supports the claim of zones between the concentric dark regions (D) to be covered with insulating material such as h-BN.

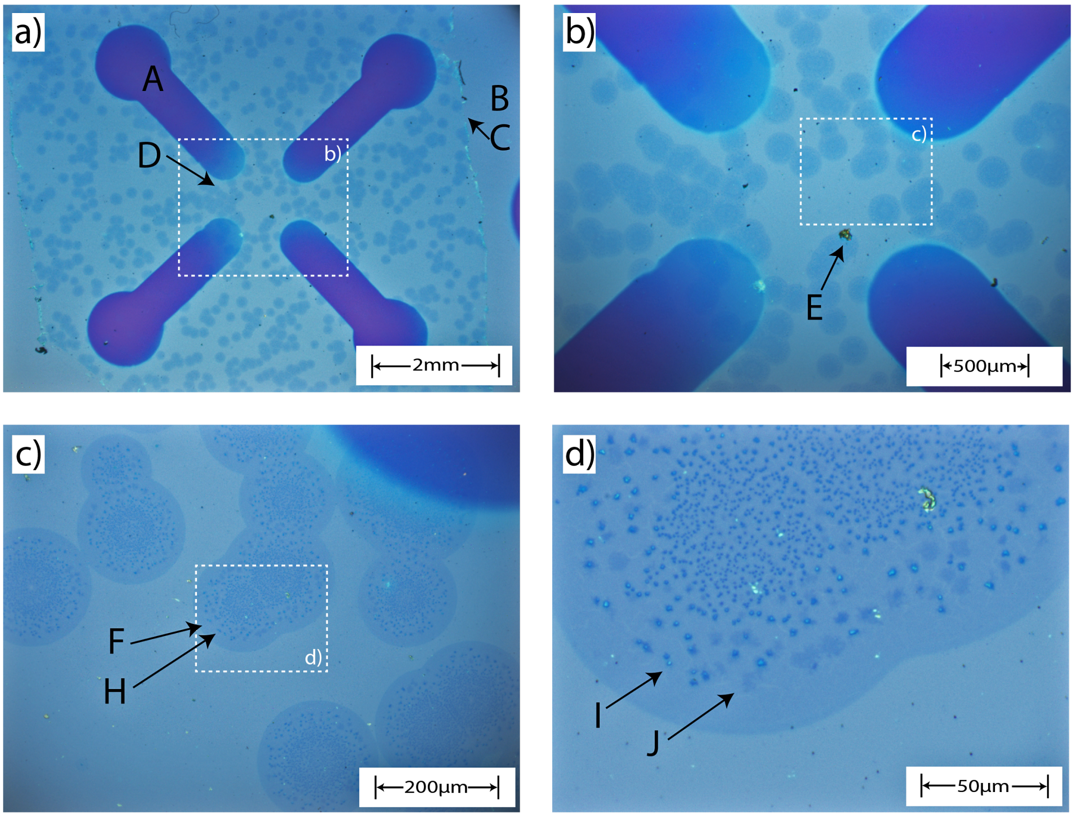

Figure 4.1 Optical microscopy images of a g/h-BN/Rh(111) sample. In subfigure a) an overview of the complete 10 x 10 mm sample: (A) contacts for further transport measurements; (B) bare SiO_2 substrate; (C) edge of the transferred layer, this border is consistent with the onset of the contiguous h-BN layer; (D) carbon growth centers with a higher light absorption suggesting the addition of one to multiple layers. Subfigure b) magnification of the highlighted area in a): (E) metallic grain from the electrochemical transfer. Subfigure c) magnification of the highlighted area in b): (F) circular carbon growth center merged with its neighbours; (H) dark multilayer carbon grain structures. Subfigure d) magnification of the highlighted area in c): (I) sharp grain structure, consistent with a multilayer type of carbon growth; (J) homogeneous carbon structure, consistent with layer by layer growth.

4.2.3.2 Raman Spectroscopy

To identify the composition of the indicated structures Raman measurements of the transferred samples were taken. Graphene results in characteristic inelastic modes called D, G and 2D modes, where the D mode is associated with defects, the G mode with carbon sp^2 allotropes and the 2D mode with defectless graphene layers [104], [105], [106]. Shifts and multipeak structures of the 2D modes can be attributed to graphitic stacking of graphene [107] and multipeak structures in the G mode may suggest the presence of graphene oxide or functionalisation of graphene [108].

The measurements were performed on a concentric dark region identified in figure 4.1 with the marker (D) and visible on the optical image of the Raman microscope in figure 4.2 a). Raman maps were performed in the region highlighted by a blue square integrating the intensity of the 2D and G modes. The Raman maps are shown in subfigures 4.2 b) and c), where the two dark grains can be recognised, displaying two strong features in the 2D mode, corresponding to the regions (1) and (4) in the optical image. The G mode is also enhanced in these regions, as visible in figure 4.2 c).

To further analyse the Raman footprint on these regions, single spectras were taken at the locations marked with numbers (1, 2 and 3) in subfigure 4.2 a). These regions correspond to: the dark grain feature (1); the plateau area next to the grain (2); a darker flake like structure (3). The overview spectras of the regions are plotted in subfigure 4.2 d). The spectras display the Raman modes expected from graphene, with the presence of the D mode which indicates the presence of defects in all three structures, but especially in the region (2). Additionally, two respectively small peak appears at $E_{CH} = 2950\ cm^{-1}$ and $E_{NT} = 2450\ cm^{-1}$ the first may be associated with hydrocarbon bounds on the sample surface, while the origin of the second is usually found on HOPG and carbon nanotubes but its origin is still debated [109].

In subfigure 4.2 e) a zoom in of the 2D mode region of the spectrum is shown. The spectras of the 2D mode show the presence of at least a double peak for the regions (1) and (3) with energies of $E_{2D_2} = 2665\ cm^{-1}$ and $E_{2D_1} = 2702\ cm^{-1}$. This modulation of the 2D mode indicates the presence of a multilayer graphite (AB-Bernal stacked graphene) structure, as expected from the high optical contrast of these structures [107].

Compared to the regions (1) and (3) the 2D mode in the region (2) is suppressed and shows a single peak structure. This suggests the presence of a single layer defective graphene sheet.

To further investigate the defect structure of the layer, a zoom in of the G mode is presented in subfigure 4.2 f). The G mode for all three regions display a double peak feature at energies $E_{G_1} = 1585\ cm^{-1}$ and $E_{G_2} = 1623\ cm^{-1}$. The second G peak has a blueshift of about $\Delta E_{G_1 G_2} = 38\ cm^{-1}$ respect to the first, shown by the dashed lines in the spectrum. This indicates the presence of either oxide or functionalisation of the graphene layer [108]. The latter may be explained by the presence of residues due to the transfer process of the heterostructures. The presence of *h*-BN is unfortunately not visible with this raman setup, as the E_{2G} mode *h*-BN is located in the energy range of the graphene D mode, of which the latter is dominant [110]. The excitation wavelength and the SiO_2 thickness are not favourable for a direct observation of the *h*-BN layer.

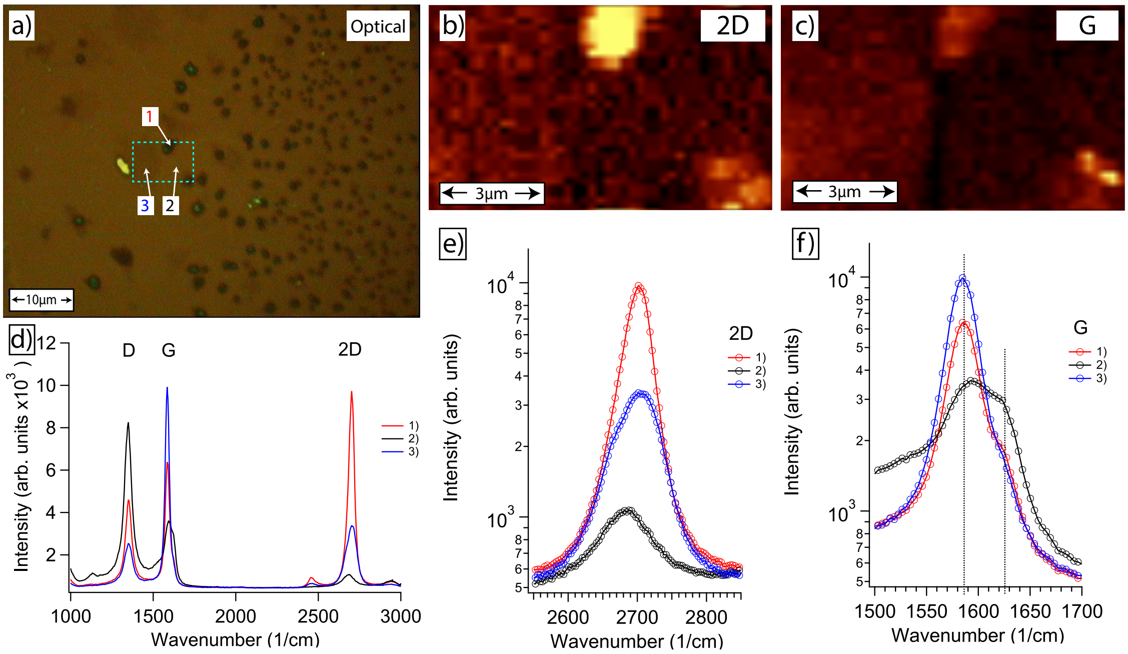

Figure 4.2 Raman measurements taken at the center for Micro- and Nanosystems DMAVT of the ETH-Zurich with a laser wavelength of $\lambda_0 = 532\ nm$. Subfigure a) optical image of the measured area, located on a carbon growth center (D) shown in figure 4.1. The blue box indicates the area of the Raman intensity maps shown in subfigures b) and c), representing the intensity of the 2D and G modes respectively. In subfigure d) the overview Raman spectra taken at the locations 1, 2 and 3 in subfigure a) respectively, are shown. The spectrum 1) was taken on a grain of carbon accumulation, 2) on a plateau of carbon deposition and 3) on a darker structure, which may be due to an additional carbon layer. The spectra show the presence the characteristic 2D and G peak indicating the presence of a hexagonal carbon structure. The visible D mode indicates the presence of defects in the structure, which is especially high in region 2. In subfigure e) the 2D mode is shown in detail. The 2D mode indicates the presence of at least two components located at an energy of $E_{2D_2} = 2665\ cm^{-1}$ and $E_{2D_1} = 2702\ cm^{-1}$. The presence of multiple components can be explained by the presence of graphite structures. In subfigure f) the G mode is shown in detail. The G mode shows the presence of a double component with energies of $E_{G_1} = 1585\ cm^{-1}$ and $E_{G_2} = 1623\ cm^{-1}$. The double component of the G mode may indicate the presence of oxidation or functionalisation of the graphene layers.

4.2.3.3 Scanning Tunnelling Microscopy

Scanning Tunnelling Microscopy (STM) measurements were performed prior to electrochemical delamination on the g/h-BN/Rh(111) samples. The measurements were performed at T= 4 K liquid helium temperature. Before measurements, the samples were degassed to a temperature T= 1075 K, in order to eliminate volatile atmospheric carbon residues due to the ex-situ transport to the PEARL laboratory. The results are shown in figure 4.3. The figures were treated with Gwyddion SPM data analysis software [111] where the images were flattened by subtracting an inclined plane.

In subfigure 4.3 a) a large scale image (130 × 130) nm^2 is shown. Visible are areas with graphene and areas with h-BN, including terraces with atomic steps. The h-BN covered areas appear in a honeycomb pore-wire shape with no azimuthal disorder [112], [113], where the darker round hole like features are called pores and the hexagonal lighter structure are called wires. The graphene areas instead appear as triangular hills and dark valleys [114]. The graphene layers show an azimuthal disorder, which can be attributed to the high pressure growth conditions which do not favor a perfect epitaxial growth [13].

To further analyse the region a zoom in of the green highlighted area is shown in subfigure 4.3 b) with (60×60) nm^2 size. The zone (A) shows a plateau covered with ordered h-BN. Area (B) instead is covered with graphene. In the zone (C) the junction of a graphene covered area next to h-BN is visible, suggesting a horizontal arrangement of the two materials rather than vertical. The scanned region may thus be a similar area which was measured with Raman spectroscopy in figure 4.2 a) area (2).

Analysing the junction allows for an attribution of stacking sequence for the two materials: either horizontal or vertical. As to height calibration the two atomic terraces for a rhodium (111) oriented crystal was used, as it is well known from literature [115] and is d= 0.219 nm per step. The measured z-height of the STM figure was normalised to the atomic step height shown in the cut (1) plotted in 4.3 d). Subsequently a cut through the junction area (2) is shown in 4.3 d). The y-axis of the plot is the height while the x-axis is the position on the cut line. The left part of the plot shows the periodicity of the graphene part, while on the right side the periodicity of the *h*-BN is shown. The junction area in the blue box is smooth without height jumps which suggest graphene and *h*-BN to be arranged horizontally, as in a vertical arrangement a jump in height would be expected. Moreover, the smooth crossover from the *h*-BN to graphene zone hints to an atom by atom substitution of the boron and nitrogen atoms of the *h*-BN with the carbon atoms of the graphene. The cut also allows to state the periodicity of the grown graphene $\Delta L_g = 3.21$ nm and *h*-BN $\Delta L_{h-BN} = 3.28$ nm which is compatible with literature values [16], [114].

In order to assert more precisely the growth mechanism of graphene substituting the *h*-BN, a second magnification of the area highlighted by the orange box in subfigure 4.3 b) and shown in 4.3 c) with the size of (20×10) nm^2 was performed. The area is centered on the graphene *h*-BN junction. The marker (D) indicates the growth sites of the graphene nucleation front and appear to happen in the pore site of the *h*-BN nanomesh structure. The marker (E) indicates the defects in the *h*-BN layer, which may be generated under the unfavourable millibar pressure conditions of the graphene growth. From the image, it becomes apparent, that the *h*-BN, where marker (D) indicates to, is substituted directly by the valley region of the graphene. Equally the wire regions of the *h*-BN are substituted by hill regions of the graphene. This is a direct observation for the graphene moiré overlayer with the *h*-BN structure as measured by Wang et. al. for graphene [116], and Laskowsky et. al. for *h*-BN [117], Brugger et. al. [114] and observed by Sutter et. al. [26].

The substitution sequence is highlighted in the lower part of subfigure 4.3 c) with cartoon shapes blended in the identical image from above to highlight the special topographic areas. In the graphene case, the valley regions are shown with green circles, the intermediate region with orange triangles and the hills with red triangles. In the *h*-BN case the pore regions are highlighted by blue hexagons while the wire sites are marked with orange and red alternating trifeuille cloverleafs. The image clearly shows a substitution of the pores (blue hexagons) by the valleys (green circles). The wires sites (cloverleafs) are substituted by the hills (red and orange triangles). The regularity of the junction can be strikingly appreciated by the smooth fadeout of the cartoon objects in the central region.

The transition mechanism is explained by the model in subfigure 4.3 e) where the three atomic junctions are diagrammed with the respective atomic locations on the rhodium substrate lattice. The arrangement of the boron, nitrogen and carbon atoms is described by the occupied position respect to the substrate atoms, three positions are possible namely the top, hcp and fcc positions. In *h*-BN the position of the nitrogen is decisive for the formation of a hill or pore depression of the corrugated material [118]. In the fist model the pore sites of the *h*-BN are located in areas where the nitrogen atoms happen to be placed on top of the rhodium atoms, while the boron atoms occupy the fcc spot of the lattice, also called the octahedral site of an fcc(111) lattice. The second layer of rhodium atoms is visible across the tetrahedral sites (hcp sites), which are not occupied in this configuration. In the case of the graphene, assuming the atoms occupy the same positions as the *h*-BN in the vicinity, the area must be assigned to a valley area, as it is observable in figure 4.3 c) where the pore sites (blue hexagons) transition in valley sites (green circles).

The same consideration can be made for the second diagram, namely the *h*-BN with nitrogen atoms on the tetrahedral site and the boron on the top position. The tetrahedral sites correspond to the hcp sites in a fcc crystal. This configuration corresponds to a wire site in the *h*-BN and becomes a intermediate (or slightly higher valley) site for the graphene. Equally, this situation is observable in figure 4.3 c) where the wire sites (orange cloverleafs) transition to intermediate states (orange triangles).

In the last configuration, the *h*-BN atoms can occupy the tetrahedral (hcp) and octahedral (fcc) sites. This configuration corresponds to a wire site. The corresponding graphene configuration is a hill site, which is observable in figure 4.3 c) as wire sites (red cloverleafs) transitioning to hill sites (red triangles).

The final observation which can be made through these considerations is that an atom by atom substitution process happens when *h*-BN/Rh(111) is provided with a carbon precursor in high pressures (millibar) and temperature, resulting in a substitution of the *h*-BN by graphene. A horizontal stacking sequence is found in the shown data which can be seen as nano-templates switching form conductive graphene to insulating *h*-BN [119], while vertical stacking was not found. The image equally suggests that *h*-BN can be completely substituted with long high pressure and high temperature carbon exposure.

4.2.3.4 Photoemission of the pristine sample

The pristine samples were analysed by x-ray photoemission spectroscopy and diffraction with a photon energy of $h\nu = 800$ eV. The obtained spectra are shown in figure 4.4, where the carbon and the nitrogen measurements are shown. The energy was recalibrated on the fermi edge and the rhodium $3d_{5/2}$ elastic line (not shown). The presence of a carbon and nitrogen elastic line confirm the presence of both elements on the sample.

In subfigure 4.4 a) the spectrum of the C1s elastic line is shown. The line shows three contributions which can be fitted using three Doniach Sunjic line shapes [120]. The raw data is shown by red circles, the fitting result by a blue line and the individual

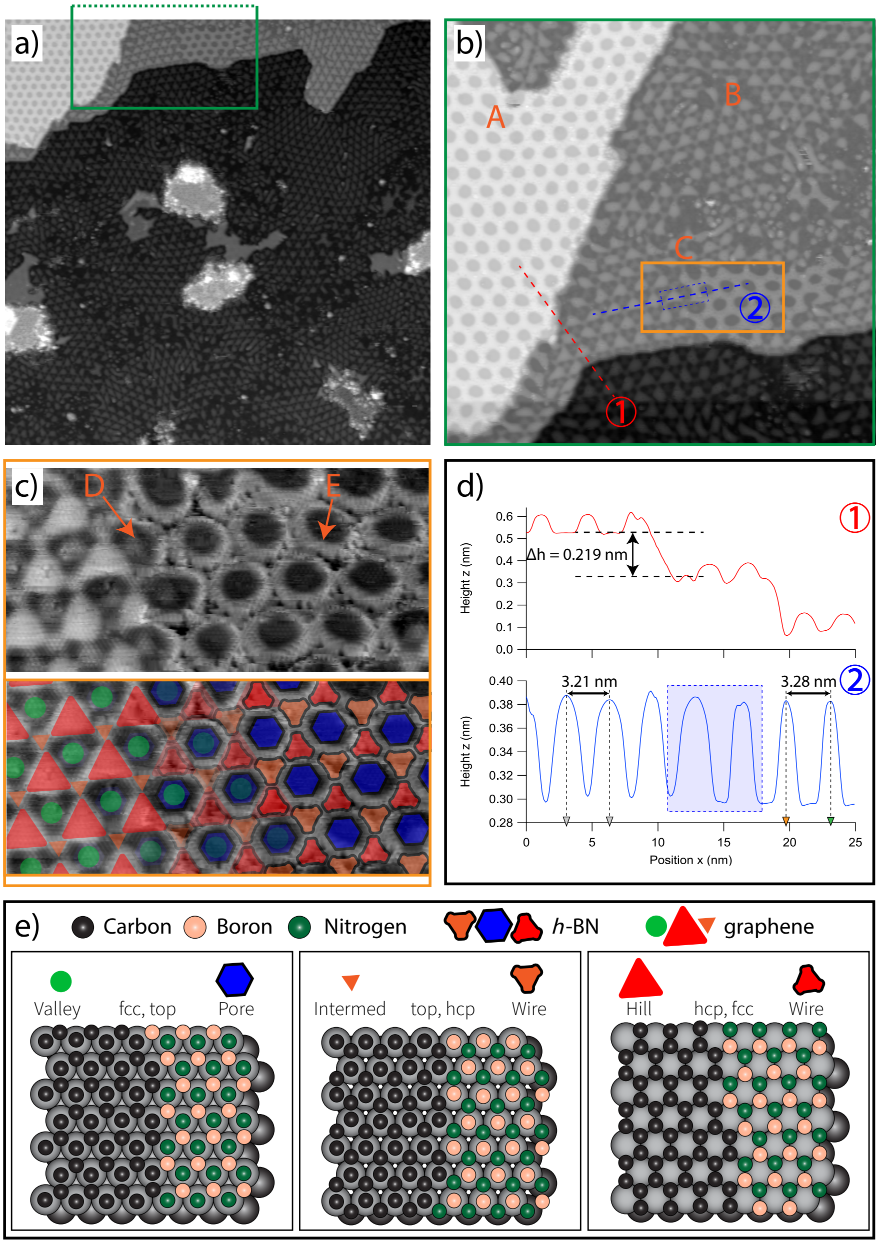

Figure 4.3 STM images of a pristine g/h-BN/Rh(111) sample prior electrochemical delamination. Subfigure a): Overview scan (130 x 130) nm^2 in size, $I_T = 100$ pA, $V_B = -1$ V. Subfigure b), magnification of the green inset in subfigure a), size (60 x 60) nm^2, $I_T = 100$ pA, $V_B = -1$ V. Marker (A), terrace with ordered *h*-BN. Marker (B), terrace with disordered graphene and *h*-BN. Marker (C), an island of *h*-BN surrounded by graphene. Subfigure c) top image: magnification (20×10) nm^2, $I_T = 100$ pA, $V_B = -0.3$ V, of the orange marked region of subfigure b). Marker (D), growth front of graphene which substitutes the *h*-BN. Marker (E), defect sites in the *h*-BN structure, mainly found on wire sites. Bottom image: Visualisation of wire and pore zones of the *h*-BN through blue hexagons (pores) and cloverleafs (wires); visualisation of the hill and valley zones of the graphene through red and orange triangles (hill) and green circles (valley). Subfigure d), cuts through subfigure b), in red over two terrace steps, on which the figure was height calibrated, in blue perpendicular to the junction zone. In e) visualisation of the junction arrangement for the three atom positions respect to the substrate in the respective junction configurations. The images represent one arrangement status over the whole image, not showing the moiré structure of graphene and *h*-BN.

fitting peaks by black lines. The best fit was obtained by two asymmetric shapes called C_2 and C_3 and one symmetric shape called C_1. Three distinct energies were obtained for the three C1s lines: $E_{C_1} = (284.97 \pm 0.01)$ eV, $E_{C_2} = (284.45 \pm 0.02)$ eV and $E_{C_3} = (283.76 \pm 0.03)$ eV. The distinct energies of the C 1s line may be due to various reasons: different carbon allotropes with a distinct hybridisation (sp^2 and sp^3) [121] [122], different chemical environnement as the presence of oxidised carbon or defects in the lattice [123] or carbon embedded in the first rhodium layers as a carbide. The formation of a rhodium carbide was already observed by Roth et al. [33] where a layer of intercalated carbon atoms decouple the *h*-BN from the substrate. As a result the *h*-BN nanomesh becomes flat and enables the contiguous growth of the graphene layer in a second CVD step. The difference with the findings of Roth et al. is the splitting of N 1s signal in wire and pore binding energies shown in figure 4.4 e), which in contrary suggest the *h*-BN to be still in a nanomesh state [124].

In order to clarify the origin of the carbon triple peak structure x-ray photoemission diffraction (XPD) was used, to link the chemical species to its structure. The XPD measurements are shown in subfigure 4.4 b) where the XPD of the complete C1s peak is shown in figure 4.4 b). The peak shows a characteristic 6-fold structure for a multilayer graphene with Bernal stacking sequence [81]. To confirm the XPD pattern for multilayer Bernal stacked graphene the pattern was simulated using electron diffraction in atomic clusters (EDAC) code [58] for a bilayer graphene with AB stacking. The resulting pattern is shown in subfigure 4.4 c) and reproduces the measured XPD to a high degree of accuracy.

The measured XPD patterns are recorded with an analyser pass energy and a two-dimensional channelplate is used as electron detector. The recorded C 1s and N 1s XPD's thus are energy resolved over the 150 channelplate channels and the structure of the three carbon species can be deconvoluted. The measured XPD can, therefore, be energy deconvolved using the fitted curves C_1, C_2, C_3 [125], [126]. The fitting must be performed over each position of the measured hemisphere. Performing this deconvolution results in three patterns for the three peaks shown in subfigure 4.4 d), these patterns indicate the structure arising from each peak which was deconvoluted. The figures show the clear graphitic pattern of the C_1 peak. The bernal AB stacked structure thus corresponds to the C_1 species. The peaks C_2 and C_3 have a weak recognisable structures which resemble the C_1 peak, especially at low polar angles, but the low signal to noise ratio hinders the attribution of a precise pattern. The weak structure may be due to the near energy position between the C_2 and C_3 peaks respect to the C_1 peak, resulting in crosstalk. The contributions of the C_2 and C_3 species are thus to be attributed to disordered graphene and “amorphous “carbon respectively on the sample, where the ordered C_1 XPD signal can be attributed to ordered graphene and few layer graphene visible on the Raman and STM measurement

To prove the presence of graphite in coexistence with h-BN an XPS spectrum and XPD pattern of the N1s line was taken. The XPS spectrum is visible in the subfigure 4.4 d) where the red circles represent the measured data, the blue line the fitting result and the black lines the single fitting peaks. The peak has to be fitted with two gaussian lines as the pore and the wire site of the corrugated h-BN nanomesh exhibit two different binding energies of the N1s line [127], [124]. The binding energy for the pore site $E_P = 398.62 \pm 0.01$ eV marked with (P) is higher as the wire site marked with (W) $E_W = 398.16 \pm 0.01$ eV, which is comparable with the core level splitting found by Preobrajenski et al. [124].

The XPD pattern of the N1s line is shown in subfigure 4.4 f) and displays the characteristic 3-fold structure of the h-BN patterns as shown on Ni(111) by Auwärter et. al. [118], demonstrating the coexistence of crystalline h-BN with multilayer graphene.

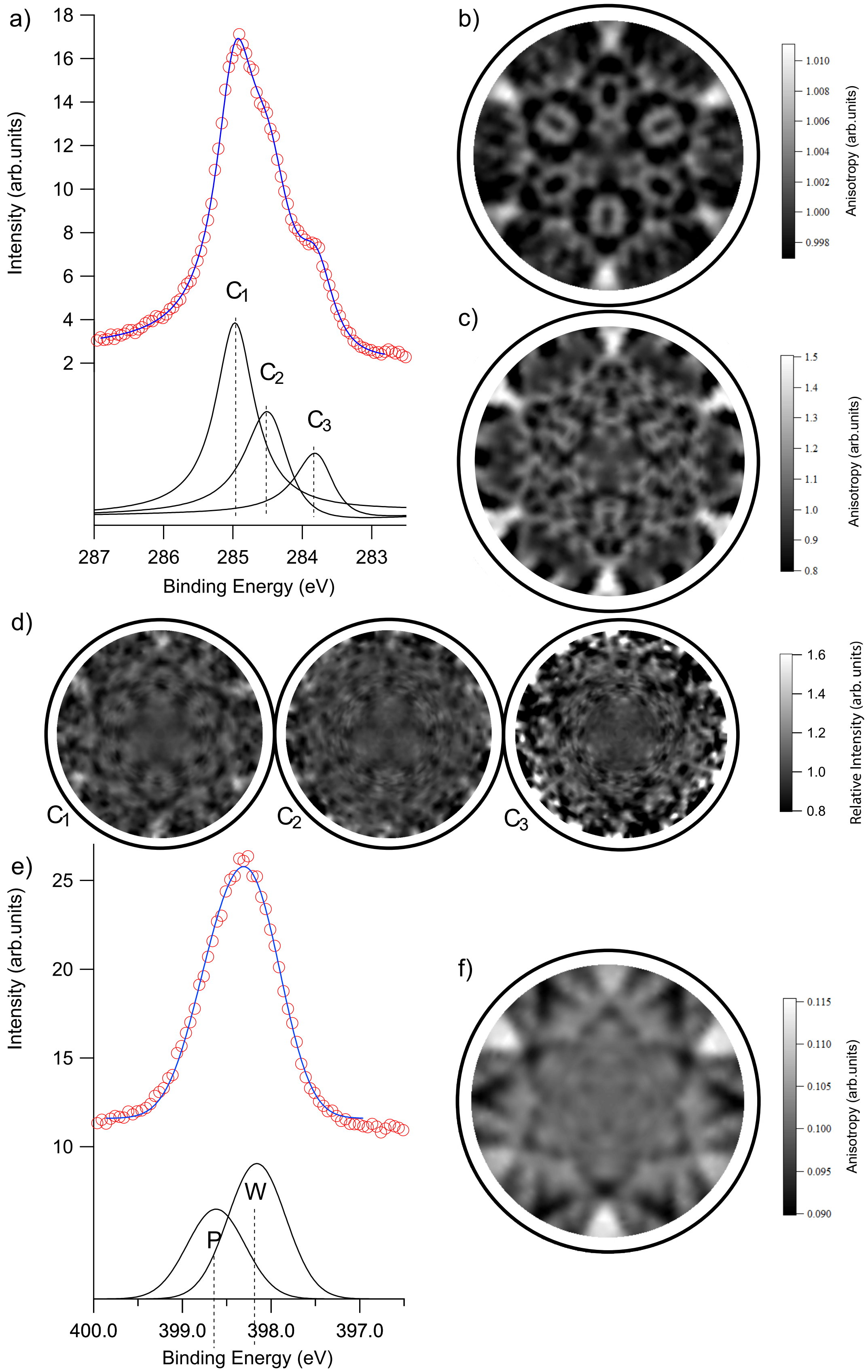

Figure 4.4 XPS and XPD for carbon and nitrogen. The peaks were energy calibrated to the rhodium bulk Rh3d$_{5/2}$ peak. The red circles are experimental data points, blue the fitting results and black single fitting curves. Top row: a) Photoemission spectrum of C1s. b) XPD pattern of the C1s as a full peak. c) EDAC simulation of a bilayer graphene structure. d) Deconvolution of the XPD patterns. e) X-ray photoemission spectrum of N1s. f) XPD pattern of the N1s.

4.2.3.5 Photoemission of the transferred sample

The transferred layers shown with optical microscopy and Raman spectroscopy were equally analysed by XPS and XPD. XPS allows to identify the transferred elements which were not possible to identify, especially for the *h*-BN layer, with the optical methods, as *h*-BN has a low raman cross section at the used laser wavelength and the E_{2g} mode is convoluted with the defective graphene D mode.

In subfigure 4.5 a) the XPS spectra of the N1s elastic line is shown. The spectrum can be deconvoluted in three distinct gaussian lineshapes with the energies: $E^t_P = 396.89 \pm 0.01$ eV for the pore site of the *h*-BN, $E^t_W = 397.79 \pm 0.01$ eV for the wire site, and an additional peak $E^t_A = 398.92 \pm 0.05$ eV. A shift with respect to the values of the pristine sample can be observed. This shift can be calculated taking the difference between the nitrogen energy of the pore state of the untransferred sample and the energy of the pore state of the transferred sample. The energy shift results to be $\Delta E = 1.73$ eV and may be due to the different insulating substrate. The additional peak E_A may arise from the chemical treatment during the transfer procedure and residuals reacting with the *h*-BN during annealing.

This picture is also supported by the analysis of the carbon peak. The transferred carbon peak is shown in subfigure 4.5 b), where the experimental data are the red circles, in a blue line the fitting result and in black the single fitting peaks. The fitting was performed using three Donjach Sunjic line shapes with the energies: $E^t_{C_1} = 283.26 \pm 0.01$ eV, $E^t_{C_2} = 284.17 \pm 0.03$ eV, $E^t_{C_3} = 284.91 \pm 0.03$ eV. The peak C^t_1 is the same as in the untransferred sample C_1. This can be verified by adding the energy shift calculated beforehand to the first peak $E^t_{C_1} + \Delta E = E_{C1}$. The C_1 species can thus be transferred to the SiO_2 while the same is not true with the peaks C_2 and C_3, which arise now at higher binding energies compared to the C_1 peak. The higher binding energy of these carbon species indicates a chemical shift towards bound states, which can be measured with oxidation or binding of carbon in molecules. This two species can be attributed to residual carbon originating from the transfer from the rhodium substrate to the silicon oxide, which includes alkanes deriving form the used TOA, PMMA residues due to incomplete sample rinsing and oxidation during air transport. In subfigure 4.5 c) and 4.5 d) the XPD plots of N1s and C1s are shown respectively showing a clear structure of single layer *h*-BN and multilayer graphene (graphite) structure. The transfer thus has no effect on the crystallinity of the sample. The transfer ratios are shown in the supplementary information in figure 4.1.

4.2.4 Conclusions

The growth of *g*/*h*-BN/Rh(111) heterostructures on the Rh(111)/YSZ/Si(111) Sinergia wafers following the recipe of Roth et. al. [33] is feasible for the self assembly of lateral heterostructures. The presented results show the growth of a lateral heterostructure which can be observed by STM analysis while XPS and XPD analysis show the presence of crystalline *h*-BN and graphene on the surface 4.3, 4.4.

The XPD patterns instead suggest the presence of a multilayer stacked graphene which can be confirmed by EDAC simulations and is probably due to the lack of the self terminating condition, because of the high pressure growth conditions (millibar pressure). The XPS shows three components in the carbon XPS spectra, indicating diverse carbon species on the surface. The structure of these components has been deconvoluted from an energy resolved XPD. Of the three components only one has a clear structure, while the other components appear weak features compared to the first and can be attributed to an amorphous structure. The crystalline part of the spectrum together with the crystalline pattern of the N1s peak can be observed in the STM images, where the junction

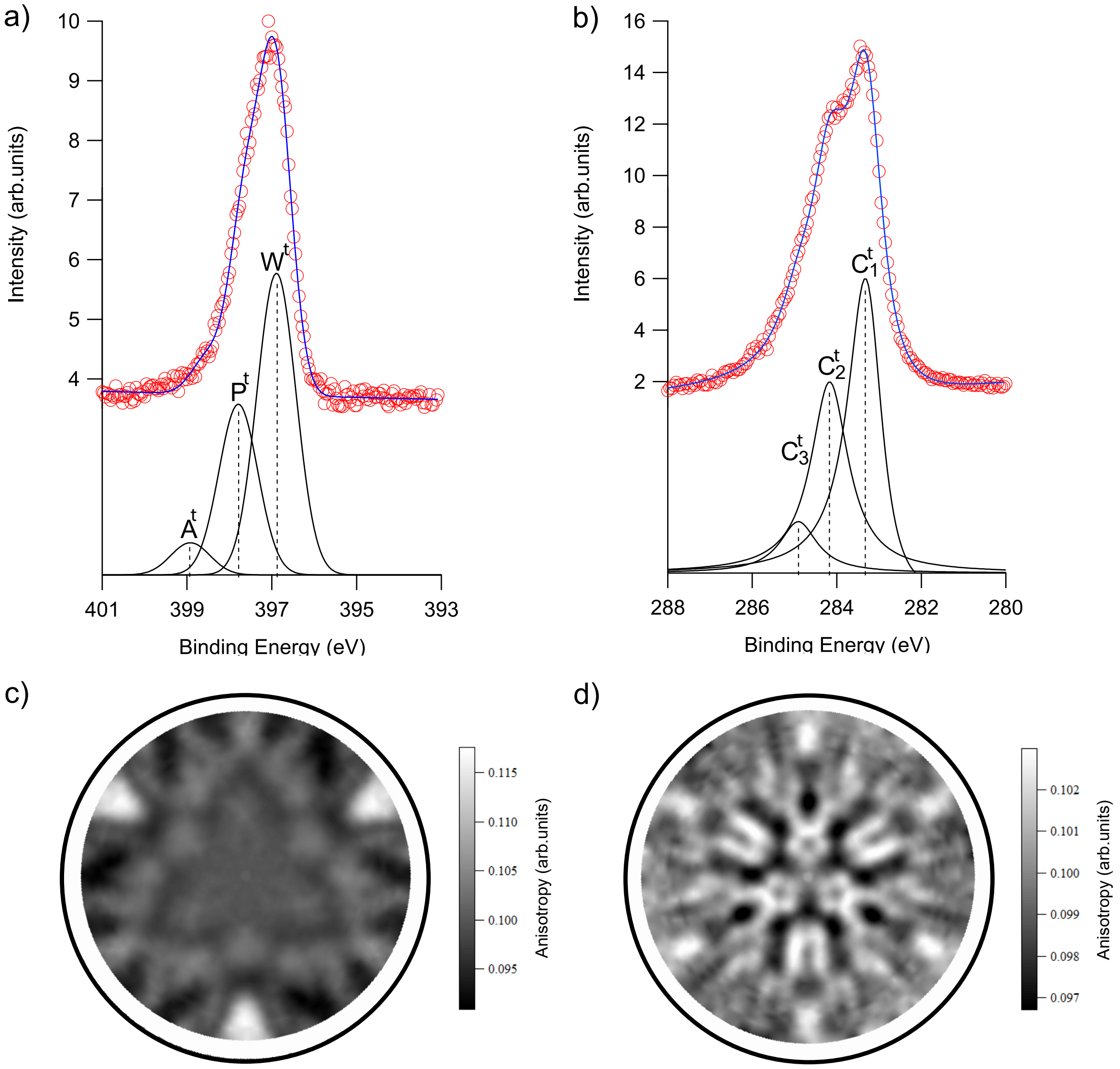

Figure 4.5 XPS and XPD spectras of the transferred layers on the SiO_2 substrate. The XPS spectras are shown as: in red the experimental data; in blue the fitting result; in black the single fitting peaks. In a) XPS spectrum of the N1s region of the *h*-BN nanomesh showing the characteristic splitting of the nanomesh, with an additional peak A^t. In b) XPS spectrum of the C1s region. Three fitting peaks were used with variable asymmetry of the peaks. The peak C_1^t is energetically the same as the C_1 in the pristine sample, while the other peaks arise during the transfer. In c) XPD pattern of the N1s species. In d) XPD pattern of the C1s species, integrated over the full peak.

between graphene and *h*-BN can be observed. The graphene, which was grown in a second step, can be shown to substitute the *h*-BN structure in an atom by atom fashion in this junction, confirming directly the findings of Brugger et. al. [114], Laskowsky et. al. [117], and Wang et. al. [116]. These results are summarised by the figure 4.6 a) showing a proposed model for the pristine heterostructure sample on the Rh(111)/YSZ/Si(111) sinergia wafer and the different measurements which support the model as icons.

The structure can be transferred to an other substrate with success. The transfer onto a SiO_2 substrate opens the characterisation methods to a whole new palette of techniques like optical microscopy and Raman spectroscopy, with the option to directly compare these to photoemission techniques. The shape and macroscopic growth of the graphene can be seen in optical microscopy 4.1, where a grain like structure becomes evident. This grain structure can be seen in high contrast to the background in Raman spectroscopy, exhibiting a strong 2D feature visible in figure 4.2. Comparing the measured Raman spectras to literature it is evident, that the grain structures consist of multilayered bernal stacked graphene, while the single layer regions exhibit a highly defective structure with a high D Raman band. A clear shoulder in the raman G peak indicates moreover a functionalisation of the graphene, suggesting transfer residuals on the surface which affect the graphene quality. These results can be compared to the photoemission results in figure 4.5 where chemical shifts can be observed in the carbon and nitrogen peak, supporting the model with transfer residuals. The XPD plots, on the other hand, confirm the crystalline status of the *h*-BN and graphene also after the transfer. The proposed model for the transferred sample is visible in figure 4.6 b) where the supporting measurements are again shown as icons.

The presented data show the presence of lateral heterostructures while there is no evidence for vertical heterostructures, which differs to the findings of Roth et al. [33] partially. The experiment was although limited to the test of a rhodium substrate and

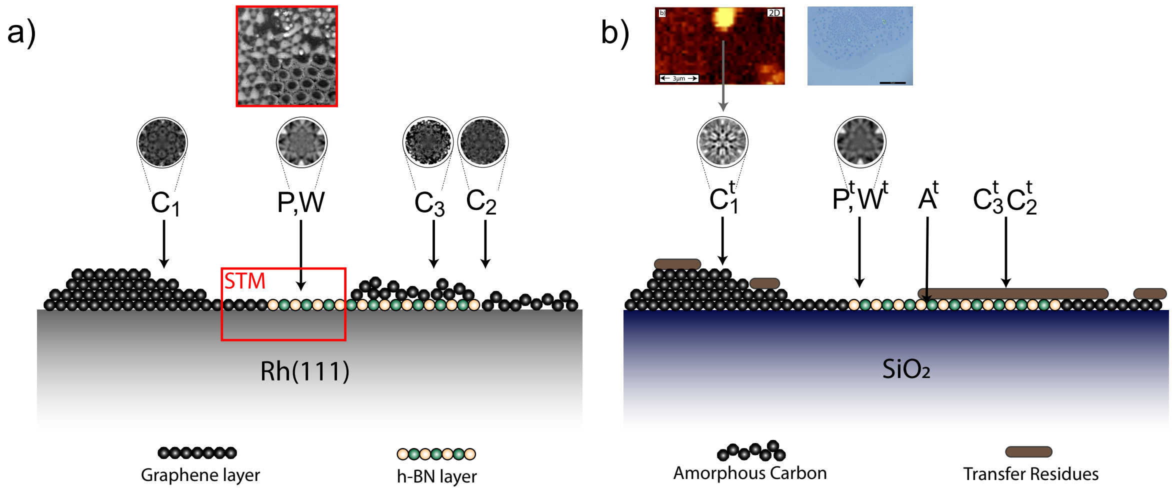

Figure 4.6 Proposed model of the heterostructure arrangement, a) before and b) after the transfer. The icons over the stick and ball plot represent the measurements supporting the proposed structural arrangement. XPS measurements are shown as characters.

should be attempted also on a copper substrate following the recipe of Roth et. al. in the case of copper [24]. Further analysis of the transferred sample should be taken into account including the measurement of the resistivity of the dark concentric regions (D) visible in figure 4.1 contacting the region directly with microcontacts or a 4-point probe STM. Furthermore, the lateral arrangement of the heterostructure could be unveiled in a simpler way with the usage of a *h*-BN sensitive raman setup.

4.3 Supplementary Information

4.3.1 Optical image contrast analysis

The measured optical images were used to determine the size of the structures on the sample and additionally the optical contrasts were calculated. The images were taken using a green light filter at $\lambda = 532\ nm$ wavelength. To obtain the sizes of the measured objects a cut visible in figure 4.7 a) in orange was used (cut not shown). The length of the cut was compared to the microscope scale obtaining the size of $D = 191.0\ \mu m$ for a length of $P = 1000$ pixels, while the microscope scale measures $P = 262$ pixels for $D = 50.0\ \mu m$. With these two points, it is now possible to extrapolate the size of the dark grains with a cut shown in 4.7 a) as a red arrow and plotted in subfigure 4.7 d). The full width at half maximum of the grain is 22 pixels. Extrapolating linearly the size of the grain is thus $D = 4.2\ \mu m$.

The same cuts can be used to determine the optical contrast of the features in the image. The optical contrast of sp^2 material can give an insight into the number of layers present on the SiO_2 surface [69]. To calculate the contrast cuts were made through the image 4.7 a) and plotted using the y-axis as intensity and the x-axis as position (in pixels of the image). Then an average on the analysed feature and in the background was performed. These averages were calculated over the colored boxes in figures 4.7 b), c) and d). An image contrast is defined though the Weber contrast which uses the formula:

$$C = \frac{I_f - I_b}{I_b} \tag{4.1}$$

Where C is the optical contrast, I_f is the intensity on the measured feature and I_b is the contrast on the background of the image.

The contrast was calculated for a light region next to the dark concentric zones visible in subfigure 4.7 a) as a green arrow. This lighter region may be a wrinkle, where the h-BN layer was not successfully transferred. The optical contrast in this region is $C = 3.8$ %, which, comparing to literature is compatible with h-BN at 90 nm SiO_2 thickness and $\lambda = 532\ nm$ light wavelength [69]. The wrinkle extends also through the concentric dark region, which is a patch of grown graphene, suggesting the graphene to be arranged on top of the h-BN. This is the only indirect hint for the existence of a vertical g/h-BN/Rh(111) heterostructure. In order to proof the claim further Raman measurement would be needed.

The optical contrast of the concentric dark region (subfigure 4.7 a) blue arrow) and a dark grain (subfigure 4.7 a) red arrow) were also calculated. The cuts are shown in the subfigures 4.7 c) and 4.7 d) respectively. The found contrasts are $C = 9.0$ % for the dark concentric region and $C = 18.6$ % for the dark grain. These values are compatible with a single layer and a double layer graphene respectively [102], [103].

4.3.2 Angular Resolved Photoelectron Spectroscopy

The exfoliated g/h-BN/SiO_2 sample was analysed with Angular Resolved Photoelectron Spectroscopy (ARPES), to investigate the Dirac cones present in graphene. The presence of a measurable Dirac cone is a direct proof of the presence of graphene. The electronic band dispersion was measured with a helium discharge lamp as radiation source using a toroidal grating momochromator to select the He II α radiation at an energy of $\hbar\nu =$ 40.8 eV. In figure 4.8 a) the electron energy dispersion in direction $\overline{\Gamma K}$ is shown. The dominant band is the π band, which shows a linear dispersion towards the Fermi energy (E_F) marked with red triangles. In figure 4.8 b) a zoom in of the interested area is presented. The dirac cones can also be observed at the Fermi surface with a momentum distribution plot shown in figure 4.8 c). The momentum plot shows clearly a six fold

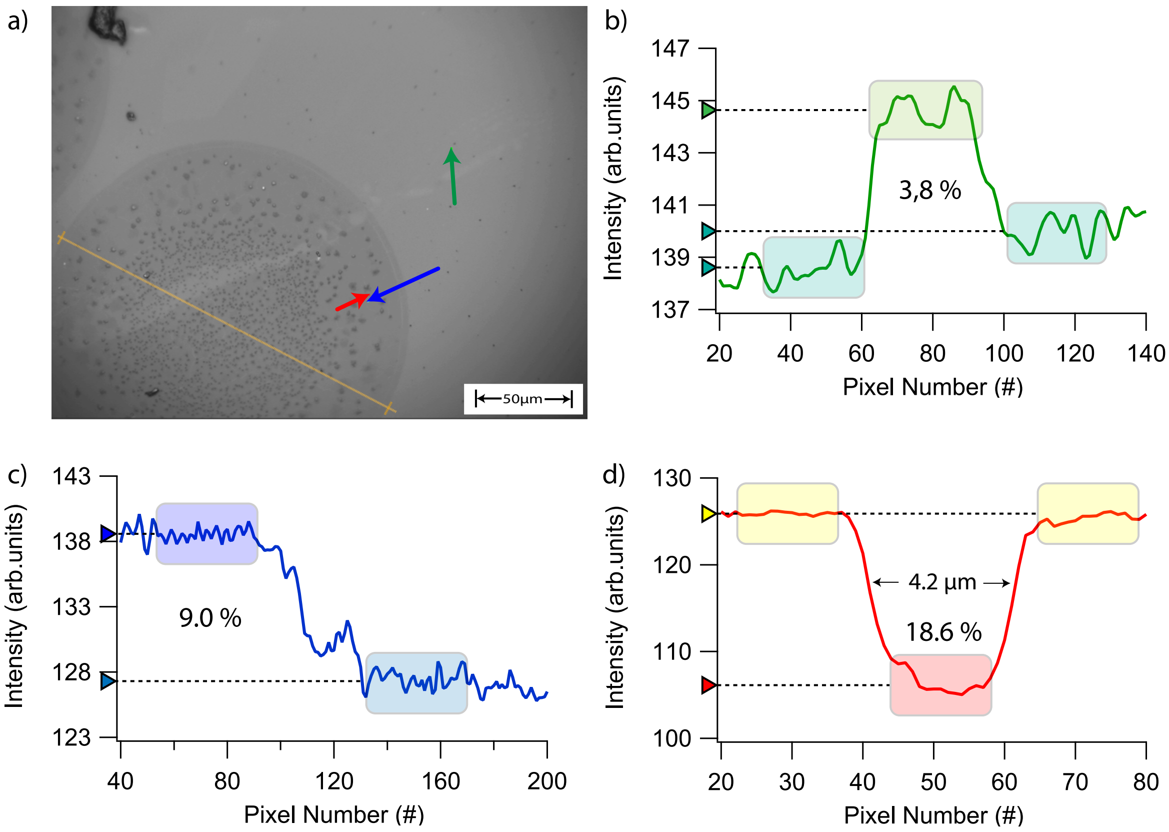

Figure 4.7 Optical contrast analysis performed on the cuts shown with the colored arrows. a) Analysed figure of a g/h-BN/SiO$_2$ transferred sample. In orange the estimation of the size of a concentric dark region which corresponds to $D = 191.0\ \mu m$ while the orange cut measures $P = 1000$ pixels. b) Contrast of a light wrinkle crossing the sample, corresponding to the green cut in the figure. This wrinkle may be an area where the h-BN has not been transferred. c) Contrast on the border of the dark concentric structure. d) Contrast of a dark grain.

symmetric intensity modulation at the K and K' location.

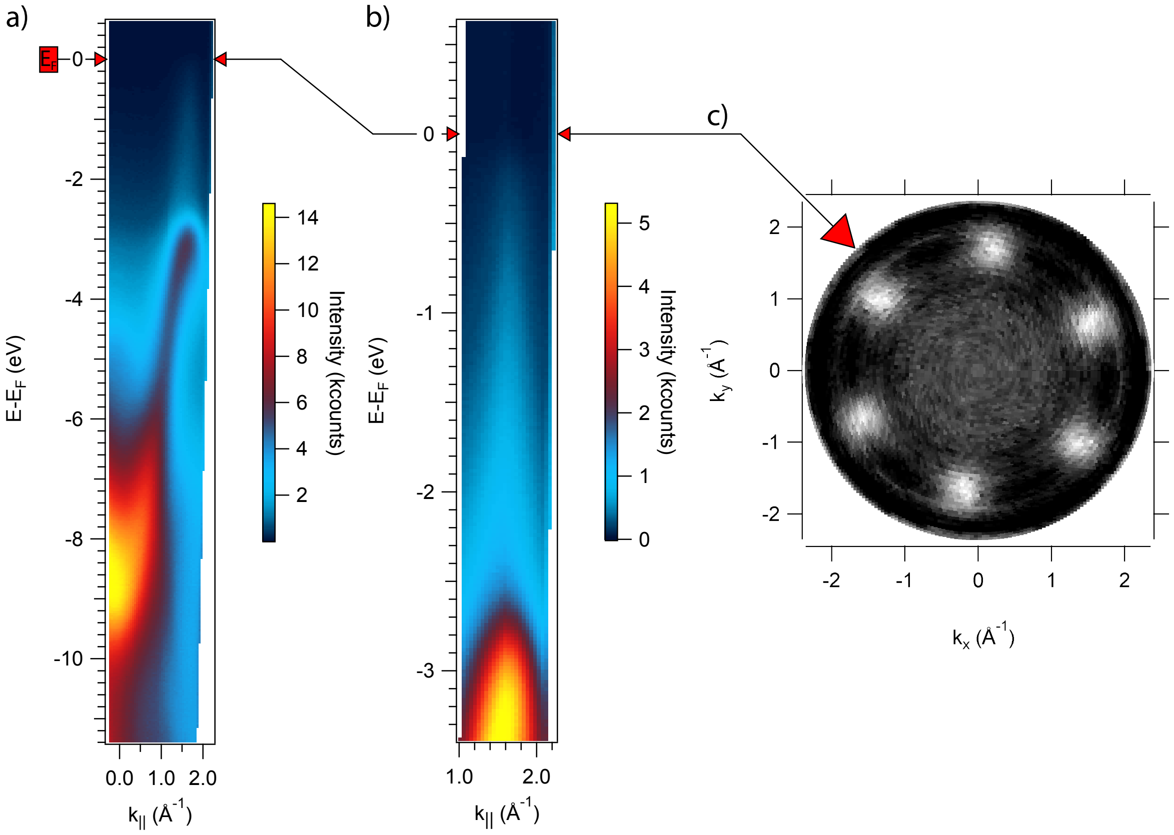

Figure 4.8 Energy distribution map of the ARPES measurement on g/h-BN/SiO$_2$. In a) $\overline{\Gamma K}$ direction plot, with a visible π band of the graphene dispersing linearly to the Fermi energy as a function of the parallel momentum vector $k_{\|}$. In b) zoom into the region under the Fermi energy and K point of the brillouin zone. In c) momentum distribution plot at the fermi energy, showing six distinct dirac points at the K and K' points.

4.3.3 Transfer ratio

XPS data gives insight over the transfer ratio of the materials using the TOA-assisted electrochemical delamination process. The transfer ratio T can be defined as the ratio of the XPS signal of the transferred element I_t divided by the pristine XPS element signal I_p, using the formula:

$$T = \frac{I_t}{I_p} \tag{4.2}$$

Nevertheless, it has to be said, that transfer ratios can vary widely from sample to sample. Here we present the transfer ratio of the best performing sample, from which the data of the main section originates.

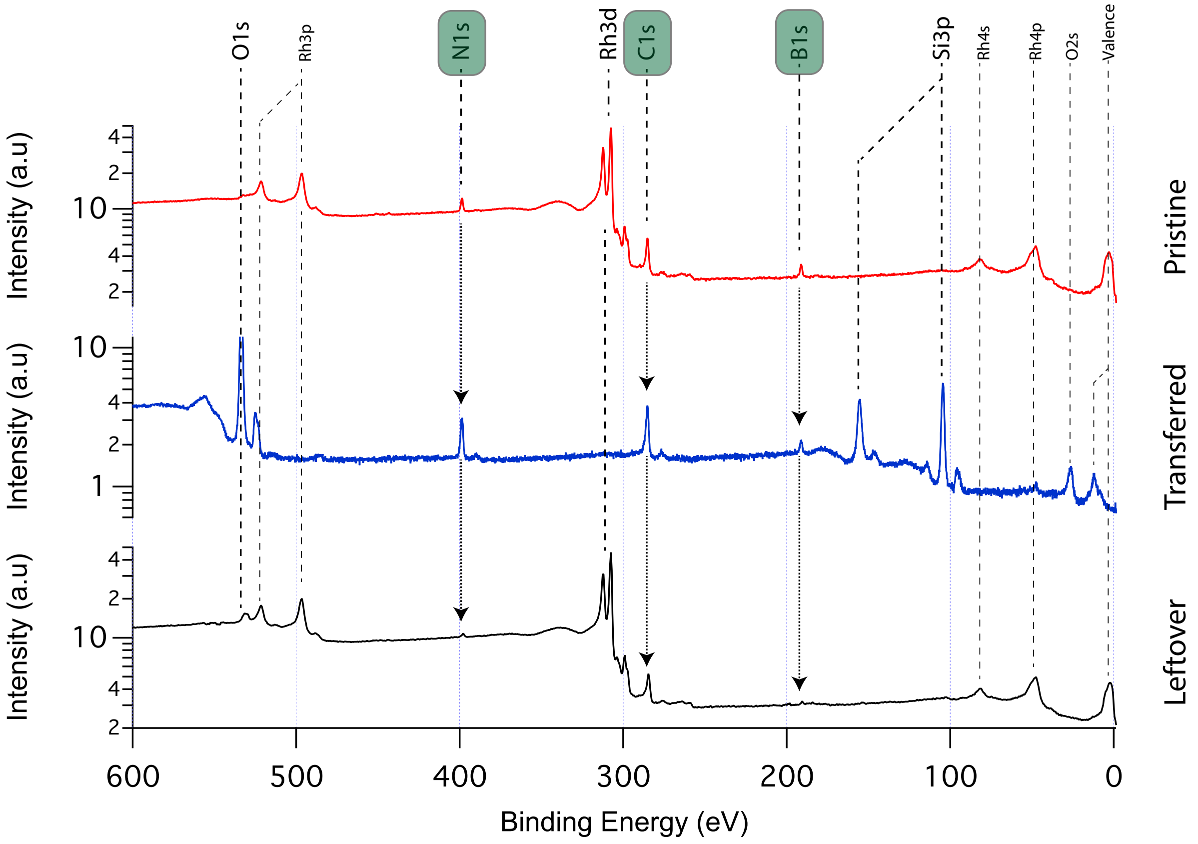

Figure 4.9 Survey spectras of the pristine (in red), transferred (in blue), leftover samples (in black). The spectras were taken using a MgK_α source with 1253.6 eV photon energy. The leftover sample is the remaining rhodium piece after electrochemical delamination. The dashed lines indicate the electron subshell excitations. The elements in the green boxes are transferred elements.

In figure 4.9 the survey spectra of the pristine, transferred and leftover samples are shown. The spectra indicate the transfer of carbon, boron, and nitrogen from the pristine sample to the transferred substrate. The leftover sample represents the rhodium substrate after electrochemical delamination. The leftover was rinsed with microfiltered water to dissolve remaining salts from the chemical solutions. On the leftover sample little amounts of nitrogen and boron are left. The leftover rhodium substrate could be

Element	Transfer	Leftover	Missing
Nitrogen	58.8 %	26.4%	14.8%
Boron	58.3%	13.2%	28.5%
Carbon	80.6%	81.7%	-62.3%

Table 4.1 Table of transfer ratios calculated form the spectra in 4.10. The negative value for the missing carbon signifies, that carbon is added in the transfer process.

reused for a second preparation.

The single detail spectra for the elements $N1s$, $B1s$, and $C1s$ are shown in figure 4.10 for the pristine, transferred and leftover sample. The areas of these spectra are used to calculate the transfer ratios for the elements. The same formula can be used to calculate the percentage of material which remains untransferred. The difference between 100% and the sum of the transferred and untransferred ratio is the missing amount, which was lost during the transfer. The used peak areas are marked in grey shading. The transfer ratio for the carbon has to be taken as an upper limit, as the transferred and leftover percentage score more than 100%, indicating the addition of carbon during the transfer process. The results for the transfer is resumed in table 4.1.

4.3.4 Possible origin of the C_2 peak

The origin of the structure in the XPD plot of the C_2 structure shown in figure 4.4 might also arise from a carbide structure in the rhodium substrate. Rhodium, as also nickel, might adsorb carbon forming a carbide structure. Albeit a carbide structure in

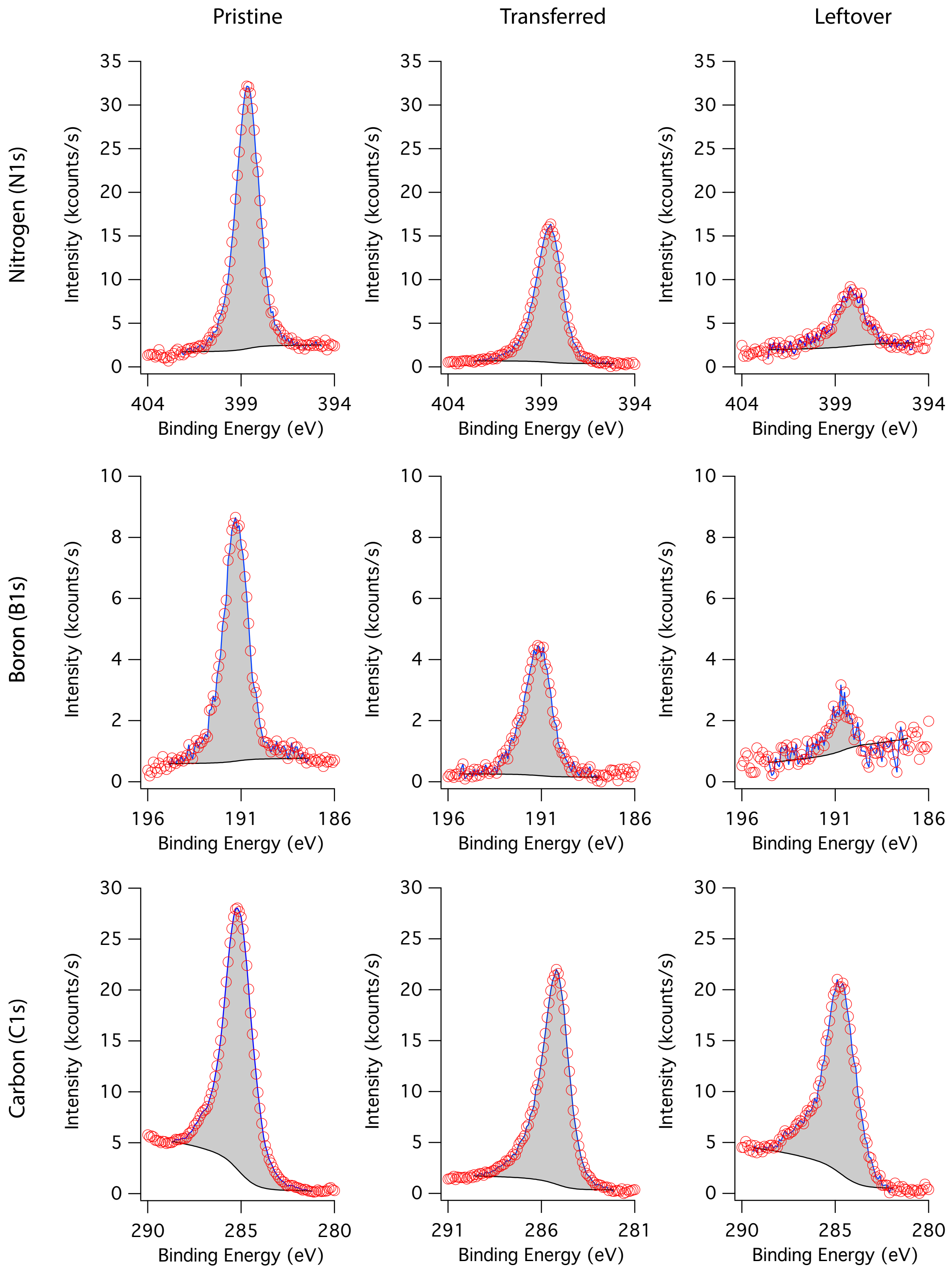

Figure 4.10 Comparison between single peaks of the pristine, transferred and leftover sample. The measurements were taken using a MgK_α source with 1253.6 eV photon energy. The peaks were subtracted by a constant and displayed with the same scale for comparison. In the first row the single peaks for nitrogen $N1s$, the second row for boron $B1s$ and the third row for the carbon $C1s$. From the peak areas the transfer ratios are calculated.

the rhodium substrate should not be affected by the electrochemical delamination of the 2-dimensional material on the surface, an XPD pattern should be still visible on the leftover rhodium substrate after delamination. In figure 4.11 a) the XPD plot of the C_2 contribution is shown next to an XPD plot b) taken form a leftover rhodium substrate. A faint structure in the pattern is visible at the center of the plot which can be compared to the XPD plot of the C_2 peak.

To strengthen this argument the XPD pattern of the rhodium carbide was simulated with EDAC. The carbon must be placed in the interstitial sites of the rhodium structure, which are the tetrahedral and octahedral sites of the crystal lattice. The resulting XPD plot of the carbon in the tetrahedral position of the rhodium crystal structure is shown in figure 4.11 c), which can be compared to the XPD plot in the subfigures a) and b). In 4.11 d) the cluster with carbon in the interstitial tetrahedral site for the EDAC calculation is shown. The plots show a clear similarity suggesting the origin of the C_2 contribution to be formed from a rhodium carbide located in the tetrahedral interstitial site.

Nevertheless, the XPD structure in the leftover sample might also arise from partially untransferred graphene or graphite on the sample. The experiment should be repeated using a method for the removal of untransferred graphene to proof the existence of the carbide structure.

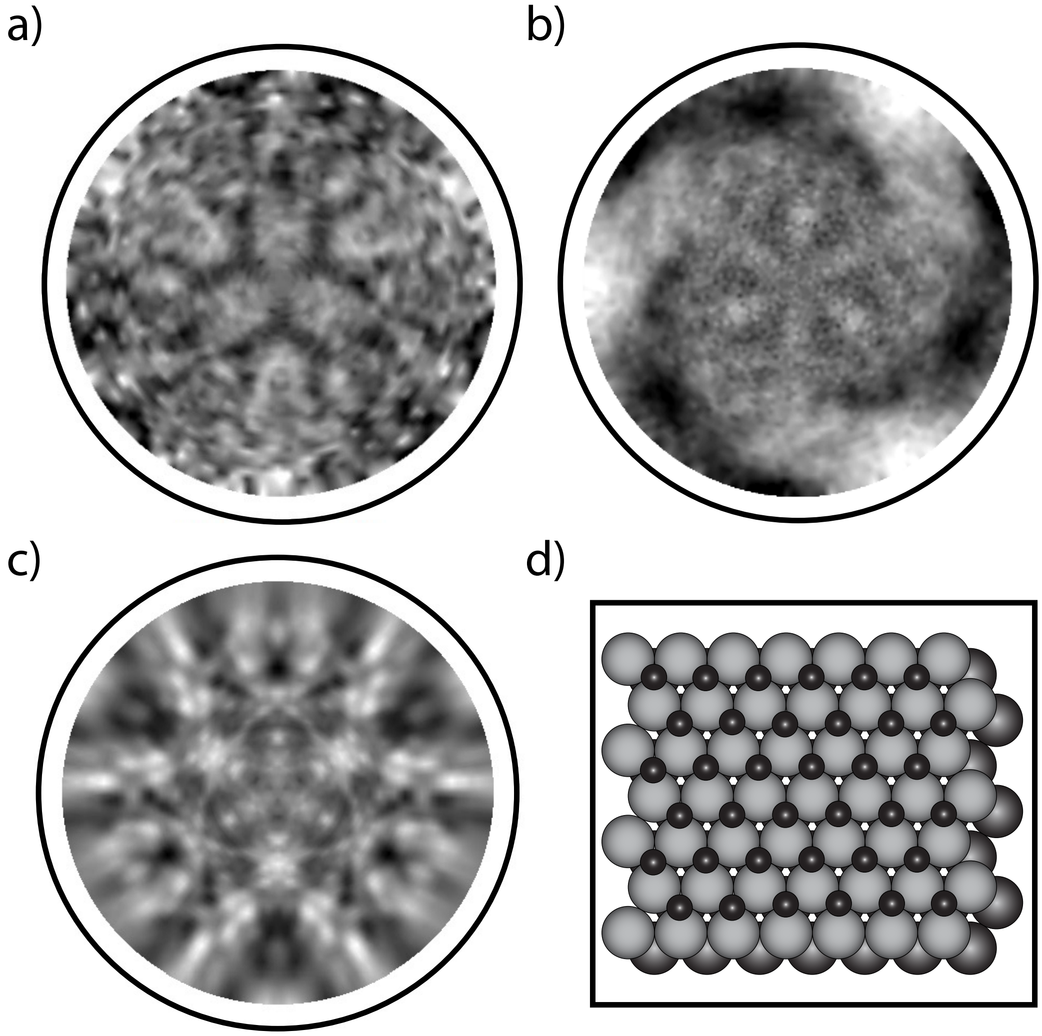

Figure 4.11 XPD patterns of a) the C_2 peak as shown in figure 4.4. b) Comparison with the C1s XPD plot of a leftover rhodium substrate after electrochemical delamination. The ring three fold wing structure at high polar angles is an artifact due to three fold averaging. c) EDAC simulation of a rhodium carbide structure, where the carbon atoms are located in the interstitial tetrahedral (hcp) sites of the crystal lattice. d) Sketch of the rhodium crystal with the carbon atom positions.

5 Molybdenum Diselenide on hexagonal Boron Nitride: A new heterostructure

In order to exploit the capabilities of in situ grown *h*-BN on 4-inch Sinergia films and further study the growth of heterostructures on *h*-BN nanomesh, an experiment to grow molybdenum diselenide ($MoSe_2$) on the *h*-BN nanomesh was carried out. In this purpose, a collaboration at the LANES laboratory with the research group of Prof. Andras Kis at EPFL Lausanne [1] was started, where $MoSe_2$ may be grown by molecular beam epitaxy. After growth of $MoSe_2$/*h*-BN heterostructures on Rh(111) the treated wafers were returned to the Sinergia laboratory at the University of Zurich for structural analysis and electrochemical delamination.

In this chapter we focus on the data obtained at the University of Zurich, the combined results of both groups, including the growth methods are shown in the publication *Electronic Properties of Transferrable Atomically Thin* $MoSe_2$ *Heterostructures Grown on Rh(111)* [34].

---

[1] http://lanes.epfl.ch/

5.1 Introduction

Molybdaenum diselenide ($MoSe_2$) belongs to the family of TMDC's (Transition Metal Dichalcogenides). Its single layer consists in a Mo (molybdenum) layer enclosed by two Se (selenium) layers. One structural arrangement in which $MoSe_2$ can be found is shown in figure 5.1. In other arrangements the positions of the Se atoms are shifted in their positions with respect to each other, giving rise to the so-called 1T and 2R arrangements in the Ramsdell polytype notation. In this case, we will focus on the 2H arrangement, which, as later will be shown, is the most probable for the growth of $MoSe_2/h$-BN. In the 2H arrangement the Mo atoms occupy a sublattice of the hexagonal sheet, while the Se atoms occupy the others. The Mo atoms are sandwiched between two Se sublattice layers and the Se atoms are located perpendicularly on top of each other. The second layer is shifted in respect to the first arranging in a ABAB stacked structure. The lattice configuration of the single layer is strikingly similar to the h-BN structure and therefore suggests the possibility of direct epitaxial growth of $MoSe_2$ on h-BN, even if the lattice mismatch between the two materials is 33% taking the $MoSe_2$ with respect to the h-BN [128].

The lattice parameters were calculated by Ding et. al. by LDA (Local Density Approximation) and PBE-GGA (Perdew-Burke-Ernyerhof) functional [129]. The lattice constant of the trigonal prismatic cell is $a = 3.33$ Å while the length of the Se-Se vertical bond is $h = 3.35$ Å. The bond length of the Mo-Se bond is $d = 2.55$ Å.

$MoSe_2$ monolayers possess particular optoelectronic properties, distinct form its multilayer counterpart [129]. Especially, the presence of a direct band gap at the K point of the Brillouin zone enables the observation of luminescence [130]. This direct band gap is only present in the single layer form of $MoSe_2$, as the band gap modifies to an indirect band gap between the Γ and the K point for two and more layers of material.

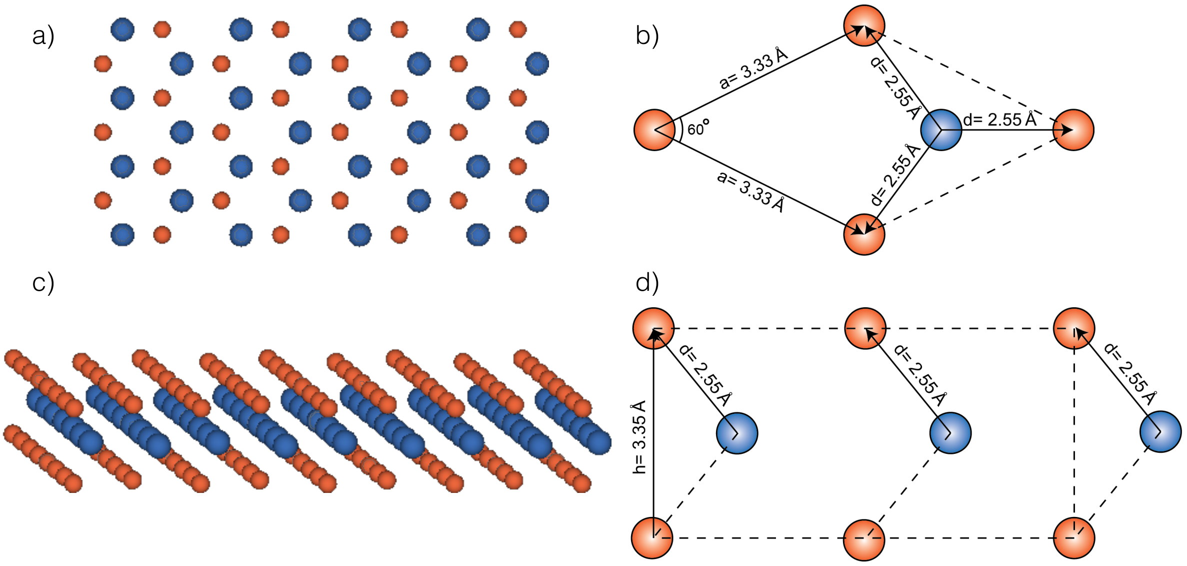

Figure 5.1 Sketches of the $MoSe_2$ structure from different angles, in orange the Se atoms, while in blue the Mo atoms. In a) a top view with the visualisation of the unit cell in b) including the atomic distances as reported in [129]. The Se and the Mo atoms are located in different layers as visible in c) and d). In this thesis, a monolayer of $MoSe_2$ refers to the full triple layer structure of Se-Mo-Se.

The combination of $MoSe_2$ in a heterostructured stack with h-BN to form $MoSe_2/h$-BN is, therefore, an attractive option for a device application. In particular the large band gap of h-BN [14], [131], [132] and the passivation of the metal substrate by the h-BN, enables new interesting growth conditions.

In a recent work [133] the study of $MoSe_2/h$-BN heterostructures was mainly obtained by the preparation through layer by layer mechanical exfoliation, which introduces impurities through the process and is not suitable for upscaling towards industrial applications. Moreover, experience from the graphene h-BN heterostructure, suggests increased carrier mobilities compared to its single standing counterpart, as a result, form the absence of dangling bonds at interfaces [9]. An attempt to directly grow $MoSe_2$ structures through CVD on SiO_2 was already published in 2014 by Wang et.al [134] while a year later the direct CVD growth of MoS_2 on h-BN [135] was performed. Therefore, direct growth of $MoSe_2$ on h-BN offers a straightforward possibility to ease the attempted production of monolayer $MoSe_2$ and study its properties on an insulating, chemically inert, monolayer material.

Here we present the results through the approach of molecular beam epitaxy on h-BN Sinergia films, which eliminates the separated exfoliation steps for the two materials. Additionally, this approach enables scalability for industrial applications through the use of a reusable, abundant and cost-effective sample basis as the Sinergia thin films described in chapter 2. The possibility to further electrochemically exfoliate the grown heterostructure material opens a new branch for possible device applications of $MoSe_2/h$-BN and an approach to large-scale industrial low-cost production.

5.2 Stoichiometry

The chemical composition, of the $MoSe_2/h$-BN heterostructures obtained from the University of Lausanne, was performed by XPS quantitative analysis. All following XPS spectra were measured using a non-monochromatised MgK_α radiation with an energy of $1253,6$ eV and a VG Escalab electron spectrometer. The chosen peaks of interest were: B1s, N1s to verify the presence of the h-BN substrate, Rh3d to verify the substrate composition and Mo3d, Se3d, Se2p to show the presence of the $MoSe_2$ species and carry out coverage calculations. C1s, O1s, Zr3d were also measured to quantify the presence of contaminants and substrate intermixing.

In Figure 5.2 the overview spectra of a $MoSe_2/h$-BN sample is shown. The presence of all expected elements on the sample confirms the successful preparation, while the absence of a Zr3d signal confirms no intermixing of the yttrium stabilized zirconium (YSZ) layer within the Sinergia thin film [30]. Clearly visible are the Mo3d and Se3p elastic lines confirming the deposition of Mo and Se species on the sample. The B1s and N1s peaks are also visible in the spectrum, while the B1s elastic line is small with respect to other lines due to its low photoelectron cross section at the used photon energy, the N1s elastic line is visible as a clear shoulder of the Mo3p$_{3/2}$.

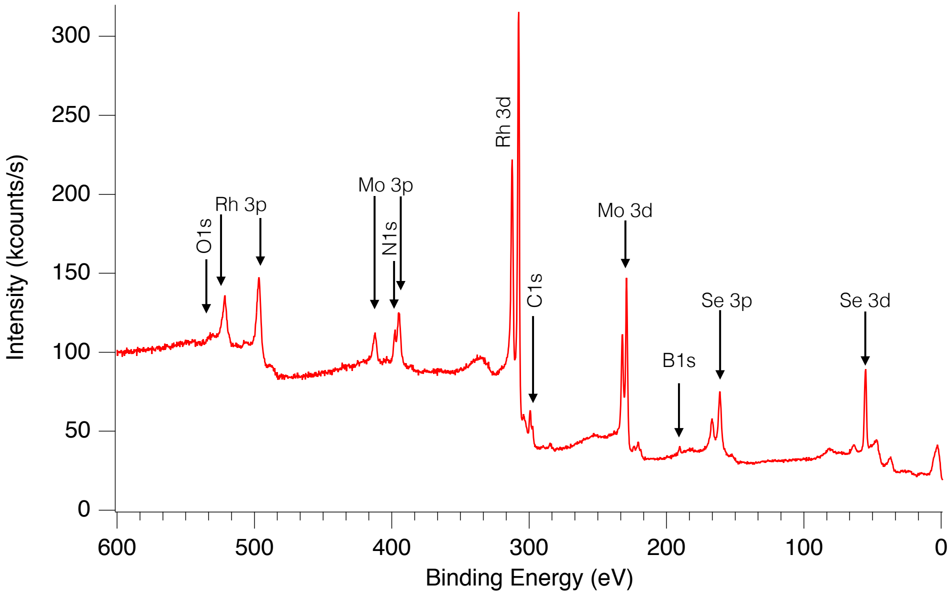

Figure 5.2 Overview spectrum of a MoSe$_2$/h-BN sample. Marked with arrows are the peaks of interest. The Rh3d elastic line represents the substrate material and is dominant in the spectrum. The Mo3d, Mo3p, Se3d, and Se3p elastic lines show the presence of the elemental parts of MoSe$_2$ and the B1s and N1s elastic lines show the presence of h-BN. The sample also shows near absence of residual carbon and oxygen confirming the low level of impurities on the sample. The absence of Zr3d elastic lines confirms the integrity of the rhodium thin film and no intermixing with the YSZ buffer layer.

In figure 5.3 the detail scans of the regions of interest are shown for a degassed sample (T=500 °C). figure 5.3 a) and b) show the Mo3d and Se3p elastic lines of the MoSe$_2$ and figure 5.3 c) and d) the N1s and B1s elastic lines of the h-BN. In red the experimental data are shown, in black the individual elastic lines were fitted with Voigt line-shapes and the fitting results are shown as blue lines. In the case of Mo3d a Se3s line was identified and shown as a dashed line, the same was performed for the N1s where the Mo3p was separated and shown in dashed line. The experimental results concerning energy positions and photoelectron line intensities from the fitting are reported in table 5.1.

The ratios of Se3p and Mo3d to N1s and B1s act as indicators for the amount of MoSe$_2$

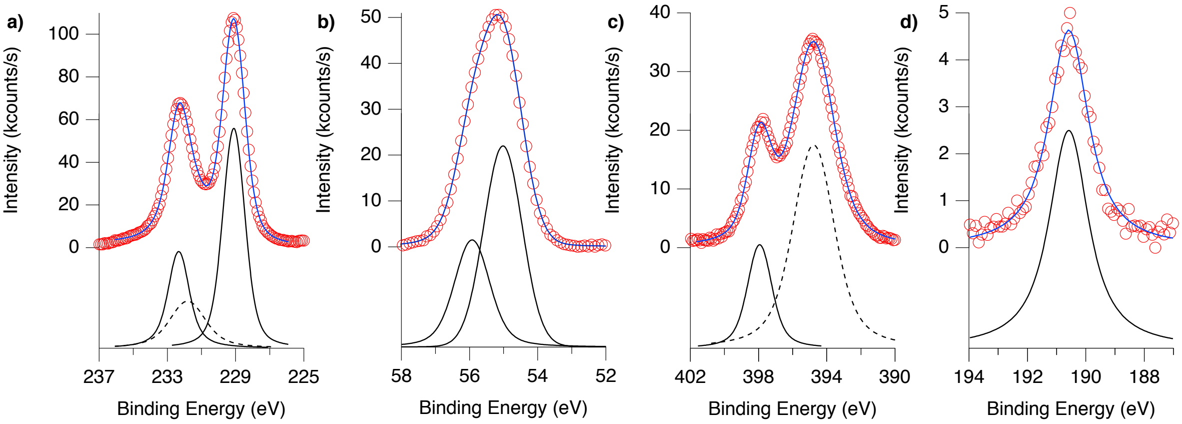

Figure 5.3 XPS detail scans of $MoSe_2/h$-BN using non-monochromatised MgK_α radiation. A Shirley function was subtracted in order to take the background into account. The data show that all the respective components of $MoSe_2/h$-BN are present. The corresponding binding energy of the respective photoelectron excitations are: a) $Mo3d_{5/2}$ = 229.1 eV and $Mo3d_{3/2}$ = 232.3 eV and the Se3s peak (dashed), b) $Se3d_{5/2}$ = 55.0 eV and $Se3d_{3/2}$ = 55.9 eV, c) N1s= 397.9 eV convoluted with the Mo3p peak (dashed), d) B1s= 190.6 eV. The red markers represent the experimental data. In blue the peak fittings results using a Voigt line shape per subshell excitation line. The individual photoemission lines from the fits are shown in black.

Core level	$Se3d_{5/2}$	$Se3d_{3/2}$	$Mo3d_{5/2}$	$Mo3d_{3/2}$	N1s	B1s
Energy (eV)	55.0	55.9	229.1	232.3	397.9	190.6
Fit Peak Area (a.u.)	62535	34799	195990	90032	38622	11421
Fitting Error (a.u.)	2080	2105	1993	4274	720	226

Table 5.1 Table for the fitting results of XPS data shown in Figure 5.3. Each column displays a measured subshell excitation, while the rows represent the data types: subshell excitation energy, fitting peak area, fitting error.

which was deposited on the sample. The B1s signal can be taken as a gauge, as we assume a single monolayer of *h*-BN on the sample. Therefore the B1s signal is the reference value for a monolayer to be compared to the signal of Mo. In order to calculate the amount of $MoSe_2$ on the *h*-BN further factors have to be considered:

1. The photoemission cross-section.
2. The density of atoms of the respective elements.
3. The inelastic mean free path of the electrons originating in the respective sample depth diffusing through the overlying layers.

A normalisation of the intensity for the photoemission cross-section and the atom density can be expressed with the equation 5.1:

$$I_i^N = \frac{I_i^0}{\sigma_i n_i} \tag{5.1}$$

Where I_i^N is the intensity normalised (N) by the photoemission cross section and the atomic layer density of the i-th element, I_i^0 the intensity obtained from the data fitting in Table 5.1, σ_i the photoemission cross-section taken from [136] and n_i the atomic layer density of the crystalline lattice of the respective element calculated with the lattice parameters of [113] and [129]. The density of atoms can be calculated from the crystalline structure of the *h*-BN and the $MoSe_2$.

In Figure 5.4 the parameters and geometry for the calculation of the atomic density for $MoSe_2$ (n_{Mo}, n_{Se}) and *h*-BN (n_N, n_B)are shown.

To estimate the atomic densities of B and N the lattice parameters of Corso et. al. were used [16], where the lattice constant of an *h*-BN unit cell was estimated to be $a_{h-BN} = 2.504$ Å. The primitive lattice cell of a honeycomb lattice is a rhombohedral

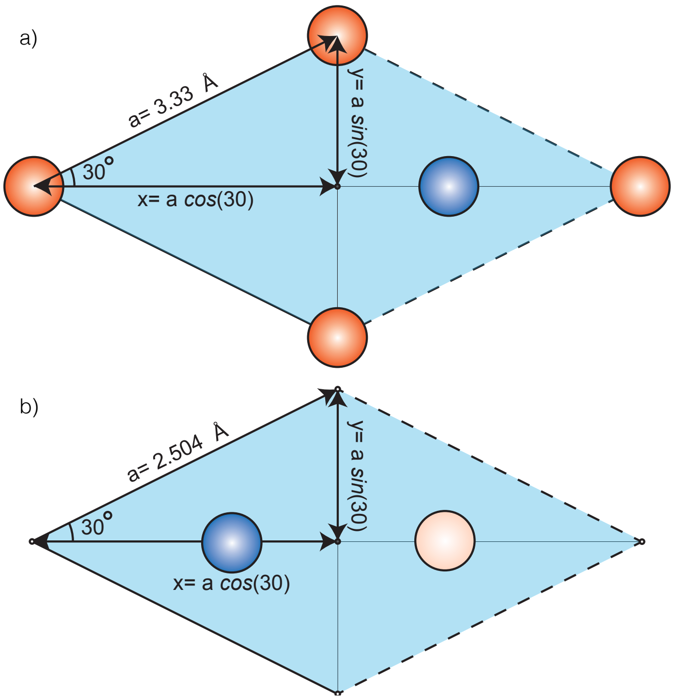

Figure 5.4 Schematic view of the a) $MoSe_2$ and b) *h*-BN with the calculation of the respective atomic densities. In orange the Se atoms, in blue the Mo and N atoms, in pink the B atoms.

unit enclosing two atoms, one B and one N. The atom density for B and N can so be estimated to be:

$$n_B = 1/A_B = 1/(2 \cdot a_{h-BN}^2 \cdot \cos(30) \cdot \sin(30)) = 0.184\ \mathring{A}^{-2} \tag{5.2}$$

Expressed in units of atoms per square Angstrom. Analogously the atom density of Mo and Se in the $MoSe_2$ structure were computed using the structure calculated by local density approximation by Ding et. al. [129]. The primitive lattice cell a $MoSe_2$ unit is trigonal prismatic, containing two Se atoms and one Mo atom. The lattice constant was calculated to be $a_{MoSe_2} = 3.330$ Å for the in-plane lattice constant and $h_{MoSe_2} = 3.350$ Å for the height of the prismatic structure. From these considerations the atom density for Mo and Se is:

$$n_{Mo} = 1/A_{Mo} = 1/(2 \cdot a_{MoSe_2}^2 \cdot \cos(30) \cdot \sin(30)) = 0.104\ \text{Å}^{-2} \tag{5.3}$$

The layer density of Se atoms is thus the density of the Mo atoms multiplied by factor of two. In the following calculations the double occupancy of Se in the unit cell will not be taken into account, so a 2:1 stoichiometric ratio is expected from the data.

As a practical visualisation of the data in table 5.1 normalised with equation 5.1 and the calculated atomic densities n_i is shown in Figure 5.5 a) where the elemental ratios calculated from the fitted intensities is shown in the form of a piechart. The percentages P are calculated as the contribution ratio of the intensity of each element I_i to the total intensity, which can be expressed in Equation 5.4:

$$P = \frac{I_i}{\sum\limits_{i=0}^{N} I_i} \tag{5.4}$$

The B1s to N1s ratio shown in figure 5.5 a) is near to the stoichiometric value of $I_B/I_N = 1$. This ratio suggests that the h-BN layer is not affected by the deposition of $MoSe_2$. In the same way, the Se3p to Mo3d are shown in 5.5 a) for the $MoSe_2$ layer. Given the structure of $MoSe_2$, a ratio of $2:1$ between Se and Mo is expected, as we did not include the double occupancy of Se per unit cell in the density calculation. The experimental data show a lack of Se which may be attributed to Se vacancies and oxidation of the top layer arising from transport through the air and subsequent annealing.

Albeit, the atomic ratio calculation does not include the influence of photoelectron attenuation, which may play a major role in the determination of the correct stoichiometry, as photoelectrons have a probability to be absorbed while traveling through material. These considerations can be combined with the following formula valid for a sample with uniformly layered structures:

$$I_i^{N'} = \frac{I_0}{\sigma_i n_i}\, e^{d_i/\Lambda_i} \tag{5.5}$$

Where i stands for the values of the respective elements, I_0 is the measured photoelectron intensity calculated fit peak area in table 5.1 using the data from figure 5.3, σ_i is the photoemission cross-sections taken from [136], n_i is the atom density and d_i is the thickness of the overlayer material, which both are calculated in the paragraph below. Λ_i is the inelastic mean free path of electrons travelling through overlying material. These values were taken from the NIST (National Institute for Standards and Technology) Standard Reference Database 71 [55].

Two different approaches of $MoSe_2$ thickness estimation will be presented. The first is of graphical nature, while the second bases on a strictly analytical basis.

5.2.1 Graphical Solution

In order to estimate the number of layers of $MoSe_2$ on top of the *h*-BN, the comparison of B to Mo and Se signal can be exploited. This can be achieved by recursively correcting the photoelectron damping factor as a function of the number of layers of $MoSe_2$. The correction factor has to include the number of layers of material the signal travels through, each with the photoelectric mean free path factor for the given photoelectron energies. The layer thicknesses is taken from the calculated values of Ding et al. [129] and the photoelectron mean free paths from the NIST database [55]. For the materials under discussion, the following matrix expresses the photoelectron mean free path as a function of the material the photoelectron travels through (columns) and the photoelectron energy expressed in subshell excitation line (rows):

Material	Mo	Se
Se3d	18.81 Å	25.38 Å
Mo3d	17.93 Å	22.40 Å
N1s	14.60 Å	19.53 Å
B1s	17.20 Å	23.01 Å

For the photoelectrons originating from the *h*-BN layer the equation for the corrected photoelectron intensity can be written as:

$$I_B^{N'} = \frac{1}{n_{Se}\sigma}\frac{I_0}{\Gamma} \cdot \exp\left(2\Gamma\frac{d_{Se}}{\Lambda_{Se}^B} + \Gamma\frac{d_{Mo}}{\Lambda_{Mo}^B}\right) \tag{5.6}$$

Where $I_B^{N'}$ is the intensity of the B species corrected for the atomic cross-section σ_B, the atom density n_B and the damping for the number of Γ overlying selenium and molybdenum layers. Γ, in this case, expresses the number of MoSe$_2$ layers. The case for nitrogen is analogous to the case of boron.

To compute the corrected intensity for Mo and Se a more involved calculation has to be performed. First, the MoSe$_2$ layer is composed of two layers of Se, this complicates the calculation as the ratio of Se intensity distribution between the top and the bottom layer is unknown. When assuming two or more layers of MoSe$_2$ this complication is greatly amplified. Nevertheless to estimate the amount of MoSe$_2$ with respect to the *h*-BN the model will assume the intensity to be evenly split between the different layers. Meanwhile a relatively big error which accumulates for every layer has to be taken into account to compensate for the even distribution assumption. However, the model shall only hold in the case of few layers of MoSe$_2$. Using this notions the intensity normalisation for Mo and Se can be written with the following formula:

$$I_{Mo}^{N'} = \frac{1}{n_{Mo}\sigma_{Mo}} I_0 \left(\sum_{i=1}^{\Gamma} \frac{1}{\Gamma} e^{iL} \right) \tag{5.7}$$

Where iL is the expression which models the number of layers the photoelectrons have to travel through for each emitting layer:

$$iL_{1Layer} = \frac{d_{Se}}{\Lambda_{Se}^{Mo}} \tag{5.8}$$

$$iL_{2Layers} = \frac{(3 \cdot d_{Se})}{\Lambda_{Se}^{Mo}} \frac{d_{Mo}}{\Lambda_{Mo}^{Mo}} \tag{5.9}$$

$$iL_{3Layers} = \frac{(5 \cdot d_{Se})}{\Lambda_{Se}^{Mo}} \frac{(2 \cdot d_{Mo})}{\Lambda_{Mo}^{Mo}} \tag{5.10}$$

$$iL_{NLayers} = \frac{(2i-1) \cdot d_{Se}}{\Lambda_{Se}^{Mo}} \cdot \frac{(i-1) \cdot d_{Mo}}{\Lambda_{Mo}^{Mo}} \tag{5.11}$$

The intensities of molybdenum and nitrogen or boron can now be compared to extract the number of layers of $MoSe_2$ as expressed in the following equation:

$$I_{Mo}^{N'} = n \cdot I_{N}^{N'} \quad \text{and} \quad I_{Mo}^{N'} = n \cdot I_{B}^{N'} \tag{5.12}$$

As the intensities depend recursively on the number of layers this equation can be graphically solved as shown in Figure 5.5 b) where the normalised intensities for Mo, B, and N are plotted in function of the number of layers N. The area of overlap between the intensity curves render an estimation of the number of $MoSe_2$ layers, which, in this case, is $N = 2.5 \pm 0.5$ layers.

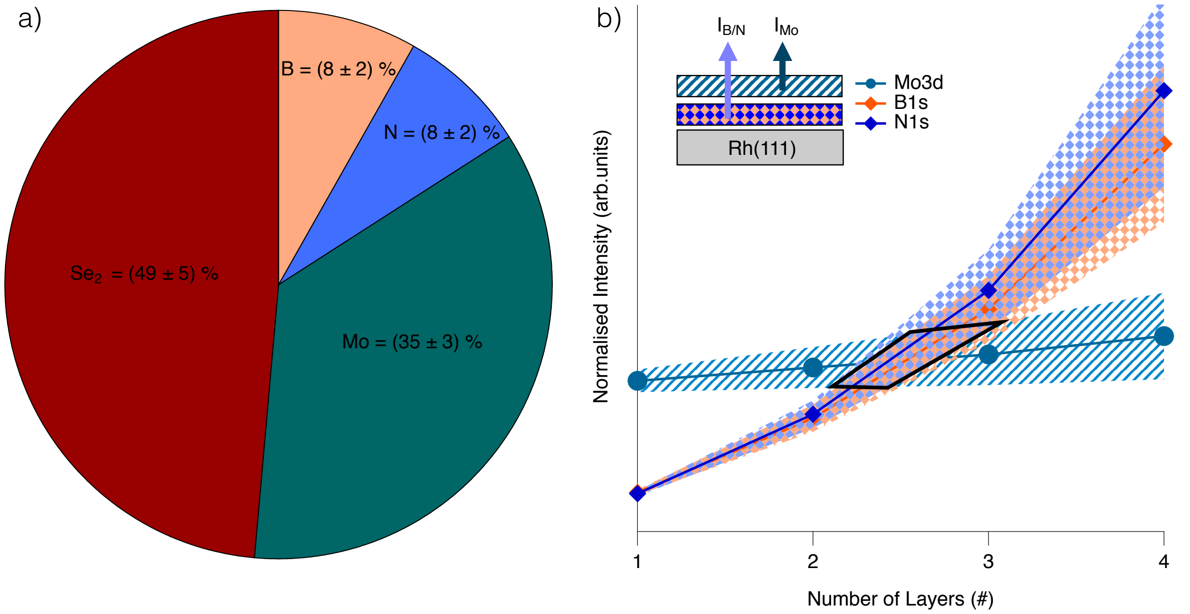

Figure 5.5 Ratio calculation between photoelectron emission intensities calculated in Table 5.3. The measured photoelectron intensities were normalised using the photoelectron cross-section and the atomic density for the investigated materials. The ratio of B to N is 1:1 showing the correct stoichiometry for *h*-BN. The Se to Mo ratio shows a slight deficit of Se, as the expected ratio between Se and Mo should be 2:1. Figure 2b) For the definition of the layer thickness a layer by layer growth model as shown by the inset in subfigure b) was used. For this purpose, the signal of B and N was used as the definition of a monolayer and compared to the Mo signal. For this calculation the inelastic mean free path of photoelectrons in the selected materials has been considered, the used values were taken from the NIST database. The comparison of Mo to B and to N intensity signals, in function of the number layers of $MoSe_2$ over *h*-BN, shows the Mo (green) signal to be equal (in the black trapezoid area) to the signal of 2 to 3 layers of B (orange) or N (blue). Therefore the thickness of $MoSe_2$ can be assumed to be between 2 and 3 layers.

5.2.2 Analytic Solution

The result in figure 5.5 b) is obtained graphically and should be verified by an analytical calculated layer model. With the same consideration as before we assume a uniform overlayer of MoSe$_2$ material. The intensities, in this case, depend only on the thickness of the overlayer. For an infinitesimal thickness dz of material we can write the equation:

$$dI_{Mo} = A\Phi\sigma_{Mo}\frac{n_{Mo}}{d_0} \cdot e^{-z/\Lambda}dz \tag{5.13}$$

Where I_{Mo} is the measured photoelectron intensity, A is the illuminated area, Φ is the photon flux, σ is the atomic cross-section, n is the bi-dimensional atom density while d_0 is the thickness of a complete MoSe$_2$ layer, dz is an infinitesimal layer of material, Λ is the photoelectron mean free path and z thickness of material the photoelectron travels through. The exponential factor corrects for the photoelectron damping in the material. We can integrate this equation form 0 to d in respect to the infinitesimal slice of material dz to obtain the intensity of the full thickness d of the damping material, obtaining:

$$\int_0^d dI_{Mo} = A\Phi\sigma_{Mo}\frac{n_{Mo}}{d_0} \cdot \int_0^d e^{-z/\Lambda}dz \tag{5.14}$$

$$I_{Mo} = A\Phi\sigma_{Mo}\frac{n_{Mo}}{d_0} \cdot \Lambda(1 - e^{-d/\Lambda}) \tag{5.15}$$

d_0 shall be the thickness of one monolayer. We may expand the exponential in a Taylor series to the first order which is correct for $d/\Lambda << 1$:

$$I_{Mo} = A\Phi\sigma_{Mo}\frac{n_{Mo}}{d_0} \cdot \Lambda(1 - 1 + d/\Lambda) \tag{5.16}$$

In a similar way the intensity of the boron signal is given as:

$$I_B = A\Phi\sigma_B n_B \cdot e^{-d/\Lambda} = A\Phi\sigma_B n_B \cdot (1 - d/\Lambda) \tag{5.17}$$

We can form the ratio of the two intensities:

$$\frac{I_{Mo}}{I_B} = \frac{\sigma_{Mo}}{\sigma_B}\frac{n_{Mo}}{n_B} \cdot \frac{\Lambda(\frac{d}{d_0}/\Lambda)}{(1 - d/\Lambda)} \tag{5.18}$$

Where d/d_0 represents the overlayer thickness expressed in the number of monolayers. We label the ratio of intensity, crosssections and atom densities as $R(I, \sigma, n)$ and simplify the expression as follows:

$$R(I) = R(\sigma)R(n)\frac{d/d_0}{1 - d/\Lambda} = R(\sigma)R(n)\frac{\Lambda}{d_0} \cdot \frac{d/\Lambda}{1 - d/\Lambda} \tag{5.19}$$

This equation can be solved for d/d_0 and yields as follows:

$$d/d_0 = \left(\frac{R(n)R(\sigma)}{R(I)} + \frac{d_0}{\Lambda}\right)^{-1} \tag{5.20}$$

Using an approximation of $\Lambda = 20$ Å, the calculated atom densities using the unit cell sizes calculated beforehand, the tabulated cross-section form Scofield et.al. [136] and the obtained photoelectron intensities form the experimental data in Table 5.1 we obtain a thickness of $MoSe_2$ of $d = 1.8$ ML of $MoSe_2$, where the boron of the *h*-BN layer defines the monolayer.

These results confirm the few-layer growth of $MoSe_2$ on *h*-BN, from a quantitative XPS point of view. The graphical and analytical results are comparable, resulting in a coverage of $\simeq 2$ monolayers of $MoSe_2$ material. Albeit, from a structural point of view and confirmed by STM [34], the growth of $MoSe_2/h$-BN could be in a mixed multilayer and monolayer fashion (Stransky-Krastanov type growth [137]) in the amounts, which appear as a monolayer to XPS analysis. In order to investigate this case, the following section will focus on the structural analysis of $MoSe_2/h$-BN.

5.3 Material Structure: LEED and XPD

To determine the structural properties of the growth of $MoSe_2$ on h-BN, two structure sensitive measurement methods were used. Low-Energy Electron Diffraction (LEED) shows the structural arrangement in the topmost layers of the structure and X-ray Photoelectron Diffraction (XPD) was performed to allow a more complete analysis of the multilayered structure. The LEED diffractometer was an Omicron with an actively cooled CCD camera. The LEED images were taken after sample degassing at 500°C and cool down to room temperature. In figure 5.6 a) a LEED image of $MoSe_2/h$-BN/Rh(111) is shown. The image was taken with an electron energy of 70 eV and was inverted for better contrast. The threefold symmetric diffraction spots of the h-BN are clearly visible, proving the presence of h-BN on the Rh(111) substrate as seen in figure 2.7. A weak moiré ring is visible with the highest intensity at the R30 rotated directions which indicates azimuthal disorder of the h-BN.

The inner structure in the LEED is related to the $MoSe_2$. The $MoSe_2$ appears to grow in preferential directions following the h-BN structure, with an azimuthal disorder forming a moiré ring. In subfigure 5.6 c) the linear intensity cuts through the LEED image which follow the lines of the same color in subfigure 5.6 b) are shown. As the LEED image represents the reciprocal space of the crystalline structure at the surface and the lattice parameters of h-BN are well known [16], an estimation of the lattice parameters of $MoSe_2$ can be given. Taking the distance in pixels across the LEED image between the features visible due to $MoSe_2$ coverage the calculated lattice constant can be estimated to be $a_{MoSe_2} = 3.3$ Å.

The alignment of the sample can be estimated through the evaluation of azimuthal cuts in the LEED figure. As shown in figure 5.6 b), circular intensity cuts were taken along the red and the two blue lines on the $MoSe_2$ features. The red circular cut was subtracted by the average of the two blue cuts at a higher and respectively lower polar angle, in order to take into account for the background. The obtained azimuthal plot is shown in figure 5.7. In red the data of the subtracted azimuthal cut is shown, while in black a smoothed version of the data is shown for easier visualisation. The data were fitted with six Lorentzians with a constant and a sinusoidal background following the formula:

$$f(\varphi, i) = C + A * \sin\left(\frac{(\varphi - P_0)}{\pi}\right) + \sum_{i}^{6} \frac{I_i}{(\varphi - i\frac{\pi}{3})^2 + B} \tag{5.21}$$

Where φ is the azimuthal angle, C the constant background, A the amplitude of the sinusoidal background, P_0 the phase of the sinusoidal background, I_i the intensities of the Lorentzian lineshapes, x_0 the positions of the Lorentzian lineshapes with a $\phi = 60°$ periodicity and B the width of the Lorentzian lineshapes. The Lorentzian lineshape value was fixed to the value obtained from the fit of the polar cut through the LEED image. This allows an estimation of the LEED resolution. The obtained fit shown in blue color in Figure 5.7, can successively be integrated and compared to the total integral of the azimuthal cut data. The region around the azimuthal angles $\phi = 300°$ were ignored as the data is affected by the shadowing of the electron source. The result of this calculation suggests a ratio $I_{ord}/I_{tot} = 42$ % of ordered to total material. This result hints to partially ordered growth of $MoSe_2$.

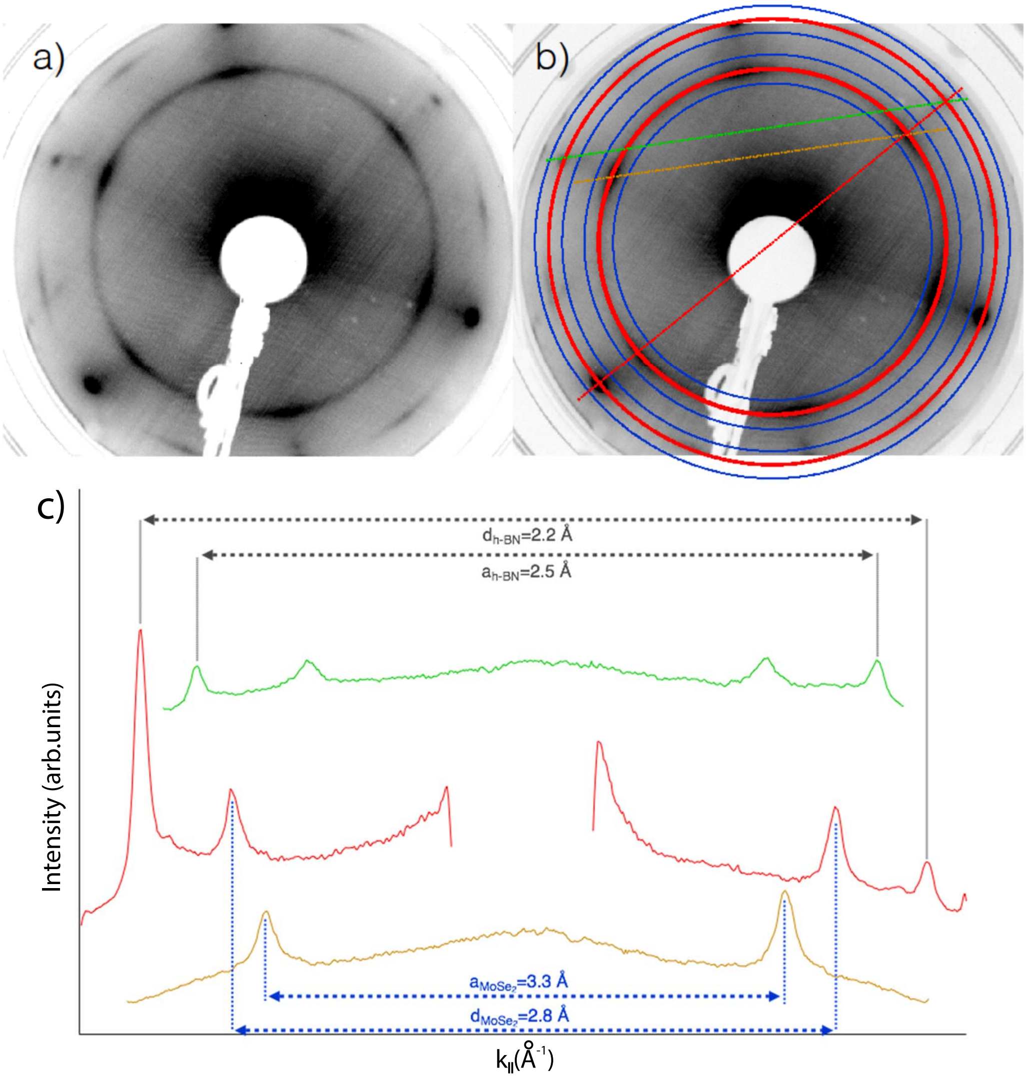

Figure 5.6 a) LEED picture of the $MoSe_2$/h-BN structure taken at 70 eV electron energy. Visible the h-BN diffraction spots with a slight R30 rotation and moiré ring, which indicates an azimuthal disorder of the h-BN layer. The 13/12 diffraction spots around the principal spots, arising from the h-BN nanomesh, are not visible after the $MoSe_2$ preparation. The inner ring is related to the $MoSe_2$ structure. The contiguous ring shows the increased azimuthal disorder of the $MoSe_2$ layer with respect to the h-BN layer. b) Polar and azimuthal cuts performed on the LEED image for further processing. In red: Polar and azimuthal cuts through the principal spots of h-BN and $MoSe_2$ diffraction rings. In blue: Azimuthal cuts performed to subtract the LEED image background from the cut through principal spots. In green and yellow: cuts performed to determine the lattice constant of h-BN and $MoSe_2$. In c) lattice constant determination: The calculation was gauged to the known lattice constant and next neighbour distance of h-BN in the green and red colored linear cuts. The lattice constant of the $MoSe_2$ is found to be $a_{MoSe_2} = 3.3$ Å.

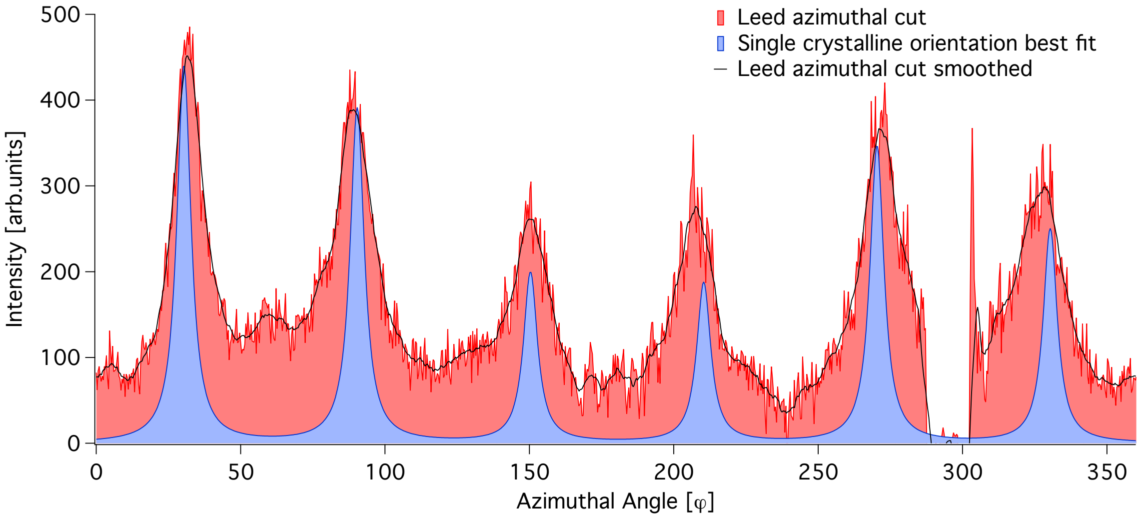

Figure 5.7 In red the normalised azimuthal cut data from figure 5.6 on the $MoSe_2$ diffraction ring. In black the smoothed data for better visualisation. In blue the fit with six Lorentzian lineshapes with fixed width. The width was chosen to be the same as the width found in the fit of the polar cut through the $MoSe_2$ ring (not shown). The data shows that $I_{ord}/I_{tot} = 42$ % of the $MoSe_2$ structure follows the registry of the h-BN.

In order to verify the finding shown in figure 5.6 XPD measurements were performed. The measurements are shown with two different types of normalisation to account for the advantages and disadvantages of the respective procedures. Additionally, a 3-fold average was performed, as the analysed structures have a C_3 fold symmetry. Both normalisations allow to display the stereographic projection in a manner to magnify the features arising from the scattering processes. With the first normalisation a 2D Gaussian function ($\propto \exp(-(\theta/\theta_0)^2)$) is subtracted from the 2D projection, for this reason the count rate after this particular procedure may be negative in certain regions. This allows to resolve ring structures which, centered at $\theta = 0°$ may indicate azimuthal disorder. On the other side a phi average normalisation is chosen, where the single pixels lying on a common azimuthal ring θ =constant are normalized by the average value of the ring. This allows to highlight features but will eliminate centered ring features, which also includes forward scattering along the surface normal. The phi average highlights how pronounced features are with respect to the background, as the phi average normalisation results in values centered around unity. This is also called the *anisotropy*.

The intensities of the Mo3d$_{5/2}$, Se3p$_{3/2}$, Rh3d$_{5/2}$, and $N1s$ lines were recorded over polar emission angles θ from 0° and 82° and the full $\varphi = 360$ azimuthal angles, which is 86% of the 2π hemisphere over the sample. The result is shown in figure 5.8, where subfigures a) and b) represent the Mo3d$_{5/2}$ stereographic projection plots with a Gaussian background subtraction and a phi average normalisation respectively. The pattern show a distinct six-fold symmetry which arises from the crystalline MoSe$_2$ layer. In the center of the plot, a forward scatterer is clearly visible, indicating the presence of at least a second layer of MoSe$_2$ and confirming the result from quantitative XPS analysis. In the same manner as in the LEED image, also the XPD shows ring structures, indicating non-perfect crystalline growth of the MoSe$_2$. In subfigures 5.8 c) and d) the stereographic projection plot of the Se3p$_{3/2}$ line are shown with Gaussian background subtraction and phi average normalisation respectively. Analogous to the case of Mo the plot shows a six-fold symmetry and a forward scatterer, which on contrary to the molybdenum XPD forward scatterer can be expected also for the single layer case. The rotation rings are more pronounced in the case of Se.

In order to confirm the common growth direction of MoSe$_2$ and h-BN in figure 5.9 the azimuthal position of the scattering features in the XPD plots of the Mo3d$_{5/2}$ and Se3p$_{3/2}$ are compared to the Rh3d$_{5/2}$ and N1s. For the Rh3d$_{5/2}$ the $(\bar{2}11)$ direction is known from the literature [125]. Starting from this known direction in the stereographic plot for a face-centered cubic crystal, polar and azimuthal cuts are performed to compare the azimuthal angle of the main scattering directions of the three crystalline structures. In the subfigure 5.9 a) the common crystalline orientation of the Rh(111), the h-BN and the MoSe$_2$ is visible in the XPD plots. In 5.9 b) the anisotropy found in the circular cuts through the XPD patterns is plotted versus the azimuthal angle. The anisotropy

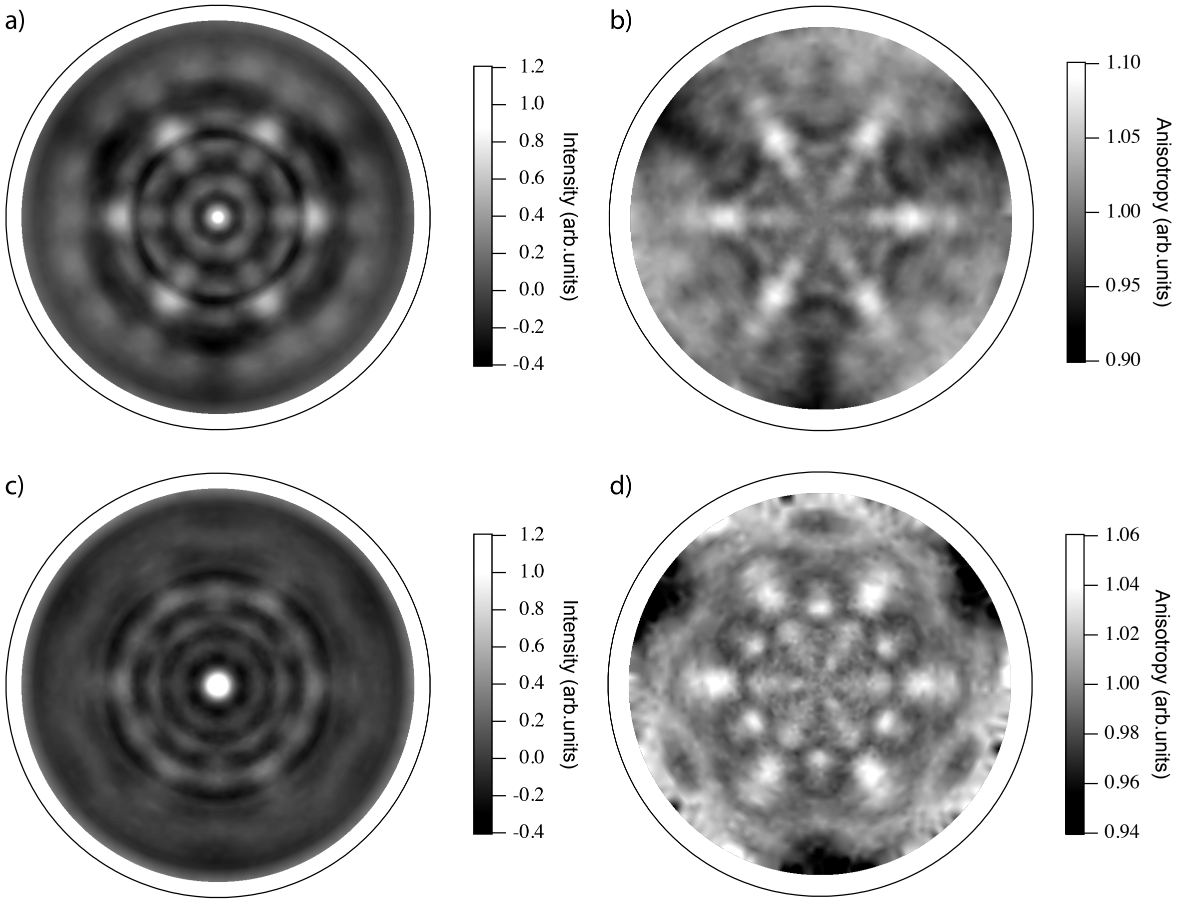

Figure 5.8 XPD of the $MoSe_2/h$-BN heterostructure for selected elements. Top row: XPD patterns of the $Mo3d_{3/2}$ line at a kinetic energy of E_{kin} = 1019.3 eV in a) displayed with a Gaussian background subtraction and in b) with a phi averaged normalisation. The patterns show a distinct six-fold structure in both cases arising from the ordered Mo layer. The central forward scatterer (visible only in a) because of normalisation reasons) suggests the $MoSe_2$ to be at least partially double layered. The ring structure suggests partial azimuthal disorder as seen in the LEED measurement in figure 5.6 Lower row: XPD patterns of the $Se3p_{3/2}$ line at a kinetic energy of E_{kin} = 1191.9 eV in c) displayed with Gaussian background subtraction and in d) with phi averaged normalisation. Analogously to the Mo case the Se displays a similar six-fold symmetric diffraction pattern and a ring structure.

is, in this case, defined as the ratio between the value of a measurement point on the azimuthal ring divided by the average of the values on the ring (I_i/I_{avg}). The plot shows that the features of the three structures have a high correlation with a periodicity of 60° and a less pronounced correlation in a 30° shifted phase. The 120° periodicity instead arises form the 3-fold averaging of the data. The forward scattering directions of the $MoSe_2$ layer diffraction patterns follow the same direction as the *h*-BN diffraction patterns, which is an indication that the $MoSe_2$ follows the *h*-BN substrate crystalline orientation.

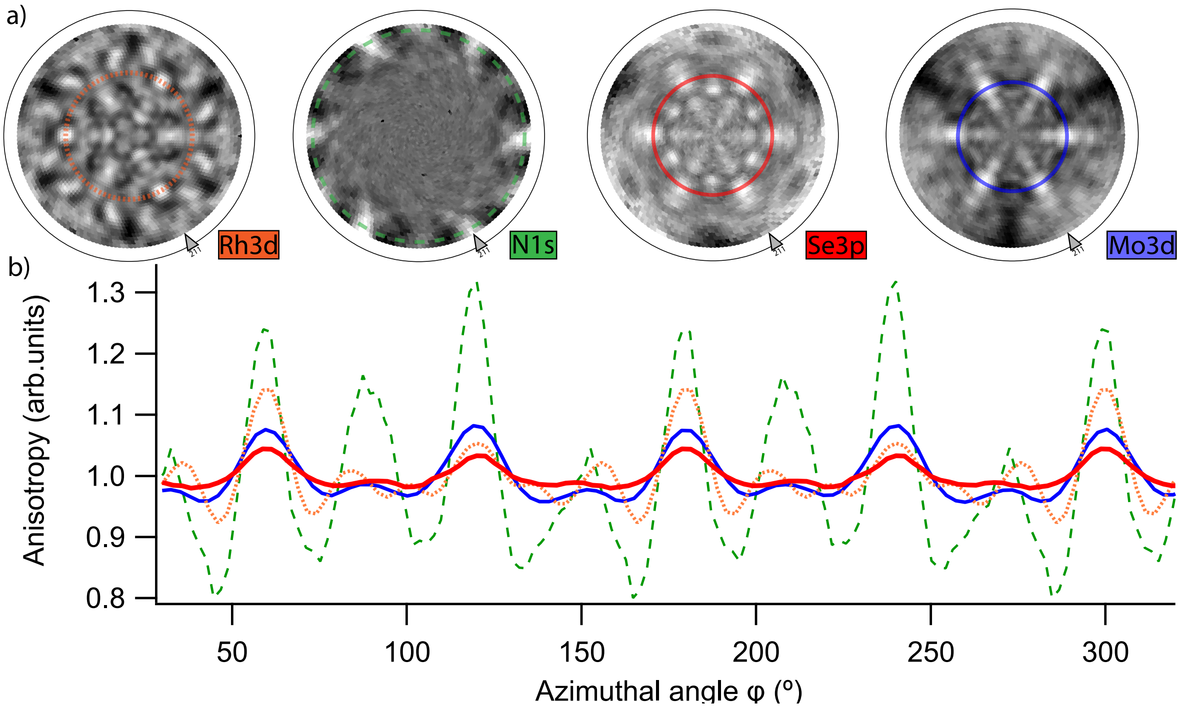

Figure 5.9 Top row a) XPD patterns of the Rh3d, N1s, Se3p, Mo3d structure. The $(\bar{2}11)$ is marked through a triangle on the XPD plot outer region. The rings of different colors plotted on the XPD patterns show the location of the azimuthal cuts through the XPD patterns shown in the subfigure b). These plots show the anisotropy of the XPD patterns along the circular cuts. The anisotropy is plotted versus the azimuthal angle. As the forward scattering directions of the $MoSe_2$ layer diffraction patterns follow the same direction as the *h*-BN layer and the Rh(111) substrate crystalline orientation. The azimuthal cuts also show a 120° which arises from the 3-fold averaging of the data.

As a concluding step to confirm the crystalline structure of $MoSe_2$ on *h*-BN Electron Diffraction in Atomic Cluster (EDAC) calculations were performed [58]. As a cluster, we took a 2H $MoSe_2$ structure with two layers as shown in figure 5.1. The calculation results are shown in the top halves of figure 5.10, where subfigure a) shows the case of Mo and subfigure b) the case of Se. In the bottom halves the corresponding experimental measurements are shown. The structure obtained in the simulations fit the structure of the experiment to a high degree, confirming the presence of crystalline, ordered $MoSe_2$ on *h*-BN.

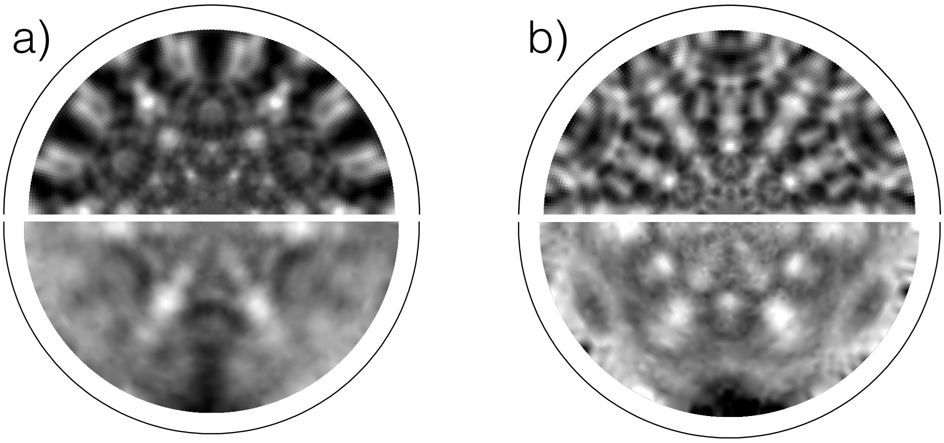

Figure 5.10 Comparison between EDAC calculation (top halves of the patterns) and experimental data (bottom halves of the patterns) for a) Mo3d and for b) Se3p emitters. The simulations are consistent with the experimental data and show a comparable structure for the Mo3d and the Se3p case.

5.4 Exfoliation

As described in the introduction of this chapter, $MoSe_2$ is particular because of the optically active properties of the single layer material. Albeit, to investigate the luminescence properties of $MoSe_2$/*h*-BN, the layers need to be transferred on a non-metallic substrate. This is necessary in order to quench the electron-hole pair recombination which is facilitated by the presence of the metal substrate in the vicinity of the optically active material. The $MoSe_2$/*h*-BN layer was electrochemically delaminated from the Rh(111) growth substrate. The method is described in publication [94] and in chapter

2, consisting of a Tetraoctylammoniabromide pre-treatment and subsequent delamination in an electrochemical wet cell. The $MoSe_2/h$-BN layer was transferred to a 90 nm thick SiO_2 on p-doped Si(111) substrate.

To investigate whether the delamination process is successful a comparison between the XPS spectra before (pristine) and after (transferred) the delamination process is the most sensitive measurement method. The direct comparison between the XPS intensities for the element x prior (I_p^x) and after delamination (I_t^x) can be taken as the transfer ratio T:

$$T^x = \frac{I_t^x}{I_p^x} \tag{5.22}$$

For simplicity, only the spectra for the boron and selenium were taken for this calculation. The boron transfer ratio T^B will be a value for the transfer success of h-BN while the selenium transfer ratio T^{Se} for the $MoSe_2$. In figure 5.11 the spectra for boron in the pristine a) and transferred b) state are shown. The same is shown for selenium in the pristine c) and transferred d) state. The red circles represent the data, the blue line the fitting result using Gaussian line shapes and in black the fitting curve for the single subshells with the peak energy positions. The pristine and transferred graphs are plotted with the same scale in order to show the signal difference before and after the transfer. In both the boron and the selenium case the peak energies show a shift due to the different substrate [94]. The transfer ratios can be calculated using the areas of the fitted peaks. The so calculated ratios are for boron $T^B = 0.44$ and for Selenium $T^{Se} = 0.1$. The transfer ratio for the h-BN are higher compared to the $MoSe_2$ and shows that the transfer procedure was less optimal for the $MoSe_2$ material. The atomic ratio between Mo and Se on the transferred sample is $R = 1.45$ selenium atoms per molybdenum atoms, which is similar to the ratio obtained before delamination ($R = 1.4$) shown in figure 5.5 indicating a selenium deficit in the $MoSe_2$.

The delaminated $MoSe_2$/*h*-BN/SiO_2 were also analysed by XPD to investigate the structure. In figure 5.12 the XPD stereographic projections of the a) N1s, b) Mo3d and c) Se3p elastic lines are shown, all with phi average normalisation. While clearly, the structure of the *h*-BN remains intact during transfer, the $MoSe_2$ structure seems more affected showing great azimuthal disorder compared to the sample in figure 5.8. The six-fold symmetric anisotropy is still visible confirming the presence of a certain amount of crystalline ordered $MoSe_2$. The disorder may be an effect of the transfer procedure where the $MoSe_2$ following the crystalline registry of the *h*-BN and the Rh(111) substrate resists delamination due to stronger bonding to the substrate.

5.5 Discussion

In this chapter, the growth and structure of $MoSe_2$ on *h*-BN/Rh(111) Sinergia thin films was studied. The XPS data (figure 5.3, 5.2 and 5.5) confirm the growth of at least a few layer structure of $MoSe_2$ on the *h*-BN/Rh(111) film, showing the feasibility of transition metal dichalcogenide (TMDC) growth on *h*-BN Sinergia thin films. The *h*-BN layer remains intact during the growth process and the $MoSe_2$ layer grows in a partially crystalline structure (figure 5.6) resulting in $I_{ord}/I_{tot} = 42$ % of ordered material. In addition XPD analysis of the $MoSe_2$ and comparison to the substrate XPD show a link between the preferred growth directions of $MoSe_2$ (figures 5.8 and 5.9) and *h*-BN. The $MoSe_2$ structure could successfully be simulated with EDAC confirming the crystalline structure of the 2H $MoSe_2$. Furthermore figure 5.11 and 5.12 demonstrate the feasibility of $MoSe_2$/*h*-BN delamination for further electronic application, albeit further research on an optimized transfer procedure has to be carried out.

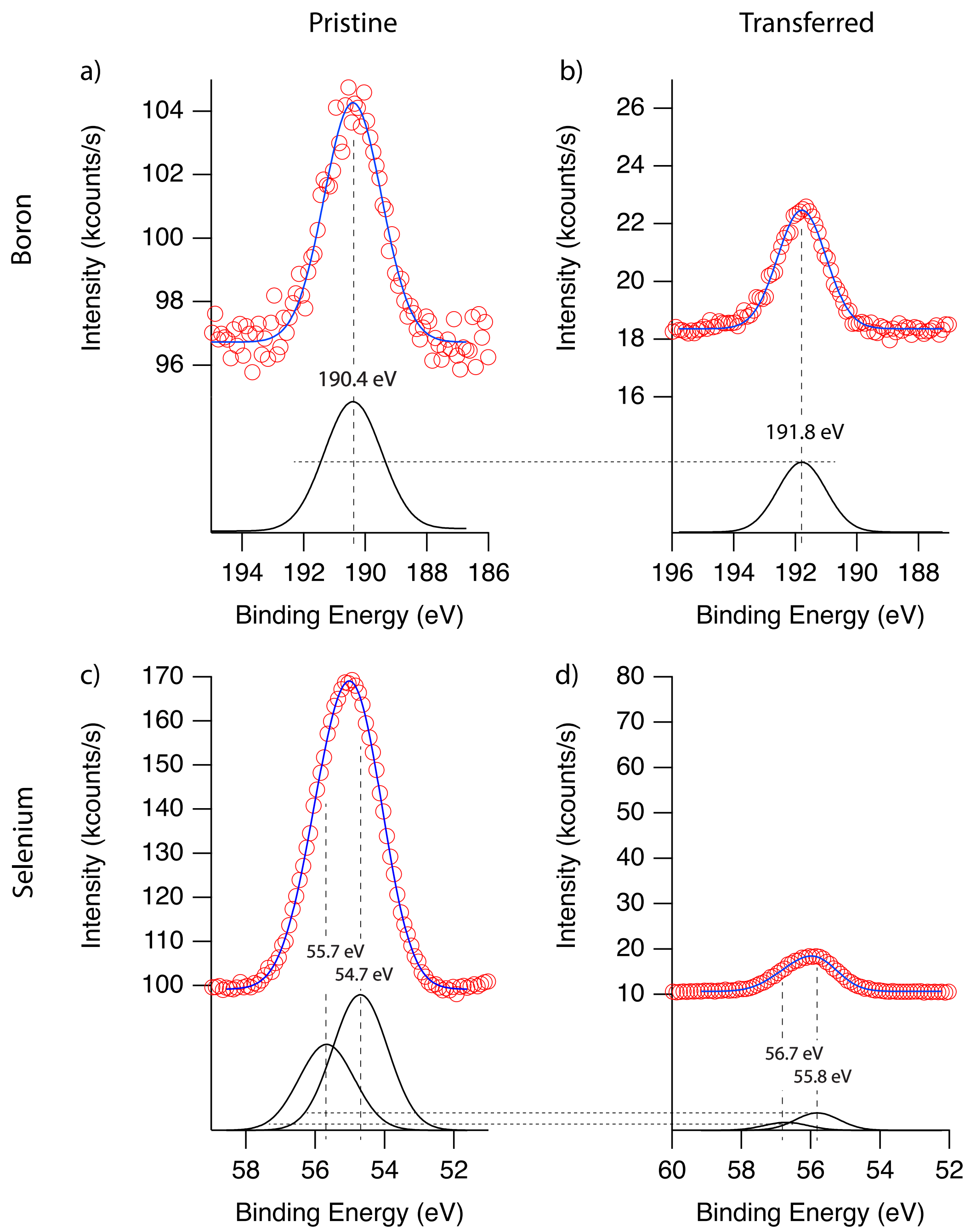

Figure 5.11 XPS data comparing a) B1s pristine, b) B1s transferred, c) Se3d pristine and d) Se3d transferred. The peaks were fitted with Gaussian line shapes. The energy shifts of the peaks are due to the insulating SiO_2 substrate which can generate charging effects. The peak areas are used to calculate the transfer ratio of the $MoSe_2$ and the *h*-BN from the Rh(111) to the SiO_2 substrate. The resulting transfer rates are $T^B = 0.44$ for the *h*-BN and $T^{Se} = 0.1$ for the $MoSe_2$ layer.

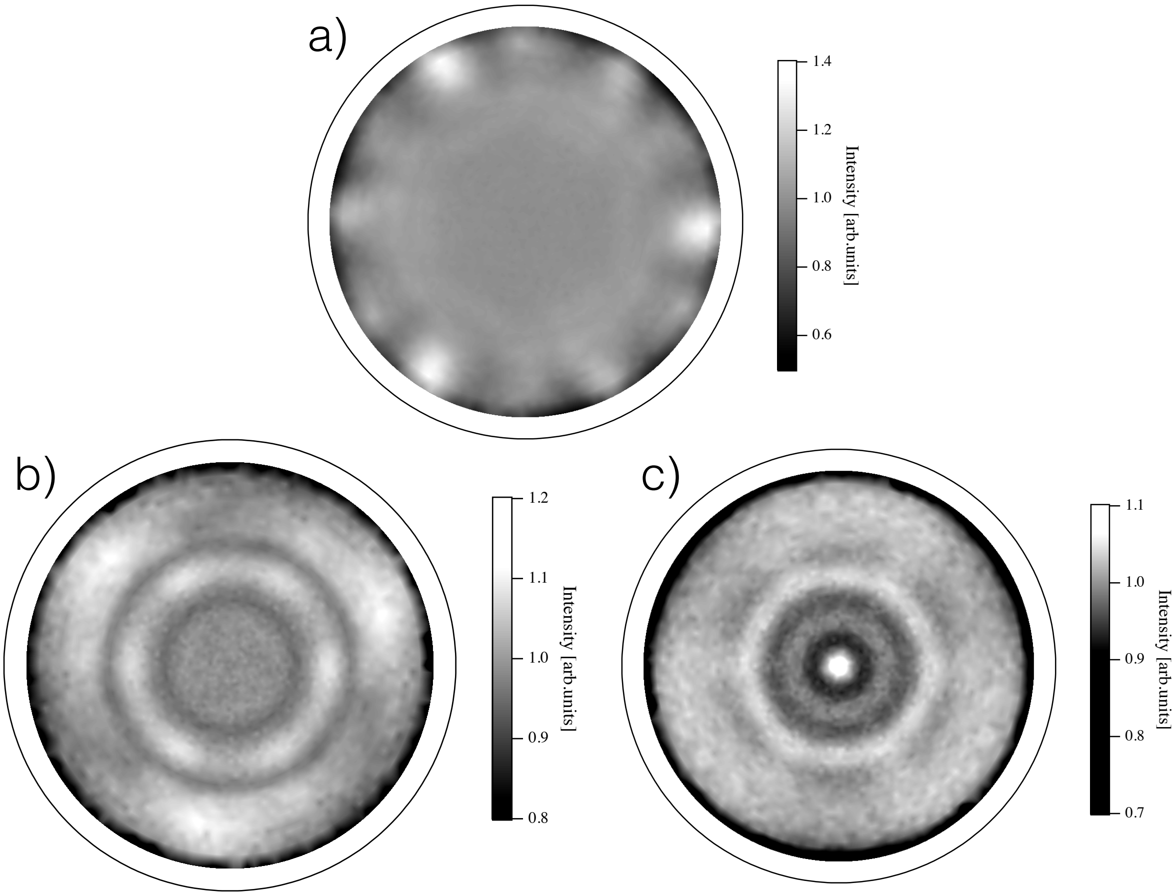

Figure 5.12 XPD patterns of a $MoSe_2$/*h*-BN after electrochemical delamination. a) N1s structure showing the well known three-fold symmetric pattern of *h*-BN, showing the transferred material remains crystalline to a certain degree. b) and c) Mo3d and Se3p XPD patterns respectively. The six-fold symmetric patterns are still recognisable, albeit the crystallinity shows less pronounced than in the case of $MoSe_2$/*h*-BN/Rh(111).

The growth of TMDC on Sinergia thin films hints to the possibility for large-scale growth. As a first step, the growth of $MoSe_2/h$-BN on a 4-inch Rh(111) wafer should be attempted. The availability of a large number of inexpensive samples allows for further studies and designs, particularly for the application of valleytronics [138]. Further progress is needed to better understand the delamination process as wet transfer methods potentially limit the electronic properties of the samples [98]. On the other hand $MoSe_2$ is not the only TMDC which shows interesting properties, for this reason, a study of other dichalcogenide material growth on h-BN/Rh(111) films should be performed and studied [139].

6 Conclusions and Outlook

6.1 Conclusions

In this thesis, growth and transfer two-dimensional materials have been studied and achieved. On 4-inch wafers graphene and *h*-BN were grown successfully. The grown layers showed to have a high crystallinity over the whole wafer and supplied the research and testing phase for the delamination and transfer of the layers. The TOA-Br assisted electrochemical delamination process is a successful transfer method for graphene and *h*-BN. It enabled, in a first step, the option to build simple graphene on SiO_2 samples which were studied by angle-resolved photoelectron spectroscopy [94], and supplied samples for collaborative projects [140], [141].

The delamination technique also allowed to construct layer by layer heterostructured samples as described in chapter 3. The so produced samples were analysed by XPS and ARPES measurements. The XPS results in figure 3.11 show the presence of both graphene and *h*-BN on the SiO_2 substrate. The momentum distribution plots at the Fermi surface and ARPES measurements clearly show six-fold symmetric intensity modulations at the K points of the Brillouin zone 3.12 which can be attributed to the Dirac cones of the graphene. The Dirac cones display an aimed rotation of 40°, demonstrating the successful arrangement of the graphene with respect to the *h*-BN. The sheet resistivity and charge carrier mobility was measured for the two heterostructured samples and compared to graphene transferred from sinergia iridium films and polycrystalline copper foils, as shown in figure 3.13. The transport properties resulted severely limited with respect to the non-heterostructured samples, which may indicate a limitation of the electrochemical transfer method. In fact, transport measurement on various samples suggests a reduction in transport characteristics especially for the TOA-Br treated samples, albeit, a conclusive statement cannot be given due to the limited sample “population “.

In a second step the direct growth of a g/h-BN/Rh(111) heterostructure on a full 4-inch sinergia wafer described in chapter 4 was achieved. *h*-BN was grown in a first step using CVD in the ultrahigh vacuum regime. Subsequently, a millibar CVD exposure with a carbon-rich precursor molecule was carried out to enable the growth of the graphene layer on the *h*-BN.

The grown heterostructures were analysed by spectroscopic methods and subsequently transferred on SiO_2 substrates. This transfer enabled us to observe the grown heterostructures by optical microscopy, as shown in figure 4.1. The figures suggest a concentric growth of graphene starting from numerous growth locations. Raman spectroscopy performed on circular areas, as shown in figure 4.2, confirm the presence of graphene and graphitic structures on the sample visible in the shape of the 2D Raman mode. The graphite contribution is expected from the non-self terminating process during high-pressure millibar growth environment. Equally, the high D mode suggests disordered graphene on the surface and is expected for the same reason.

From this knowledge, scanning tunnelling microscopy was performed on the untransferred sample, as shown in figure 4.3, in an attempt to find evidence for heterostructure growth. A lateral heterostructure junction was found, and the junction area was analysed. No evidence for vertical heterostructures was found using scanning tunnelling microscopy, which does not exclude the coexistence of vertical and horizontal heterostructure phases. In a last step, the photoemission spectra and diffraction patterns of the transferred and untransferred samples were compared. Figure 4.4 and 4.5 show the presence of the *h*-BN components on the untransferred and transferred sample while the components of the graphene, namely the C1s contribution, is split into three distinct peaks. Using photoelectron diffraction, it was possible to assign the origin to the three peaks.

The measurements suggest a lateral arrangement of the heterostructure as summarised in figure 4.6, where the high-pressure environment, during the millibar CVD exposure, allows carbon atoms to substitute the *h*-BN layer, forming *h*-BN - graphene lateral junctions on the sample.

$MoSe_2$/*h*-BN heterostructure growth on rhodium sinergia films was achieved as described in chapter 5. In a collaboration project, rhodium sinergia films were treated with molecular beam epitaxy to grow a dichalcogenide - *h*-BN heterostructure.

The heterostructure was analysed by photoemission spectroscopy as shown in figure 5.2 and 5.3. From the XPS intensities the thickness of the $MoSe_2$ layer on *h*-BN was calculated, showing the presence of 2-3 monolayers of $MoSe_2$ in respect to *h*-BN. The structure of the $MoSe_2$/*h*-BN sample was analysed by low energy electron diffraction and photoelectron diffraction, shown in figures 5.6 and 5.8, where the amount of crystalline $MoSe_2$ was estimated to be 42% of the total.

Delamination of the $MoSe_2$/*h*-BN to a SiO_2 heterostructure substrate was possible with a transfer ratio of 0.1 for the selenium compared to the 0.44 for the boron. Regardless of the loss of selenium during transfer, Raman spectroscopy and luminescence of the transferred $MoSe_2$ was observed and published in a peer-reviewed journal [34].

6.2 Outlook

Growth and transfer of two-dimensional heterostructures will remain a central topic for its potential in technology application. For computers, the fulfillment of Moore's law, which postulates the doubling of the number of transistors per chip every two years [142], development of two-dimensional heterostructured materials may span the growing effects of quantum mechanics in miniaturisation of silicon-based field effect transistors.

In this thesis, the growth of g/h-BN/Rh(111) and $MoSe_2/h$-BN heterostructures was demonstrated on a rhodium wafer based substrate. The option to synthesise such heterostructures on different metal substrates remains open. Copper thin film sinergia wafers represent a possible choice for further experiments on the heterostructure growth. Indeed, copper substrates were already used for successful vertical heterostructure growth [24] and the copper facilitates the delamination of the grown structures, as the coupling of graphene and h-BN to copper is weaker compared to the case of rhodium. TOA-Br assisted electrochemical delamination is suspected to be a cause for reduced transport characteristics in the transferred samples [92]. The use of copper substrates may eliminate the necessity of the TOA-Br pretreatment.

Another option is the synthesis of $MoSe_2$ or other diverse dichalcogenide species on a full 4-inch wafer to study these materials on highly abundant sample availability. The option to transfer the grown structures on SiO_2 opens the experiment to new measurement techniques which, when compared to the measurements of the untransferred samples, may be valuable sources of new insights.

Bibliography

[1] H. P. Boehm, A. Clauss, G. O. Fischer, and U. Hofmann, *Das Adsorptionsverhalten sehr dünner Kohlenstoff-Folien*, Zeitschrift für anorganische und allgemeine Chemie **316**, 119–127.

[2] H. Boehm, R. Setton, and E. Stumpp, *Nomenclature and terminology of graphite intercalation compounds*, Carbon **24**, 241 – 245 (1986).

[3] A. K. Geim, *Graphene prehistory*, Physica Scripta **2012**, 014003 (2012).

[4] P. Blake, E. W. Hill, A. H. Castro Neto, K. S. Novoselov, D. Jiang, R. Yang, T. J. Booth, and A. K. Geim, *Making graphene visible*, Applied Physics Letters **91**, 063124 (2007).

[5] K. S. Novoselov, A. K. Geim, S. V. Morozov, D. Jiang, Y. Zhang, S. V. Dubonos, I. V. Grigorieva, and A. A. Firsov, *Electric Field Effect in Atomically Thin Carbon Films*, Science **306**, 666–669 (2004).

[6] A. H. Castro Neto, F. Guinea, N. M. R. Peres, K. S. Novoselov, and A. K. Geim, *The electronic properties of graphene*, Rev. Mod. Phys. **81**, 109–162 (2009).

[7] Y.-M. Lin, C. Dimitrakopoulos, K. A. Jenkins, D. B. Farmer, H.-Y. Chiu, A. Grill, and P. Avouris, *100-GHz Transistors from Wafer-Scale Epitaxial Graphene*, Science **327**, 662–662 (2010).

[8] X. Li, X. Wang, L. Zhang, S. Lee, and H. Dai, *Chemically Derived, Ultrasmooth Graphene Nanoribbon Semiconductors*, Science **319**, 1229–1232 (2008).

[9] D. R., Y. F., MericI., LeeC., WangL., SorgenfreiS., WatanabeK., TaniguchiT., KimP., S. L., and HoneJ., *Boron nitride substrates for high-quality graphene electronics*, Nat Nano **5**, 722–726 (2010).

[10] K. S. Novoselov, V. I. Fal'ko, L. Colombo, P. R. Gellert, M. G. Schwab, and K. Kim, *A roadmap for graphene*, Nature **490**, 192 EP – (2012), review Article.

[11] J. Coraux, A. T. N'Diaye, C. Busse, and T. Michely, *Structural Coherency of Graphene on Ir(111)*, Nano Letters **8**, 565–570 (2008), pMID: 18189442.

[12] X. Li, W. Cai, J. An, S. Kim, J. Nah, D. Yang, R. Piner, A. Velamakanni, I. Jung, E. Tutuc, S. K. Banerjee, L. Colombo, and R. S. Ruoff, *Large-Area Synthesis of High-Quality and Uniform Graphene Films on Copper Foils*, Science **324**, 1312–1314 (2009).

[13] S. Roth, J. Osterwalder, and T. Greber, *Synthesis of epitaxial graphene on rhodium from 3-pentanone*, Surface Science **605**, L17 – L19 (2011).

[14] A. Nagashima, N. Tejima, Y. Gamou, T. Kawai, and C. Oshima, *Electronic structure of monolayer hexagonal boron nitride physisorbed on metal surfaces*, Physical Review Letters **75**, 3918–3921 (1995).

[15] T. Greber, L. Brandenberger, M. Corso, A. Tamai, and J. Osterwalder, *Single layer hexagonal boron nitride films on Ni(110)*, e-Journal of Surface Science and Nanotechnology **4**, 410–413 (2006).

[16] M. Corso, *Boron nitride nanostructures on transition metals: flat layers and nanomesh*, Ph.D. thesis, University of Zurich (2006).

[17] L. Gao, W. Ren, H. Xu, L. Jin, Z. Wang, T. Ma, L.-P. Ma, Z. Zhang, Q. Fu, L.-M. Peng, X. Bao, and H.-M. Cheng, *Repeated growth and bubbling transfer of graphene with millimetre-size single-crystal grains using platinum*, Nature Communications **3**, 699 EP – (2012), article.

[18] Y. Wang, Y. Zheng, X. Xu, E. Dubuisson, Q. Bao, J. Lu, and K. P. Loh, *Electrochemical Delamination of CVD-Grown Graphene Film: Toward the Recyclable Use of Copper Catalyst*, ACS Nano **5**, 9927–9933 (2011), pMID: 22034835.

[19] M. S. Bresnehan, M. J. Hollander, M. Wetherington, M. LaBella, K. A. Trumbull, R. Cavalero, D. W. Snyder, and J. A. Robinson, *Integration of Hexagonal Boron Nitride with Quasi-freestanding Epitaxial Graphene: Toward Wafer-Scale, High-Performance Devices*, ACS Nano **6**, 5234–5241 (2012), pMID: 22545808.

[20] G. Kim, A.-R. Jang, H. Y. Jeong, Z. Lee, D. J. Kang, and H. S. Shin, *Growth of High-Crystalline, Single-Layer Hexagonal Boron Nitride on Recyclable Platinum Foil*, Nano Letters **13**, 1834–1839 (2013), pMID: 23527543.

[21] K. K. Kim, A. Hsu, X. Jia, S. M. Kim, Y. Shi, M. Dresselhaus, T. Palacios, and J. Kong, *Synthesis and Characterization of Hexagonal Boron Nitride Film as a Dielectric Layer for Graphene Devices*, ACS Nano **6**, 8583–8590 (2012), pMID: 22970651.

[22] M. Yankowitz, J. Xue, D. Cormode, J. D. Sanchez-Yamagishi, K. Watanabe, T. Taniguchi, P. Jarillo-Herrero, P. Jacquod, and B. J. LeRoy, *Emergence of superlattice Dirac points in graphene on hexagonal boron nitride*, Nature Physics **8**, 382 EP – (2012).

[23] Y. Qian, H. Van Ngoc, and D. J. Kang, *Growth of Graphene/h-BN Heterostruc-*

tures on Recyclable Pt Foils by One-Batch Chemical Vapor Deposition, Scientific Reports **7**, 17083 (2017).

[24] S. Roth, F. Matsui, T. Greber, and J. Osterwalder, *Chemical Vapor Deposition and Characterization of Aligned and Incommensurate Graphene/Hexagonal Boron Nitride Heterostack on Cu(111)*, Nano Letters **13**, 2668–2675 (2013).

[25] G. H. Han, J. A. Rodriguez-Manzo, C.-W. Lee, N. J. Kybert, M. B. Lerner, Z. J. Qi, E. N. Dattoli, A. M. Rappe, M. Drndic, and A. T. C. Johnson, *Continuous Growth of Hexagonal Graphene and Boron Nitride In-Plane Heterostructures by Atmospheric Pressure Chemical Vapor Deposition*, ACS Nano **7**, 10129–10138 (2013), pMID: 24182310.

[26] P. Sutter, R. Cortes, J. Lahiri, and E. Sutter, *Interface Formation in Monolayer Graphene-Boron Nitride Heterostructures*, Nano Letters **12**, 4869–4874 (2012).

[27] Z. Liu, L. Ma, G. Shi, W. Zhou, Y. Gong, S. Lei, X. Yang, J. Zhang, J. Yu, K. P. Hackenberg, A. Babakhani, J.-C. Idrobo, R. Vajtai, J. Lou, and P. M. Ajayan, *In-plane heterostructures of graphene and hexagonal boron nitride with controlled domain sizes*, Nature Nanotechnology **8**, 119 EP – (2013).

[28] L. Britnell, R. V. Gorbachev, R. Jalil, B. D. Belle, F. Schedin, A. Mishchenko, T. Georgiou, M. I. Katsnelson, L. Eaves, S. V. Morozov, N. M. R. Peres, J. Leist, A. K. Geim, K. S. Novoselov, and L. A. Ponomarenko, *Field-Effect Tunneling Transistor Based on Vertical Graphene Heterostructures*, Science **335**, 947–950 (2012).

[29] M. P. Levendorf, C.-J. Kim, L. Brown, P. Y. Huang, R. W. Havener, D. A. Muller, and J. Park, *Graphene and boron nitride lateral heterostructures for atomically thin circuitry*, Nature **488**, 627 EP – (2012).

[30] H. Adrian, B. Carlo, C. Huanyao, R. Silvan, K. Martin, K. Thomas, W. M. G. Stefan, S. Matthias, O. Jürg, and G. Thomas, *High quality single atomic layer deposition of hexagonal boron nitride on single crystalline Rh(111) four-inch wafers*, Review of Scientific Instruments **85**, 035101 (2014).

[31] S. Grandthyll, S. Gsell, M. Weinl, M. Schreck, S. Hüfner, and F. Müller, *Epitaxial growth of graphene on transition metal surfaces: chemical vapor deposition versus liquid phase deposition*, Journal of Physics: Condensed Matter **24**, 314204 (2012).

[32] L. Koefoed, M. Kongsfelt, S. r. Ulstrup, A. G. s. c. ˘ Cabo, A. Cassidy, P. R. Whelan, M. Bianchi, M. Dendzik, F. Pizzocchero, B. Jø rgensen, P. Bø ggild, L. Hornekæ r, P. Hofmann, S. U. Pedersen, and K. Daasbjerg, *Facile electrochemical transfer of large-area single crystal epitaxial graphene from Ir(1 1 1)*, Journal of Physics D: Applied Physics **48** (2015), 10.1088/0022-3727/48/11/115306.

[33] S. Roth, T. Greber, and J. Osterwalder, *Some Like It Flat: Decoupled h-BN Monolayer Substrates for Aligned Graphene Growth*, ACS Nano **10**, 11187–11195 (2016).

[34] M.-W. Chen, H. Kim, C. Bernard, M. Pizzochero, J. Zaldıivar, J. I. Pascual, M. M. Ugeda, O. V. Yazyev, T. Greber, J. Osterwalder, O. Renault, and A. Kis, *Electronic Properties of Transferable Atomically Thin MoSe2/h-BN Heterostructures Grown on Rh(111)*, ACS Nano 10.1021/acsnano.8b05628, pMID: 30371049.

[35] T. Greber, O. Raetzo, T. J. Kreutz, P. Schwaller, W. Deichmann, E. Wetli, and J. Osterwalder, *A photoelectron spectrometer for k-space mapping above the Fermi level*, Review of Scientific Instruments **68**, 4549–4554 (1997).

[36] A. Reina, X. Jia, J. Ho, D. Nezich, H. Son, V. Bulovic, M. S. Dresselhaus, and

J. Kong, *Large Area, Few-Layer Graphene Films on Arbitrary Substrates by Chemical Vapor Deposition*, Nano Letters **9**, 30–35 (2009), pMID: 19046078.

[37] Y. Lee, S. Bae, H. Jang, S. Jang, S.-E. Zhu, S. H. Sim, Y. I. Song, B. H. Hong, and J.-H. Ahn, *Wafer-Scale Synthesis and Transfer of Graphene Films*, Nano Letters **10**, 490–493 (2010), pMID: 20044841.

[38] K. K. Kim, A. Hsu, X. Jia, S. M. Kim, Y. Shi, M. Hofmann, D. Nezich, J. F. Rodriguez-Nieva, M. Dresselhaus, T. Palacios, and J. Kong, *Synthesis of Monolayer Hexagonal Boron Nitride on Cu Foil Using Chemical Vapor Deposition*, Nano Letters **12**, 161–166 (2012), pMID: 22111957.

[39] P. O. C. Database, *Borazine* (2018).

[40] N. C. WebBook, *Ethylene* (2018).

[41] N. C. WebBook, *3-Pentanone* (2018).

[42] E. W. Leib, U. Vainio, R. M. Pasquarelli, J. Kus, C. Czaschke, N. Walter, R. Janssen, M. Müller, A. Schreyer, H. Weller, and T. Vossmeyer, *Synthesis and thermal stability of zirconia and yttria-stabilized zirconia microspheres*, Journal of Colloid and Interface Science **448**, 582 – 592 (2015).

[43] M. Fischer, S. Gsell, M. Schreck, R. Brescia, and B. Stritzker, *Preparation of 4-inch Ir/YSZ/Si(001) substrates for the large-area deposition of single-crystal diamond*, Diamond and Related Materials **17**, 1035 – 1038 (2008), proceedings of Diamond 2007, the 18th European Conference on Diamond, Diamond-Like Materials, Carbon Nanotubes, Nitrides and Silicon Carbide.

[44] S. Gsell, M. Fischer, M. Schreck, and B. Stritzker, *Epitaxial films of metals from the platinum group (Ir, Rh, Pt and Ru) on YSZ-buffered Si(111)*, Journal of Crystal Growth **311**, 3731 – 3736 (2009).

[45] M. Paffett, R. Simonson, P. Papin, and R. Paine, *Borazine adsorption and decomposition at Pt(111) and Ru(001) surfaces*, Surface Science **232**, 286 – 296 (1990).

[46] C. Oshima and A. Nagashima, *Ultra-thin epitaxial films of graphite and hexagonal boron nitride on solid surfaces*, Journal of Physics: Condensed Matter **9**, 1 (1997).

[47] L. DE BROGLIE, *Waves and Quanta*, Nature **112**, 540 EP – (1923).

[48] H. Hertz, *Ueber einen Einfluss des ultravioletten Lichtes auf die electrische Entladung*, Annalen der Physik **267**, 983–1000.

[49] A. Einstein, *Über einen die Erzeugung und Verwandlung des Lichtes betreffenden heuristischen Gesichtspunkt*, Annalen der Physik **322**, 132–148.

[50] H. Stefan, *Photoelectron Spectroscopy* (Springer, 1996).

[51] J. Osterwalder, *Surface and Interface Science* (Wiley, 2012).

[52] R. Steinhardt and E. Serfass, *X-Ray Photoelectron Spectrometer for Chemical Analysis*, Analytical Chemistry **23**, 1585–1590 (1951).

[53] U. Gelius, E. Basilier, S. Svensson, T. Bergmark, and K. Siegbahn, *A high resolution ESCA instrument with X-ray monochromator for gases and solids*, Journal of Electron Spectroscopy and Related Phenomena **2**, 405 – 434 (1973).

[54] J. F. Moulder, W. F. Stickle, P. E. Sobol, and K. D. Bomben, *Handbook of X-ray Photoelectron Spectroscopy* (Physical Electronics Division, Perkin-Elmer Corporation, 1992).

[55] *NIST Electron Inelastic-Mean-Free-Path Database - Version1.2* (National Institute of Standards and Technology, 2010).

[56] J. Osterwalder, T. Greber, A. Stuck, and L. Schlapbach, *Experimental full-solid-angle substrate photoelectron-diffraction data at 1-keV energies: Implications for photoelectron holography*, Phys. Rev. B **44**, 13764–13767 (1991).

[57] T. Greber, J. Wider, E. Wetli, and J. Osterwalder, *X-Ray Photoelectron Diffraction in the Backscattering Geometry: A Key to Adsorption Sites and Bond Lengths at Surfaces*, Phys. Rev. Lett. **81**, 1654–1657 (1998).

[58] F. J. García de Abajo, M. A. Van Hove, and C. S. Fadley, *Multiple scattering of electrons in solids and molecules: A cluster-model approach*, Phys. Rev. B **63**, 075404 (2001).

[59] M. Kralj, I. Pletikosić, M. Petrović, P. Pervan, M. Milun, A. T. N'Diaye, C. Busse, T. Michely, J. Fujii, and I. Vobornik, *Graphene on Ir(111) characterized by angle-resolved photoemission*, Phys. Rev. B **84**, 075427 (2011).

[60] C. Davisson and L. H. Germer, *Diffraction of Electrons by a Crystal of Nickel*, Phys. Rev. **30**, 705–740 (1927).

[61] N. W. Ashcroft and D. N. Mermin, *Festkörperphysik* (Oldenbourg, 2007).

[62] A. Zangwill, *Physics at Surfaces* (Cambridge University Press, 1988).

[63] G. Binnig, H. Rohrer, C. Gerber, and E. Weibel, *Surface Studies by Scanning Tunneling Microscopy*, Phys. Rev. Lett. **49**, 57–61 (1982).

[64] J. Bardeen, *Tunnelling from a Many-Particle Point of View*, Phys. Rev. Lett. **6**, 57–59 (1961).

[65] J. Tersoff and D. R. Hamann, *Theory of the scanning tunneling microscope*, Phys. Rev. B **31**, 805–813 (1985).

[66] B. H. Bransden and C. J. Joachin, *Physics of Atoms and Molecules* (Pearson Education, 2003).

[67] B. Schrader, *Raman Spectroscopy* (VCH Verlagsgesellschaft, 1995).

[68] C. V. Raman, *Part II.—The Raman effect. Investigation of molecular structure by light scattering*, Trans. Faraday Soc. **25**, 781–792 (1929).

[69] R. V. Gorbachev, I. Riaz, R. R. Nair, R. Jalil, L. Britnell, B. D. Belle, E. W. Hill, K. S. Novoselov, K. Watanabe, T. Taniguchi, A. K. Geim, and P. Blake, *Hunting for Monolayer Boron Nitride: Optical and Raman Signatures*, Small **7**, 465–468.

[70] J. Wu, W.-Q. Han, W. Walukiewicz, J. W. Ager, W. Shan, E. E. Haller, and A. Zettl, *Raman Spectroscopy and Time-Resolved Photoluminescence of BN and BxCyNz Nanotubes*, Nano Letters **4**, 647–650 (2004).

[71] Q. Cai, D. Scullion, A. Falin, K. Watanabe, T. Taniguchi, Y. Chen, E. J. G. Santos, and L. H. Li, *Raman signature and phonon dispersion of atomically thin boron nitride*, Nanoscale **9**, 3059–3067 (2017).

[72] L. A. Falkovsky, *Phonon dispersion in graphene*, Journal of Experimental and Theoretical Physics **105**, 397–403 (2007).

[73] M. S. Dresselhaus, A. Jorio, A. G. Souza Filho, and R. Saito, *Defect characterization in graphene and carbon nanotubes using Raman spectroscopy*, Philosophical Transactions of the Royal Society of London A: Mathematical, Physical and Engineering Sciences **368**, 5355–5377 (2010).

[74] R. Beams, L. G. Cançado, A. Jorio, A. N. Vamivakas, and L. Novotny, *Tip-enhanced Raman mapping of local strain in graphene*, Nanotechnology **26**, 175702 (2015).

[75] J.-B. Wu, M.-L. Lin, X. Cong, H.-N. Liu, and P.-H. Tan, *Raman spectroscopy of graphene-based materials and its applications in related devices*, Chem. Soc. Rev. **47**, 1822–1873 (2018).

[76] R. Beams, L. G. Cançado, and L. Novotny, *Raman characterization of defects and dopants in graphene*, Journal of Physics: Condensed Matter **27**, 083002 (2015).

[77] L. Malard, M. Pimenta, G. Dresselhaus, and M. Dresselhaus, *Raman spectroscopy in graphene*, Physics Reports **473**, 51 – 87 (2009).

[78] D. M. Hoffman, G. L. Doll, and P. C. Eklund, *Optical properties of pyrolytic boron nitride in the energy range 0.05—10 eV*, Phys. Rev. B **30**, 6051–6056 (1984).

[79] R. J. Koch, J. Katoch, S. Moser, D. Schwarz, R. K. Kawakami, A. Bostwick, E. Rotenberg, C. Jozwiak, and S. Ulstrup, *Electronic structure of exfoliated and epitaxial hexagonal boron nitride*, Phys. Rev. Materials **2**, 074006 (2018).

[80] P. R. Wallace, *The Band Theory of Graphite*, Phys. Rev. **71**, 622–634 (1947).

[81] *The structure of graphite*, Proceedings of the Royal Society of London A: Mathematical, Physical and Engineering Sciences **106**, 749–773 (1924).

[82] H. Lipson and R. Stokes, *The structure of graphite*, Proceedings of the Royal Society of London A: Mathematical, Physical and Engineering Sciences **181**, 101–105 (1942).

[83] M. Schmitz, S. Engels, L. Banszerus, K. Watanabe, T. Taniguchi, C. Stampfer, and B. Beschoten, *High mobility dry-transferred CVD bilayer graphene*, Applied Physics Letters **110**, 263110 (2017).

[84] V. I. Artyukhov, Y. Hao, R. S. Ruoff, and B. I. Yakobson, *Breaking of Symmetry in Graphene Growth on Metal Substrates*, Phys. Rev. Lett. **114**, 115502 (2015).

[85] J. Wintterlin and M.-L. Bocquet, *Graphene on metal surfaces*, Surface Science **603**, 1841 – 1852 (2009), special Issue of Surface Science dedicated to Prof. Dr. Dr. h.c. mult. Gerhard Ertl, Nobel-Laureate in Chemistry 2007.

[86] A. Nagashima, N. Tejima, and C. Oshima, *Electronic states of the pristine and alkali-metal-intercalated monolayer graphite/Ni(111) systems*, Phys. Rev. B **50**, 17487–17495 (1994).

[87] I. Miccoli, F. Edler, H. Pfnür, and C. Tegenkamp, *The 100th anniversary of the four-point probe technique: the role of probe geometries in isotropic and anisotropic systems*, Journal of Physics: Condensed Matter **27**, 223201 (2015).

[88] L. J. van der Pauw, *A method of measuring the resistivity and hall coefficent on lamellae of arbitrary shape*, Philips technical review **20**, 220–224 (1958).

[89] L. J. van der Pauw, *A method of measuring specific resistivity and hall effect of discs of arbitrary shape*, Philips Res. Repts **13**, 1–9 (1958).

[90] G. D. Mahan, *Conformal Mapping*, in *Applied Mathematics* (Springer US, Boston, MA, 2002) pp. 141–176.

[91] Q.-T. Truong, P. Pokharel, G. S. Song, and D.-S. Lee, *Preparation and Characterization of Graphene Nanoplatelets from Natural Graphite via Intercalation and Exfoliation with Tetraalkylammoniumbromide*, Journal of Nanoscience and Nanotechnology **12**, 4305–4308 (2012).

[92] E. Bjerglund, M. Kongsfelt, K. Shimizu, B. B. E. Jensen, L. Koefoed, M. Ceccato, T. Skrydstrup, S. U. Pedersen, and K. Daasbjerg, *Controlled Electrochemical Carboxylation of Graphene To Create a Versatile Chemical Platform for Further Functionalization*, Langmuir **30**, 6622–6628 (2014).

[93] G. Lupina, J. Kitzmann, I. Costina, M. Lukosius, C. Wenger, A. Wolff, S. Vaziri, M. Östling, I. Pasternak, A. Krajewska, W. Strupinski, S. Kataria, A. Gahoi, M. C. Lemme, G. Ruhl, G. Zoth, O. Luxenhofer, and W. Mehr, *Residual Metallic Contamination of Transferred Chemical Vapor Deposited Graphene*, ACS Nano **9**, 4776–4785 (2015), pMID: 25853630.

[94] E. Miniussi, C. Bernard, H. Y. Cun, B. Probst, D. Leuenberger, G. Mette, W.-D. Zabka, M. Weinl, M. Haluska, M. Schreck, J. Osterwalder, and T. Greber, *Fermi surface map of large-scale single-orientation graphene on SiO 2*, Journal of Physics: Condensed Matter **29**, 475001 (2017).

[95] B. Technology, *Sample Mountig Boards* (2018).

[96] G. Associates, *GMW Diopole Electromagnet* (2018).

[97] Graphenea, *Product Datasheet, Graphenea Monolayer Graphene film on various substrates* (2018).

[98] Z. Salmi, L. Koefoed, B. B. E. Jensen, A. G. Čabo, P. Hofmann, S. U. Pedersen, and K. Daasbjerg, *Electroinduced Intercalation of Tetraalkylammonium Ions at the Interface of Graphene Grown on Copper, Platinum, and Iridium*, ChemElectroChem **3**, 2202–2211.

[99] S. Hofmann, P. Braeuninger-Weimer, and R. S. Weatherup, *CVD-Enabled Graphene Manufacture and Technology*, The Journal of Physical Chemistry Letters **6**, 2714–2721 (2015), pMID: 26240694.

[100] L. Mircosystems, *Leica DVM2500 and DVM5000 HD Specifications* (2012).

[101] M. Muntwiler, J. Zhang, R. Stania, F. Matsui, P. Oberta, U. Flechsig, L. Patthey, C. Quitmann, T. Glatzel, R. Widmer, E. Meyer, T. A. Jung, P. Aebi, R. Fasel,

and T. Greber, *Surface science at the PEARL beamline of the Swiss Light Source*, Journal of Synchrotron Radiation **24**, 354–366 (2017).

[102] P. Blake, E. W. Hill, A. H. Castro Neto, K. S. Novoselov, D. Jiang, R. Yang, T. J. Booth, and A. K. Geim, *Making graphene visible*, Applied Physics Letters **91**, 063124 (2007).

[103] I. Jung, M. Pelton, R. Piner, D. A. Dikin, S. Stankovich, S. Watcharotone, M. Hausner, and R. S. Ruoff, *Simple Approach for High-Contrast Optical Imaging and Characterization of Graphene-Based Sheets*, Nano Letters **7**, 3569–3575 (2007).

[104] A. C. Ferrari, J. C. Meyer, V. Scardaci, C. Casiraghi, M. Lazzeri, F. Mauri, S. Piscanec, D. Jiang, K. S. Novoselov, S. Roth, and A. K. Geim, *Raman Spectrum of Graphene and Graphene Layers*, Phys. Rev. Lett. **97**, 187401 (2006).

[105] F. Tuinstra and J. L. Koenig, *Raman Spectrum of Graphite*, The Journal of Chemical Physics **53**, 1126–1130 (1970).

[106] L. G. Cançado, A. Jorio, E. H. M. Ferreira, F. Stavale, C. A. Achete, R. B. Capaz, M. V. O. Moutinho, A. Lombardo, T. S. Kulmala, and A. C. Ferrari, *Quantifying Defects in Graphene via Raman Spectroscopy at Different Excitation Energies*, Nano Letters **11**, 3190–3196 (2011), pMID: 21696186.

[107] A. C. Ferrari, *Raman spectroscopy of graphene and graphite: Disorder, electron–phonon coupling, doping and nonadiabatic effects*, Solid State Communications **143**, 47 – 57 (2007), exploring graphene.

[108] K. N. Kudin, B. Ozbas, H. C. Schniepp, R. K. Prud'homme, I. A. Aksay, and R. Car, *Raman Spectra of Graphite Oxide and Functionalized Graphene Sheets*, Nano Letters **8**, 36–41 (2008).

[109] T. Shimada, T. Sugai, C. Fantini, M. Souza, L. Cançado, A. Jorio, M. Pimenta, R. Saito, A. Grüneis, G. Dresselhaus, M. Dresselhaus, Y. Ohno, T. Mizutani, and H. Shinohara, *Origin of the 2450cm-1 Raman bands in HOPG, single-wall and double-wall carbon nanotubes*, Carbon **43**, 1049 – 1054 (2005).

[110] J. Wu, W.-Q. Han, W. Walukiewicz, J. W. Ager, W. Shan, E. E. Haller, and A. Zettl, *Raman Spectroscopy and Time-Resolved Photoluminescence of BN and BxCyNz Nanotubes*, Nano Letters **4**, 647–650 (2004).

[111] D. Nečas and P. Klapetek, *Gwyddion: an open-source software for SPM data analysis*, Central European Journal of Physics **10**, 181–188 (2012).

[112] S. Berner, M. Corso, R. Widmer, O. Groening, R. Laskowski, P. Blaha, K. Schwarz, A. Goriachko, H. Over, S. Gsell, M. Schreck, H. Sachdev, T. Greber, and J. Osterwalder, *Boron Nitride Nanomesh: Functionality from a Corrugated Monolayer*, Angewandte Chemie International Edition **46**, 5115–5119.

[113] M. Corso, W. Auwärter, M. Muntwiler, A. Tamai, T. Greber, and J. Osterwalder, *Boron Nitride Nanomesh*, Science (2004), 10.1126/science.1091979.

[114] T. Brugger, S. Günther, B. Wang, J. H. Dil, M.-L. Bocquet, J. Osterwalder, J. Wintterlin, and T. Greber, *Comparison of electronic structure and template function of single-layer graphene and a hexagonal boron nitride nanomesh on Ru(0001)*, Phys. Rev. B **79**, 045407 (2009).

[115] J. W. Arblaster, *Crystallographic Properties of Rhodium*, Platinum Metals Rev. **41**, 184–189 (1997).

[116] B. Wang, M.-L. Bocquet, S. Marchini, S. Günther, and J. Wintterlin, *Chemical origin of a graphene moiré overlayer on Ru(0001)*, Phys. Chem. Chem. Phys. **10**, 3530–3534 (2008).

[117] R. Laskowski and P. Blaha, *Unraveling the structure of the h-BN/Rh(111) nanomesh with ab initio calculations*, Journal of Physics: Condensed Matter **20**, 064207 (2008).

[118] W. Auwärter, T. Kreutz, T. Greber, and J. Osterwalder, *XPD and STM investigation of hexagonal boron nitride on Ni(111)*, Surface Science **429**, 229 – 236 (1999).

[119] H.-f. Ma, M. Thomann, J. Schmidlin, S. Roth, M. Morscher, and T. Greber, *Corrugated single layer templates for molecules : From h -BN nanomesh to graphene based quantum dot arrays*, **5**, 387–392 (2010).

[120] S. Doniach and M. Sunjic, *Many-electron singularity in X-ray photoemission and X-ray line spectra from metals*, Journal of Physics C: Solid State Physics **3**, 285 (1970).

[121] S. T. Jackson and R. G. Nuzzo, *Determining hybridization differences for amorphous carbon from the XPS C 1s envelope*, Applied Surface Science **90**, 195 – 203 (1995).

[122] J. Díaz, G. Paolicelli, S. Ferrer, and F. Comin, *Separation of the sp^3 and sp^2 components in the C1s photoemission spectra of amorphous carbon films*, Phys. Rev. B **54**, 8064–8069 (1996).

[123] T. Susi, M. Kaukonen, P. Havu, M. P. Ljungberg, P. Ayala, and E. I. Kauppinen, *Core level binding energies of functionalized and defective graphene*, Beilstein J Nanotechnol **5**, 121–132 (2014), 24605278[pmid].

[124] A. B. Preobrajenski, A. S. Vinogradov, M. L. Ng, E. Ćavar, R. Westerström, A. Mikkelsen, E. Lundgren, and N. Mårtensson, *Influence of chemical interac-*

tion at the lattice-mismatched h-BN/Rh(111) and h-BN/Pt(111) interfaces on the overlayer morphology, Phys. Rev. B **75**, 245412 (2007).

[125] R. Stania, W. Heckel, I. Kalichava, C. Bernard, T. C. Kerscher, H. Y. Cun, P. R. Willmott, B. Schönfeld, J. Osterwalder, S. Müller, and T. Greber, *Self-assembly of nanoscale lateral segregation profiles*, Phys. Rev. B **93**, 161402 (2016).

[126] M. E. Greif, *Time-Resolved Photoelectron Diffraction*, Ph.D. thesis, University of Zurich (2015).

[127] T. Brugger, H. Ma, M. Iannuzzi, S. Berner, A. Winkler, J. Hutter, J. Osterwalder, and T. Greber, *Nanotexture Switching of Single-Layer Hexagonal Boron Nitride on Rhodium by Intercalation of Hydrogen Atoms*, Angewandte Chemie International Edition **49**, 6120–6124.

[128] S. M. Poh, X. Zhao, S. J. R. Tan, D. Fu, W. Fei, L. Chu, D. Jiadong, W. Zhou, S. J. Pennycook, A. H. Castro Neto, and K. P. Loh, *Molecular Beam Epitaxy of Highly Crystalline MoSe2 on Hexagonal Boron Nitride*, ACS Nano **12**, 7562–7570 (2018), pMID: 29985581.

[129] Y. Ding, Y. Wang, J. Ni, L. Shi, S. Shi, and W. Tang, *First principles study of structural, vibrational and electronic properties of graphene-like MX2 (M=Mo, Nb, W, Ta; X=S, Se, Te) monolayers*, Physica B: Condensed Matter **406**, 2254–2260 (2011).

[130] H. P. Komsa and A. V. Krasheninnikov, *Electronic structures and optical properties of realistic transition metal dichalcogenide heterostructures from first principles*, Physical Review B - Condensed Matter and Materials Physics **88**, 1–7 (2013).

[131] H. Henck, D. Pierucci, G. Fugallo, J. Avila, G. Cassabois, Y. J. Dappe, M. G. Silly, C. Chen, B. Gil, M. Gatti, F. Sottile, F. Sirotti, M. C. Asensio, and A. Ouerghi,

Direct observation of the band structure in bulk hexagonal boron nitride, Physical Review B **95**, 085410 (2017).

[132] J. Gómez Díaz, Y. Ding, R. Koitz, A. P. Seitsonen, M. Iannuzzi, and J. Hutter, *Hexagonal boron nitride on transition metal surfaces*, Theoretical Chemistry Accounts **132**, 1–17 (2013).

[133] Z. Lin, A. McCreary, N. Briggs, S. Subramanian, K. Zhang, Y. Sun, X. Li, N. J. Borys, H. Yuan, S. K. Fullerton-Shirey, A. Chernikov, H. Zhao, S. McDonnell, A. M. Lindenberg, K. Xiao, B. J. LeRoy, M. Drndić, J. C. M. Hwang, J. Park, M. Chhowalla, R. E. Schaak, A. Javey, M. C. Hersam, J. Robinson, and M. Terrones, *2D materials advances: from large scale synthesis and controlled heterostructures to improved characterization techniques, defects and applications*, 2D Materials **3**, 042001 (2016).

[134] X. Wang, Y. Gong, G. Shi, W. L. Chow, K. Keyshar, G. Ye, R. Vajtai, J. Lou, Z. Liu, E. Ringe, B. K. Tay, and P. M. Ajayan, *Chemical Vapor Deposition Growth of Crystalline Monolayer* $MoSe_2$, ACS Nano **8**, 5125–5131 (2014), pMID: 24680389.

[135] S. Wang, X. Wang, and J. H. Warner, *All Chemical Vapor Deposition Growth of* MoS_2*/h-BN Vertical van der Waals Heterostructures*, ACS Nano **9**, 5246–5254 (2015).

[136] S. J. H., *Hartree-Slater subshell photoionisation cross-sections at 1254 and 1487 eV*, Journal of Electron Spectroscopy and Related Phenomena , 129–137 (1976).

[137] S. Ivan N. and K. Lubomir, *Zur Theorie der orentierten Ausscheidung von Ionenkristallen aufeinander*, Abhandlung der Mathematisch Naturwissenschaftlichen Klasse IIb Akademie der Wissenschaften Wien **146**, 797–810 (1938).

[138] J. R. Schaibley, H. Yu, G. Clark, P. Rivera, J. S. Ross, K. L. Seyler, W. Yao, and X. Xu, *Valleytronics in 2D materials*, Nature Reviews Materials **1**, 16055 EP – (2016), review Article.

[139] F. Langer, C. P. Schmid, S. Schlauderer, M. Gmitra, J. Fabian, P. Nagler, C. Schüller, T. Korn, P. G. Hawkins, J. T. Steiner, U. Huttner, S. W. Koch, M. Kira, and R. Huber, *Lightwave valleytronics in a monolayer of tungsten diselenide*, Nature **557**, 76–80 (2018).

[140] B. Salzmann, C. Bernard, A. Hemmi, and T. Greber, *Remote doping of graphene on SiO2 with 5 keV x-rays in air*, Journal of Vacuum Science & Technology A **36**, 020603 (2018).

[141] Y. Sugiyama, C. Bernard, Y. Okuyama, S. ichiro Ideta, K. Tanaka, T. Greber, and T. Hirahara, *Flattening and manipulation of the electronic structure of h-BN/Rh(111) nanomesh upon Sn intercalation*, Surface Science **672-673**, 33 – 38 (2018).

[142] G. E. Moore, *Cramming more components onto integrated circuits, Reprinted from Electronics, volume 38, number 8, April 19, 1965, pp.114 ff.*, IEEE Solid-State Circuits Society Newsletter **11**, 33–35 (2006).

[143] H. Cun, A. Hemmi, E. Miniussi, C. Bernard, B. Probst, K. Liu, D. T. L. Alexander, A. Kleibert, G. Mette, M. Weinl, M. Schreck, J. Osterwalder, A. Radenovic, and T. Greber, *Centimeter-Sized Single-Orientation Monolayer Hexagonal Boron Nitride With or Without Nanovoids*, Nano Letters **18**, 1205–1212 (2018), pMID: 29314849.

List of Publications

1. **Self-assembly of nanoscale lateral segregation profiles**

   Stania, R. and Heckel, W. and Kalichava, I. and Bernard, C. and Kerscher, T. C. and Cun, H. Y. and Willmott, P. R. and Schönfeld, B. and Osterwalder, J. and Müller, S. and Greber, T.

   American Physical Society, Physical Review B (2016), [125]

2. **High quality single atomic layer deposition of hexagonal boron nitride on single crystalline Rh(111) four-inch wafers**

   Hemmi Adrian and Bernard Carlo and Cun Huanyao and Roth Silvan and Kloeckner Martin and Kaelin Thomas and Weinl Michael Gsell Stefan and Schreck Matthias and Osterwalder Jürg and Greber Thomas

   Review of Scientific Instruments (2014), [30]

3. **Fermi surface map of large-scale single-orientation graphene on SiO 2**

   E Miniussi and C Bernard and H Y Cun and B Probst and D Leuenberger and G Mette and W-D Zabka and M Weinl and M Haluska and M Schreck and J Osterwalder and T Greber

   Journal of Physics: Condensed Matter (2017), [94]

4. **Flattening and manipulation of the electronic structure of h-BN/Rh(111) nanomesh upon Sn intercalation**

   Yuya Sugiyama and Carlo Bernard and Yuma Okuyama and Shin-ichiro Ideta and Kiyohisa Tanaka and Thomas Greber and Toru Hirahara

   Surface Science (2018), [141]

5. **Remote doping of graphene on SiO2 with 5 keV x-rays in air**

   Salzmann,Björn and Bernard,Carlo and Hemmi,Adrian and Greber,Thomas

   Journal of Vacuum Science & Technology A (2018), [143]

6. **Centimeter-Sized Single-Orientation Monolayer Hexagonal Boron Nitride With or Without Nanovoids**

   Cun, Huanyao and Hemmi, Adrian and Miniussi, Elisa and Bernard, Carlo and Probst, Benjamin and Liu, Ke and Alexander, Duncan T. L. and Kleibert, Armin and Mette, Gerson and Weinl, Michael and Schreck, Matthias and Osterwalder, Jürg and Radenovic, Aleksandra and Greber, Thomas

   ACS Nano Letters (2018), [143]

7. **Electronic Properties of Transferable Atomically Thin MoSe2/h-BN Heterostructures Grown on Rh(111)**

   Chen, Ming-Wei and Kim, HoKwon and Bernard, Carlo and Pizzochero, Michele and Zaldıivar, Javier and Pascual, Jose Ignacio and Ugeda, Miguel M. and Yazyev, Oleg V. and Greber, Thomas and Osterwalder, Jürg and Renault, Olivier and Kis, Andras

   ACS Nano Letters (2018), [34]

Curriculum Vitae

Name:	Carlo Maria Bernard
Birth:	22.02.1985 in Rome, Italy
Nationality:	Swiss, Italian

Education

2012 - 2018	PhD in experimental Physics University of Zurich Zurich, Switzerland Group of Prof. Dr. Jürg Osterwalder and Prof. Dr. Thomas Greber
2017 - 2018	High Education Diploma (Ongoing) Pädagogische Hochschule Thurgau Kreuzlingen, Switzerland
2010 - 2012	Master Diploma in Physics University of Zurich Zurich, Switzerland Group of Prof. Dr. Jürg Osterwalder and Prof. Dr. Thomas Greber Luminescence Mapping of Ordered Silver Nanoclusters on Hexagonal Boron Nitride Nanomesh
2004 - 2010	Bachelor Diploma in Physics University of Roma Tre Rome, Italy

---

Teaching Experience

2017 - 2018	Physics and Mathematics Teacher Kantonsschule Heerbrugg, Switzerland
2012 - 2016	Semester Assistant in Physics
2013 - 2014	Lecture Assistant in Physics 1 and Physics 2

Acknowledgments

In the following I express my gratitude to every person who contributed to the completion of this PHD. I would like to especially thank the members of my PHD-committee Prof. Dr. Thomas Greber, Prof. Dr. Jürg Osterwalder and Prof. Dr. Peter Sutter for the help, suggestions, support, their time and in particular for the opportunity to learn from their vast experience in the surface science field.

I would like to thank my colleagues in the sinergia, ESCA, SQUID and laser laboratory, for the great time in the lab and the fruitful discussions along the years, especially in front of the coffee machine. A special thank goes to Dr. Roland Stania, with whom I had the pleasure to share various beam times and night shifts at PEARL and ESCA laboratory, since the days of the master thesis, Dr. Matthias Muntwiler for the support at the PEARL endstation, Dr. Aram Kostanian, Dr. Wolf-Dietrich Zabka, Dr. Adrian Schuler for the companionship during the years.

My gratitude also goes to our laboratory technical responsible Thomas Kälin, to the machine work shop and the electronic work shop of the University of Zurich for their technical suggestions, support and out of the ordinary readiness every time an unexpected issue appeared.

Finally I thank my family, relatives and friends for the appreciated support in these years.